STRESS REDUCTION IN A PLATE WITH A HOLE BY APPLIED INDUCED STRAINS

by

Pradeep Kumar Sensharma

Dissertation submitted to the Faculty of the
Virginia Polytechnic Institute and State University
in partial fulfillment of the requirements for the degree of

Doctor of Philosophy

in

Aerospace and Ocean Engineering

APPROVED:

R. T. Haftka, Chairman

C. A. Rogers

O. F. Hughes

O. H. Griffin

E. R. Johnson

R. K. Kapania

E. Nikolaidis

December, 1993

Blacksburg, Virginia

STRESS REDUCTION IN A PLATE WITH A HOLE BY APPLIED INDUCED STRAINS

by

Pradeep Kumar Sensharma

Committee Chairman: Dr R.T. Haftka

Aerospace and Ocean Engineering

(ABSTRACT)

This work investigates the potential of reducing stresses in the region of stress concentration by applied induced strains. A thin 30 inch square plate with a 1 inch diameter circular hole under uniaxial load was used for this investigation.

This investigation considered first an ideal case with a few physical limitations for the purpose of probing the limits of active stress reduction. Applied induced strains were applied over the region $A \leq r \leq 1.5A$, where A is the radius of the hole. It was found that the axisymmetric applied induced strains could reduce the stress concentration factor (SCF) from 3 to 2. With non-axisymmetric applied induced strain distribution the SCF could be reduced to 1.45. Numerical optimizations based on finite element simulations were also carried out for a composite plate with a hole and similar reductions in stress concentration factors were obtained.

Next, a more realistic case, consisting of bonded and embedded piezoelectric actuators was considered. It was found that partial-thickness actuators produce large radial stresses which erase any benefits associated with axisymmetric actuation.

With non-axisymmetric actuation, the actuators with present technology limitations were found to be effective in reducing stress concentration factor for a fatigue load case. However, due to repetative nature of the load, the energy expenditure may be large. For

an extreme load case, actuators with present technology limitations were not very effective in reducing SCF. Actuators were needed to be placed over a larger area to achieve a larger reduction in SCF. Also, passive stiffening was found to be more effective in reducing stress concentration than bonded actuators with present technology limitations.

ACKNOWLEDGEMENTS

I am indebted to Dr. R. T. Haftka for the help and guidance he has given me throughout this work. I am also grateful to Dr. O. F. Hughes, Dr. C. A. Rogers, Dr. O. H. Griffin, Dr. E. R. Johnson, Dr. R. K. Kapania and Dr. E. Nikolaidis for their time and effort during the course of this work.

Special thanks to my wife, Nisha, for the happiness she brought into my life and also for bringing our lovely and adorable son, Anuraag, to this world. I am also very grateful to my brothers, Pranab and Prabir, and sisters, Deepti and Rita, for their encouragement and support.

Thanks are due to my fellow students in Femoyer 109, 203 and 205 for their help and advice and for making Femoyer a fun place to work in. I would also like to thank M. P. Palanterä and Dr. M. H. Kadivar for their contribution to this research. Thanks are also due to Hans, Yuping, Renjith and Jayashree for their moral support throughout this endeavor.

I would like to acknowledge and thank the National Aeronautics and Space Administration and US Army Research Office for supporting this work.

Finally, this work is dedicated to my loving parents, Aparna and Lilamoy, whose constant support and encouragement made my educational achievements possible.

TABLE OF CONTENTS

LIST OF FIGURES

LIST OF TABLES

CHAPTER 1

INTRODUCTION TO SMART STRUCTURES

In the past, material systems and structures were limited to passive response to external stimuli. However, with the advent of intelligent material systems, the structures are becoming active in variety of manners. Intelligent material systems have been identified as one of the most important emerging materials technology areas for space and aerospace and are regarded by some as the first really new idea relating to structural materials since the introduction of structural composites in the 1960's (Davidson, [1]). They are expected to revolutionize what structures and material systems are capable of doing.

Smart structures are a new class of structures which have self-inspection and inherent adaptive capabilities. Nature is the source of most of the ideas within the the area of smart structures. Zuk and Clark wrote in their book Kinetic Architecture [2] , *"Life itself is motion, from the single cell to the most complex organism, man. When motion ceases, life ceases. Motion of the limbs, the lungs, and the heart are taken to be virtually synonymous with life. It is these attributes of motion, of mobility, of change, of adaptation that place living things on higher plateau of evolution than static forms. Indeed, survival of these living species depends on their kinetic abilities: to nourish themselves, to heal themselves, to reproduce themselves, to adapt to changing needs and environments, and in this case of man to be materially and spiritually productive."* Smart structures technology enhances existing structural materials, enabling complex functions to be carried out within the material itself and opening up opportunities for radical change in approaches to structural design. The applications of this technology are wide ranging,

from civil engineering through industries like the oil industry, to more advanced technology areas such as aerospace and defense. Potential advantages of this new technology include improved process yield, increased safety through real time structural monitoring, increased efficiency by minimizing structural repair time, and cost savings and weight reduction by reducing over engineering of structures. The concept of smart structures is based on advanced developments in both material and information sciences.

1.1 DEFINITION OF SMART STRUCTURES

A smart structure (or adaptive structure, or intelligent structure) can be defined as a structure which can sense its state and can take corrective measures, if necessary, to perform its mission at the highest possible performance level. Wada et al. [3] define adaptive structures as structural systems whose geometric and inherent characteristics can be changed beneficially to meet mission requirements either through remote commands and/or automatically in response to external stimulations. Rogers [4] distinguishes adaptive structures from intelligent structures and according to him intelligent structures do not simply perform functions programmed a priori (adaptive structures), but also learn the appropriate responses to a wide range of situations and should also have means to convey information to the designer and user. According to Gandhi et al. [5], ingredients of a smart structure are a host structural material, a network of sensors, a network of actuators, microprocessor-based computational capabilities, and real-time control capabilities. Additionally these structures must demonstrate (i) the ability to respond almost instantaneously to changes in external stimuli, (ii) they must feature an inherent ability to interface with modern microprocessors and solid-state electronics, and (iii) they should possess the inherent ability to integrate modern control systems. Miura [6], defines structure as ".... a device which determines the relative position of

numbers of points in space." Since the relative position depends on the configuration (geometry) and force (dynamics), according to him the intelligence of structures should be defined in connection with their geometric and dynamic properties. With this logic, Miura defines adaptive or intelligent structures as structures equipped with intelligence and active mechanisms, which can change their geometric and dynamic properties.

There is no universally accepted definition of the term smart structures. However, a reasonable working definition of such a structure would probably include the elements shown in Figure 1.1, taken from Spillman [7]. Although five distinct elements are shown, any or all of them could represent different characteristics of a single multifunctional entity. When these elements are fused to form a smart structure, one of the principle characteristics of that structure is that it has a purpose that it strives to achieve. The structure acts to optimize itself and overcome obstacles to fulfill its purpose, i.e., it adapts to changing conditions. A generic diagram illustrating the pattern of activity in a smart structure is shown in Figure 1.2 (also by Spillman [7]). The three main components of smart structures, i.e., sensors, controls and actuators can be compared to biological counterparts. Sensors work as artificial nerves and describe the state of the material or structure. Controls are the intelligence which decide what corrective action should be taken and passes these decisions to the actuators. Actuators are the muscles that contract or expand to take the corrective measures, based on the directives received from the control system.

The inspiration and motivation for this new field is also to create a higher form of material systems and structures by providing the "life" functions of sensing, actuation, control and intelligence to material and structures (Chaudhry, [8]). In addition to the capability of adaptation, natural systems operate in a mode to reduce energy consump-

tion. In the same vein the goal of intelligent material systems proposed by Rogers [9] is to "replace mass and energy with intelligence". Thus by studying the different methods by which nature creates adaptive functions, we can develop synthetic methods to mimic those of nature.

According to Rogers [9], the modes of adaptibility in nature and in smart material systems can be classified as follows:

- Variation in material properties, i.e., stiffness;
- Changes in strain energy of a system;
- Application of forces, moments and torques;
- Shifting of energy from one mode to another.

In a report published by Japan Science and Technology Agency [10] on the concept of intelligent materials, the following currently imaginable intelligent structural materials and expected intelligent functions related to their use were listed

- Materials which restrain the advance of cracks by producing compression stress around them through volume change from stress-induced transformation at the tip of the crack, when the cracks are produced in strong parts due to repeated stress. [Recognition/Discriminaton, Redundancy]
- Materials which recognize the load speed of stress and generate a large force against the shock stress by discriminating whether it is shock or static stress. [Recognition/Discriminaton, Redundancy]
- Materials which give a warning and supress the advance of generated deformations, damage, etc. or repair themselves to their original form in the course of time (automobile

bodies, aircraft, etc.). [Self -Diagnosis, Prediction/notification, Self-Repair]

• Materials which are usable over an extremely wide range of temperatures with a suitable change in composition by transformation on chemical reaction according to the environment (heat-resistant materials for the space shuttle, etc.). [Self-Adaptation/Surrounding-Adjustment]

Two major components of smart structures, the sensors and the actuators are described below.

1.2 SENSOR SYSTEMS

Integrated sensors can be either internal or external (Dittrich, [11]). Internal sensors are used to monitor the structure itself, by measuring temperature, strain or vibration, or by detecting damage due to overloading or impact. External sensors are mainly used for detecting electromagnetic energy. The most common sensor elements are described below.

1.2.1 Fiber Optic Sensors

A fiber optic nervous system (Measures [12], Udd [13]) may be used to support the necessary sensing functions of smart structures and has several compelling advantages with respect to electrical alternatives. In many cases fiber sensors are enabling technology where equivalent electrical devices do not exist. It is possible to embed fiber optic sensors into composite structures during manufacturing to allow internal interrogation of material. They are compatible with common fabrication processes and are capable of withstanding strains of the same magnitude as the composite itself. Fiber optic sensors can be used for continuous monitoring of structures at all stages of its life. Optical

fiber sensors can be designed to detect a whole range of physical parameters including temperature, strain, pressure, electric fields and magnetic fields. Optical fibers possess many attractive features that make them eminently suitable to serve as the sensory systems for a smart structure (Measures [12]). In essence these are:

- light in weight
- very small
- immune to electromagnetic interference
- inert and corrosion resistant
- safe and can not initiate fires
- capable of being very sensitive sensors
- embeddable within composite materials
- nonperturbing in regard to structural properties
- signal processing with integrated optics

Distributed and quasi-distributed measurements have been demonstrated using optical radar techniques by monitoring reflected signals (Davidson [1]). In recent report by Culshaw and Michie [14], it has been shown that properly treated optical fibers can be embedded in a composite panel as thin as 1 mm. without any degradation in the mechanical performance of the composite panel.

1.2.2 Piezoelectric Sensors

Piezoelectricity is the phenomenon in which certain crystalline substances develop

electric fields when subjected to pressure forces, or conversely, exhibit mechanical deformations when subjected to electric fields. The relationship between applied electric field and strain is linear. There are a wide variety of materials which exhibit this phenomenon to some degree, including quartz crystals, semi-crystalline polyvinylidene polymers, polycrytalline piezoceramics, and human bone. Piezoelectricity is due to spontaneous separation of charge within certain crystal structures under right conditions. This phenomenon, referred to as spontaneous polarization, is caused by a displacement of the electron clouds relative to their individual atoms, as well as a displacement of the positive ions relative to the negative ions within their crystal cells. Such a situation produces an electric field. Piezoelectrics have been employed extensively in a variety of tranducers, including strain gages, pressure transducers and accelerometer. Piezoelectrics can be used both as sensors and actuators. Piezoelectrics can be either bonded to or embedded in beams, plates and tubes. Due to the brittle nature of piezoelectric ceramics, the piezoelectric sensors are generally made of one of the family of polymers, polyvinyldene fluoride, also known as PVDF or PVF_2. Because it is polymer, it can be formed into very thin sheets and adhered to almost any surface (Rogers, [15]).

Most applications which require a piezoelectric transducer, for example, underwater hydrophones or pressure sensors, use a ceramic material called Lead Zirconium Titanate or PZT. PZT has many advantages;

- chemically inert

- high sensitivity

- can be used over a wide range of pressures without serious non-linearity.

The biggest drawback of the material is its mechanical fragility, like all ceramics,

(Rogers [15]). This problem has now been overcome to a large extent. Neurgoankar et al. [16] have recently reported the development of highly densified PZT which not only exhibit higher electromechanical coupling but also have much better physical properties.

A new sensor recently introduced at the Center of Intelligent Material Systems and Structures is the PZT paint (Chaudhry [8]). The paint is fabricated by grinding piezoceramics to micron sized particles and mixing them with a typical lacquer or enamel. It is intended to simplify processing and attachment of a sensor to a structure. The paint can be applied with a spray or a brush and cures at room temperature in less than an hour. It may be activated by applying a DC field across its electrodes. When stressed, the paint exhibits the direct piezoelectric effect.

1.3 ACTUATOR SYSTEMS

Actuator systems can be divided into two broad catagories (Chaudhry [8]). In the first catagory are the actuators that are widely applied to the surface or are embedded. In the second category are actuators used in truss like structures where they replace some of the truss elements of the structure (Wada et al. [3]). The actuators in the first category are almost invariably induced strain actuators like piezoelectric actuators, whereas in the second category, the active truss members can be conventional displacement actuators, where the length of the members is controlled, or force actuators where the load in the members is controlled. Deployable space structures will make use of such active trusses not only for deployment but also for making fine resoluton adjustments of the structural surfaces (Natori et al., [17]).

Induced strain actuation can be described as the process by which applying actuation strain in some structural elements induces deformations in the entire structure. Here,

actuation strain is the general term applied to the strain components caused by non-mechanical stimulus, i.e., thermal, electrical or magnetic. Piezoelectric materials, shape memory alloys (SMA), electrostrictive materials, magnetostrictive materials etc., can cause such actuation strains. In all of these materials, since the actuation strains can be easily regulated, they can be used to induce strains in a controlled manner in structures to reduce stresses in the regions of high stress concentrations. Actuation strains can also be used to control the deformations of large structures with distributed sensor-actuator systems. Most commonly used induced strain actuators are discussed in the following sections.

1.3.1 Shape Memory Alloys (SMAs)

Shape memory actuators are a form of thermal actuators. They expand upon cooling and contract when heated. These materials possess a unique mechanical (shape) "memory" (Jia and Rogers [18]). The shape memory effect can be described as follows: an object in the low-temperature martensitic condition, when plastically deformed and the external stresses removed, will regain its original shape when heated. The process or phenomenon is the result of a martensitic transformation during heating. The process of regaining original shape is associated with a reverse transformation of the deformed martensitic phase to the higher austenite phase. Most commonly used SMAs are the Nickel-titanium alloys (Nitinol). Shape memory alloys based on NiTi were first investigated by the Naval Ordinance Factory and hence are referred to as Nitinol. The shape recovery performance of Nitinol is phenomenal. The material can be plastically deformed in its low-temperature martensite phase and then restored to the original configuration or shape by heating it above the characteristic temperature. Plastic strains of typically six to eight percent may be completely recovered by heating the material to

its austenite phase. Restraining the material from regaining its memory shape can yield stresses of 100 ksi. It is these force and displacement capabilities that are exploited for electromechanical actuators (Liang and Rogers, [19]). Nitinol actuators embedded in composite structures can be used to modify the static and dynamic response by actively changing the stiffness of the structure, or by alternately activating agonist and antgonist pairs of actuators embedded in a material off the neutral axis (Rogers and Robertshaw [20]).

Lin and Rogers [21] developed a one-dimensional model to calculate strains for symmetric SMA composites beams. Liang and Rogers [22] presented a model to demonstrate the recovery stress and recovery strain relationship and behaviour that is unique to SMAs. Chaudhry and Rogers [23] studied enhanced bending control of beams with SMA wires. Jia and Rogers [24] formulated a generalized laminate shell theory that incorporates embedded SMA fibers.

1.3.2 Piezoelectric Actuators

As mentioned earlier, piezoelectric materials exhibit mechanical deformations when subjected to electrical fields and due to this property these are used as induced strain actuators. Piezoelectrics are available in ceramic or polymer form. Piezoceramics (PZT) are simple, compact, light weight structures which can be incorporated easily into structures. Piezoceramics can be either bonded to or embedded in structures to act as actuators. Piezoelectric actuators are popular due to their large band-width (greater than 20 khz) and their ability to produce extensional as well as compressive strain.

Fanson and Chen [25] and Baz and Poh [26] have done significant work with piezoelectric actuators. Their works on control of motion in beams have demonstrated the

potential of piezoelectric material as distributed actuators. Crawley and de Luis [27] studied stress-strain-voltage behaviour of piezoelectric actuators bonded to and embedded in one dimensional beams. They analyzed the stresses, strains and loads generated on a cantilevered beam when piezoelectric segments were bonded symmetrically on both sides. Their work demonstrated a number of important results such as increased effectiveness of the actuators for stiffer and thinner bonding layers, as well as for stiffer piezoelectric material. Another important observation was that the effective moment resulting from the piezoelectric actuators can be seen as concentrated on the two ends of the actuator when the bonding layer is assumed infinitely thin. Crawley et al. [28] presented a theoretical background for the use of piezoelectrics as elements of intelligent structures. They developed static analysis of piezoelectrics bonded to various substructures. They found that the ability of the piezoelectric actuator to deform an elastic substructure depends on both the piezoelectric constants and the elastic constants of the actuator-substructure system. They also derived a complete laminated plate model and found that their solutions were similar to the simpler models which neglect the full piezoelectric stiffness.

1.3.3 Electrorheological Materials

Electrorheological (ER) materials exhibit changes in rheological behavior in the presence of an electric field. The response of an ER material to an applied electric field can be observed in a variety of material properties. Changes in optical, electrical, volumetric, and mechanical properties of ER materials have all been observed to date, and applications based on each of these changes have been proposed (Coulter et al. [29]). The rheological behavior of ER material can be categorized into pre-yield and post-yield regimes, as shown in Figure 1.3. ER material controllable devices are for the most

part based on controllable post-yield shear behavior of ER suspensions. ER material adaptive structures are made controllable through the incorporation of ER materials at selected locations. For common structural deformation ranges it is likely that contained ER materials will remain in a pre-yield state. The viscosity of ER fluid increases in the presence of electric field. With no field present, the fluid flows freely as water or hydraulic oil. If the electrified ER fluid is sheared with sufficient force, it flows. But when the applied shear force is below the critical value, ER fluid reacts as a solid with measurable stiffness. Investigations of ER controllable devices such as valves, mounts, clutches, brakes, and dampers have by far dominated the ER materials applications research and development spectrum to date (Coulter et al. [29]). ER fluids have certain drawbacks which limit their extensive use at the present time. These are: insufficient stability of properties, a relatively narrow temperature range of activity, and a rather low mechanical response (Korobko [30]).

1.3.4 Electrostrictive Actuators

Electrostrictive materials exhibit an electrostrictive effect, whereby any electric field, positive or negative, induces an electric polarization and makes the material expand. Electrostriction is a second order effect, and hence is quadratic. Electrostrictive actuators are made of ferromagnetic material. Most commonly used electrostrictive material is lead-magnesium-nobiate, or PMN. They require high voltage and stroke is limited to 1000 $\mu\epsilon$ (micro strain). However, electrostrictive actuators exhibit less hysteresis compared to piezoelectrics. They also exhibit no aging or creep since no poling is necessary for electrostriction strains (Uchino [31]).

1.4 APPLICATION OF SMART STRUCTURES

The function of materials for aircraft and space structures is still very limited. Progress has been made by application of materials with improved strength, stiffness and light weight. The next step in technological progress is now expected with smart material systems and structures. Crowson [32] has identified certain potential applications of smart structures for the Department of Defense (DoD) community, and they are listed in Table 1.1. These include airplane wings that could reconfigure themselves to accommodate for flying conditions, submarines which could be virtually invisible to sonar detection, and helicoopter rotors that could redistribute stresses and maximize lift.

At present, most of the work in the area of smart structures is at a research stage with the aim of demonstrating the feasibility for use in real life structures. From the point of view of current research, the application areas can be divide into four broad categories (Chaudhry [8]) :

- Vibration and Acoustic Control
- Motion and Shape Control
- Non-Destructive Evaluation
- Damage Control

Table 1.1. Smart Materials and Structure Applications in DoD Systems(Crowson [32])

Application	Systems	Payoffs	Mission Benefit
Adaptive Control Surfaces	Aircraft (Wings & Control Surfaces)	2x Increase in Lift-to-Drag (L/D) Ratio	30 % Greater Payload 50 % Longer Range 30 % Increase in Maneuverability
Active Acoustic Coatings for Signature Suppression (Broad Band)	Submarines (Coatings)	60 dB noise Suppression 100 x reduction in Settling Time	Active Stealth 2 x Listening Range
Vibration Suppression & Twist Control	Helicopters (Blades)	Active Blade Trimming & Balancing 3 % Gross Wt. Reduction	15 % Increased Readiness Increased Speed-160-200 Knots Increased Agility
Active Structural Tuning & Damping	Precision Space Structures	1 μ m Adjustments over 25 m	Pointing Accuracy

1.4.1 Vibration and Acoustic Control

Most of the work in the area of smart structures have been reported in the area of vibration and acoustic control. Hanagud et al.[33] used bonded piezoelectric actuators and sensors for the vibration control of flexible structures. In this work, the effect of the location and placement of the sensors and actuators and the question of centralized and decentralized actuators and sensors were discussed with reference to selected flexible structures. Dimitriadis et al. [34] analytically studied the behaviour of two dimensional patches of bonded piezolelectric actuators used as vibration actuators. They found that it is possible to excite modes in two dimensional structures using patch type actuators and the location of the actuators strongly influence the ability of the actuator to excite certain modes. Bailey and Hubbard [35] used piezoelectric polymer (Poly Vinylidene Fluoride or PVF2) for active vibration control of cantilever beams. They developed and implemented three different control algorithms on a beam piezoelectric system to control transient cantilever beam vibrations. Gandhi et al. [5] proposed a new generation of smart materials and structures incorporating *embedded hybrid multiple actuation systems* which capitalize on the diverse strengths of both electro-rheological (ER) fluids and piezoelectric materials, and operate in conjunction with fiber optic, and/or conventional sensing systems for the active continuum vibration control of structural and mechanical systems. Nitzsche and Breitbach [36] used embedded PZT crystals in the blade structure to study the performance of a single input, single output, individual control system, designed to attenuate the helicopter rotor vibration. Clark and Fuller [37] experimentally studied the active control of sound radiation from a vibrating simply supported rectangular plate excited by a steady state harmonic point force disturbance. Shape memory alloy hybrid composites have also been used for vibration and acoustic control (Rogers [38]; Anders et al. [39]). Experimental work with nitinol hybrid com-

posite beams with 5%, 10 %, and 15 % nitinol volume fraction and clamped-clamped boundary conditions showed increases in the natural frequency by factors of 1.7, 2.5, and 3.0, respectively.

1.4.2 Motion and Shape Control

Fanson and Garba [40] used active members to replace certain passive members of truss-type structures. The active-member functions dually as a structure element or load carrying member as well as an actuator/sensor pair. The sensors allow measurement of the elastic strain and deformation experienced by the structure due to disturbances such as gravity gradients, thermal distortions, and vibration from on-board activity and maneuvering. The sensor measurments are then processed to generate commands to the actuators which exert internal forces on the structure. The choice of logic employed in converting sensor signals to actuator forces determines the adaptive structures's response characteristics. Natori et al. [41] designed a deployable antenna type structure, where the actuators to deploy the structure can be modified to make the fine resolution adjustments of the structure surface. The actuators used to adjust the member lengths can also be utilized to make adjustments during the mission as well as to provide structural damping. Takahara et al. [42] developed piezo linear actuators (PLAs) which are driven by piezoelectric devices and can be used for adaptive truss structures for precision positioning and shape control. Miura [43] proposed the use of intelligent material concepts for shape control of precision antenna reflectors, and study on construction of large space structures by assembling adaptive structures.

Crawley and Lazarus [44] used piezoelectric actuators for shape control of composite and metal plates. They developed a consistent plate model for isotropic and anisotropic plates, which combines both actuators and substrates into one integrated structure and

considers actuators to be plies of a laminated plate. Their exact solutions showed that the resulting induced strains and curvatures produced through strain actuation are dependent on actuaton strains, geometry of the system, and relative stiffness ratio of the actuators and structures. The results were also verified experimentally. Austin et al. [45] developed an actuator system to deform a wing over its entire cross section so that optimum aerodynamic shapes can be realized for more than one flight condition. Their preliminary aerodynamic analysis indicate that this concept could reduce the drag coefficients of the JSTARS (a Grumman-modified Boeing 707 aircraft) wing by at least 6 % during loiter. Spangler and Hall [46] studied the feasibility of using piezoelectric actuators for actively changing the flap angle of a helicopter rotor blade. In actual wind tunnel tests of a scale model of a helicopter blade, the actual deflections achieved and effectiveness in terms effective angle of attack were significant. Lazarus et al.[47] showed the benefits of using adaptive airfoils for aeroelastic control considering a box type wing structure. They showed that greater authority along with a lower weight penalty is achievable using adaptive aeroelastic structures for a variety of wing designs. Song et al.[48] have also shown the benefits of adaptive airfoils considering an adaptive swept-forward wing, modeled as a thin walled beam. Chaudhry and Rogers [49] presented a new concept of shape control, whereby induced strain actuators are attached to a structure at discrete points (as opposed to being bonded). This proposed configuration was found to enhance the response above the bonded actuator configuration.

1.4.3 Non-Destructive Evaluation

In aeronautical and space applications, the ability to detect and respond to the initiation of structural failures is a critical safety factor. In these applications, a basic intelligent material could be a surface film on the wing of an aircraft which incorporates

a network of sensors and surface acoustic wave generators which can act as a " nervous system"relaying information of wing stress and signals from early crack information to a central information processor reporting wing status to the pilot (Spillman [7]). A later development of the smart material concept could be surface layers on the structural members of an aircraft wing which not only informs a central information processor of a developing crack growth but responds by initiating effort to restrict or slow the crack growth or to effect self-repair.

In the area of non-destructive testing, fiber optic sensors are being actively researched for health monitoring of structures. Integrated fiber optical fibers can reliably detect cracks and, under certain conditions, delaminations in composite structures, thereby making a quick pre/post-flight or continuous damage check possible. Optical fibers have been intensively investigated by Dornier for aircraft applications with promising results (Dittrich [11]). Gerardi [50] suggested use of smart material system for health monitoring of aircraft where sensors, artificial intelligence and advanced analytical techniques will provide real time and continual health assessment. Hickman et al. [51] have succesfully tested a prototype Health Monitoring System (HMS) that can detect structural damages by monitoring vibration signature of a structure. The HMS system uses eddy-current actuators as well as environmental input disturbances to provide structural excitation. By monitoring the vibration signature of the structure with piezoelectric sensors, HMS determines structural abnormalities using pattern recognition techniques to classify the sensor signals and determine the type of defect. Matsuzaki et al.[52] describe the computer simulation analyses on application of a fuzzy logic and a neural network control to tracking and rendezvous of a moving target for docking by an adaptive space structure in order to examine the effectiveness and feasibility of both the controls. Their example simulations have shown that the application of fuzzy control and neural networks is very

effective in the tracking and rendezvous problem. Shaikh et al. [53] developed a novel active sensor by sputtering a piezoelectric film onto a metal fiber. This sensor can detect vibration and fracture in a manner similar to acoustic emmision.

1.4.4 Damage Control

The active damage control concept has been recently introduced by Rogers et al. [54] . They presented a new technique of using induced strain actuators, including Shape Memory Alloys, piezoelectric, electrostrictive, and magnetostrictrictive actuators, to control the propagation of cracks within hybrid composite systems and fatigue damage of metallic and composite material structures. When a crack propagates and is near these embedded induced strain actuators, activation of the embedded induced strain actuators will change the stress and strain distributions at the crack tip resulting in a reduction of the stress intensity factors. Experimentally, they have observed 24 % reduction in the stress intensity factor with embedded shape memory alloy fibers. Rogers et al. [54] have also investigated the use of PZT actuators for controlling fatigue of bonded joints. In an experiment, where a graphite/epoxy beam was bonded to a steel beam, active control using PZT actuators increased the fatigue life of the joint by an order of magnitude.

1.5 MECHANISM OF INDUCED STRAIN ACTUATORS

Induced strain actuators can be defined as : any actuator that develops strains in response to a stimulus. The strains that the actuator develops may be due to material phase change, electromechanical coupling, thermomechanical coupling, or magnetomechanical coupling. In the absence of all mechanical constraints, the strain which develops in an actuator is termed as free induced strain or actuation strain ϵ^i. The total strain

in the actuator can thus be written as:

$$\epsilon^t = \epsilon^m + \epsilon^i \tag{1.1}$$

where ϵ^m is the mechanical strain. Free induced strain is the mechanism by which induced strain actuators exert control on the structure to which they are attached. With the above expression, it is possible to model actuator-structure interaction irrespective of the details of how ϵ^i relates to a certain stimulus.

Two elementary components of an active structure are the induced strain actuator and the structure to which it is attached. Generally, the actuators are bonded or embedded symmetrically about the plate or beam structure as shown in Figure 1.4. When the actuators are activated in phase, they exert a compressive or tensile force on the substrate structure. When the actuators are activated out-of-phase, where one actuator contracts and the other expands, a force couple is produced and flexure is induced in the structure. In a case where the actuator is bonded on one side of the structure only, the structure becomes unsymmetric and the bending and extensional responses are coupled.

1.6 ACTIVE STRESS ALLEVIATION

Induced strain actuators, as mentioned earlier, can be used to induce strains in a structure and reduce stresses in regions of high stress concentration. This application is particularly attractive for structures designed to withstand high stresses for relatively short time durations. Aircraft wing structures, for example, are often designed to withstand high gust and maneuver loads which occur rarely and for short durations only. Active strain reduction could in such cases result in significant weight savings.

So far, very little work has been done in the field of active stress alleviation. Rogers et al. [54] have demonstrated, both numerically and experimentally that substantial

reduction in stress concentration near a crack tip can be achieved using SMA wires. They were able to reduce the peak stresses at the crack tip from 110 MPa to 69 MPa. Holnicki [55] studied the application of induced strains in the form of thermal distortions to a rotating disk loaded by centrifugal load and found an induced strain distribution that reduced the maximum tangential streses in the disk by 80 %.

The objective of the present work was to investigate the effectiveness of active stress alleviation. We studied the effects of both ideal and realistic actuators. Influence of present technology limitations of piezoelectric actuator materials, i.e., the stresses in the actuators and the maximum available actuation strains, on stress reduction were studied for two load cases, namely, a fatigue load case and an extreme load case. The fatigue load case was selected to demonstrate the effectiveness of active stress alleviation when the loads are repetitive in nature. Civil aircraft upper wing skins experience this kind of repetitive compressive load. The extreme load case corresponds to the loading when they are not repetitive in nature. We used a large plate with a small hole under uniaxial loading throughout this study.

Chapter 2 investigates the magnitude of the possible reduction obtained in stress concentration factor with ideal actuators for an isotropic plate and a composite plate with a hole. This was done largely to probe the potential of active stress alleviation. The effect of axisymmetric partial-thickness actuation was investigated in Chapter 3. The effectiveness of piezoelectric actuators in reducing stress concentration factor, with realistic limits on actuator stresses and actuation strains were examined for the fatigue load case and the extreme load case in Chapter 4 and Chapter 5, respectively. Chapter 6 offers some concluding remarks.

This investigation started as a team work and Markku J. Palanterä (visiting stu-

dent from Helsinki University of Technology, Finland), Dr. Mohammed H. Kadivar (visiting professor from Shiraj University, Iran) and I worked under the supervision of Dr. Raphael T. Haftka. Palanterä contributed to finite element based optimization of ideal actuators, section 2.2.5 and Dr. Kadivar contributed to the analytical study of axisymmetric partial-thickness actuation, Chapter 3.

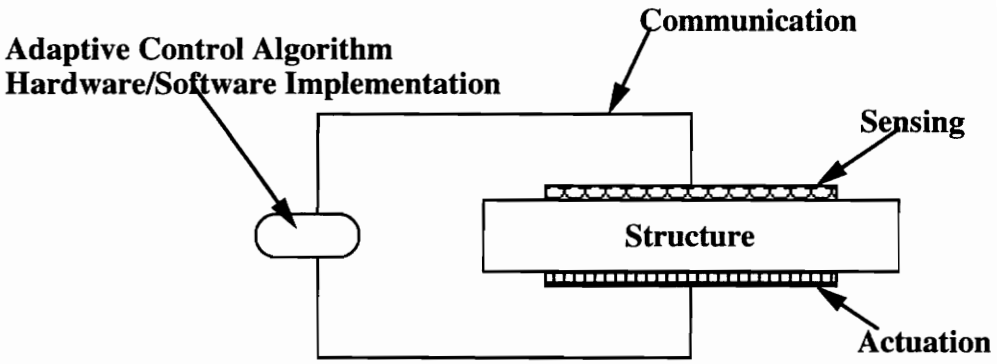

Figure 1.1 : Elements of Smart Structures [7]

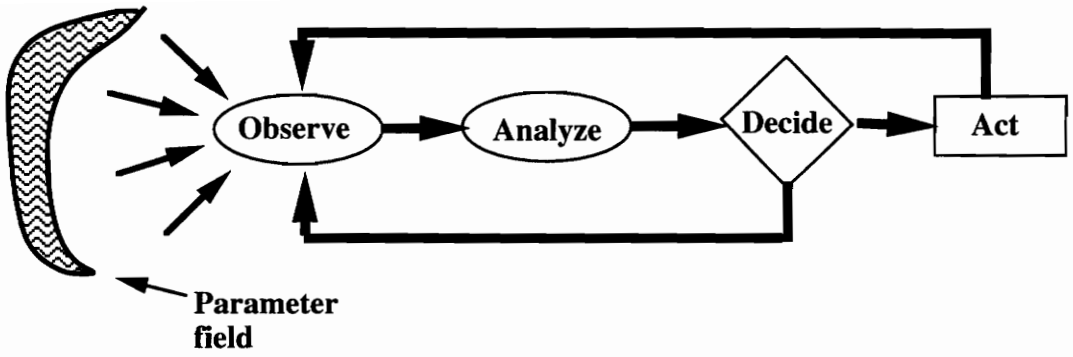

Figure 1.2 : Generic diagram illustrating the pattern of activity in a smart structure [7]

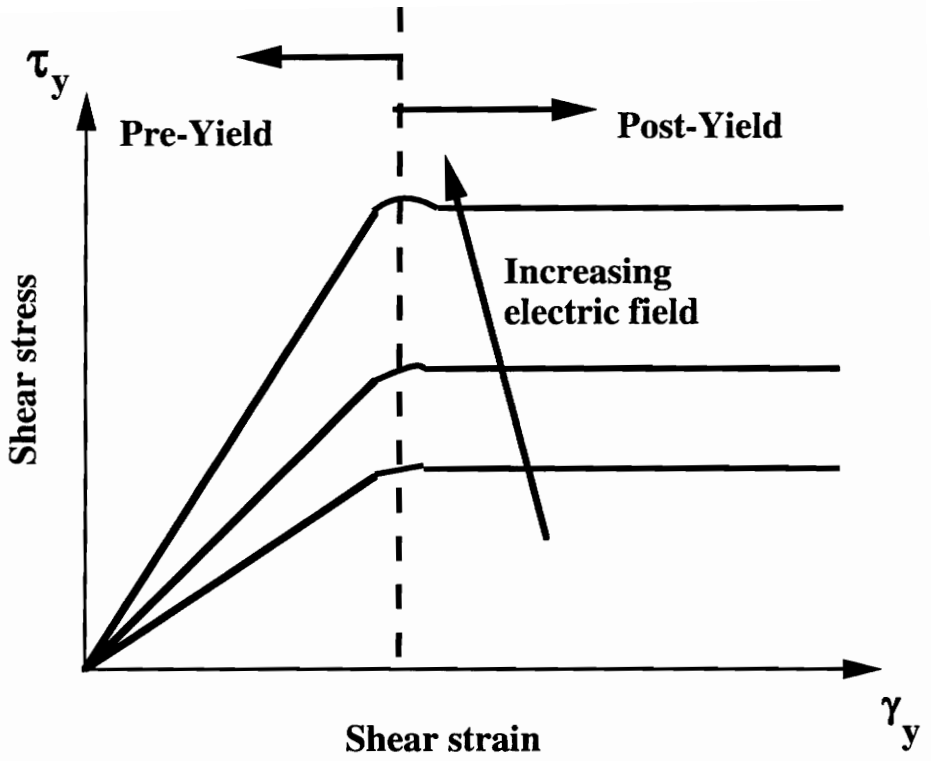

Figure 1.3 : Idealized constitutive shear behavior of ER materials

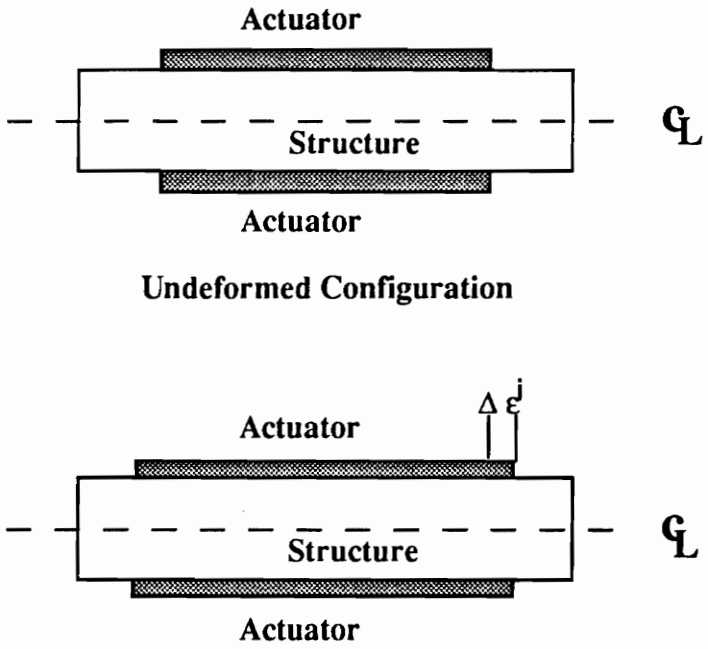

Figure 1.4 : Actuator/substrate geometry

CHAPTER 2

STRESS REDUCTION USING IDEAL ACTUATORS

2.1 IDEAL ACTUATORS

The objective of our work, as discussed in the previous chapter, was to show the effectiveness of active stress alleviation. We started by considering an ideal case with few physical limitations for the purpose of probing the limits of active stress reduction. We used the entire thickness of the plate for actuation, and assumed that the mechanical properties of the actuators are the same as that of the plate. We also did not place any limits on the magnitude of applied actuation strains, or considered other physical limitations of the actuators.

2.2 ISOTROPIC PLATE WITH A HOLE

2.2.1 Problem Definition

A 0.1 inch thin 30 inch square plate with a 1 inch diameter circular hole under uniaxial tensile loading S = 10 ksi, as shown in Figure 2.1, was used throughout this study. The plate is made of aluminum with Young's modulus E = 10 Msi and Poisson's ratio ν = 0.3. The plate was treated analytically as an infinite plate. The radial, tangential, and shear stress distribution for this case are given by Timoshenko [55]

$$\sigma_r^M = \frac{S}{2}\left[1 - \left(\frac{A}{r}\right)^2\right] + \frac{S}{2}\left[1 + 3\left(\frac{A}{r}\right)^4 - 4\left(\frac{A}{r}\right)^2\right] cos2\theta, \tag{2.1}$$

$$\sigma_\theta^M = \frac{S}{2}\left[1 + \left(\frac{A}{2}\right)^2\right] - \frac{S}{2}\left[1 + 3\left(\frac{A}{r}\right)^4\right] cos2\theta, \tag{2.2}$$

$$\tau_{r\theta}^{M} = -\frac{S}{2}\left[1 - 3\left(\frac{A}{r}\right)^{4} + 2\left(\frac{A}{r}\right)^{2}\right] sin2\theta, \tag{2.3}$$

where A is the radius of the hole. Our goal was to reduce the stress concentration as measured by Von-Mises or the maximum shear stress criteria by adding axisymmetric and non-axisymmetric actuation strain fields throughout the entire thickness of the plate and over a minimal region of the plate. Without the actuation strain field, σ_{θ}^{M} varies from 3S to -S around the edge of the hole. Since it is the only nonzero stress component there, the stress concentration factor is 3. An axisymmetric actuation strain can lower that stress concentration no lower than 2 (when the variation will be between 2 and -2, Figure 2.2). Our goal was to achieve that reduction with the smallest possible region of applied actuation strains, and the smallest possible magnitude of the actuation strains. The actuation strains were simulated by applying temperature differences.

In the non-axisymmetric case, however, the stress concentration factor can be reduced below 2 because the stresses can be reduced at one point (i.e., $\theta = \pi/2$) without affecting stresses at other points (i.e., $\theta = 0$)

For the finite element analysis, a quarter plate model was analyzed using a commercially available finite element code Engineering Analysis Language (EAL). The finite element model in the vicinity of the hole is shown in Figure 2.3 and the complete finite element model is shown in Figure 2.4. The basic element mesh of the plate was formed by four-node quadrilateral elements. The hole region, as well as the transition from dense to coarser element mesh was modelled with 3-node triangular elements. The model consists of 234 three-node (E31) and 176 four-node (E41) membrane elements. The plate was loaded in unidirectional tension by applying a constant displacement at one end of the quarter plate model. Free movement in the direction perpendicular to the applied load was allowed. The outer edge was left free. Symmetry boundary conditions

were applied to the other two edges of the quarter plate model. The total number of active degrees of freedom in the model was 611. Axisymmetric actuation strain variation was applied separately to five constant- width rings of elements around the hole. The inner and outer radii of these rings were 0.500 - 0.515 inch, 0.515 - 0.530 inch, 0.530 - 0.580 inch, 0.580 - 0.650 inch, and 0.650 - 0.750 inch. In the non-axisymmetric case, the actuation strain distribution in the tangential direction was formed by dividing the five rings into constant strain sectors.

An applied displacement of 0.015 inch was used as the mechanical load in the analysis. This corresponds to nominal strain $\epsilon_\infty = 0.001$ and tensile stress $\sigma_\infty = 10$ ksi in the absence of the hole. From the analysis, the highest yield stresses for Von-Mises and maximum shear stress criteria were obtained as 28.45 ksi and 28.89 ksi, respectively. Since the analytical solution predicts 30 ksi for the equivalent stresses, all the numerical results were normalized corresponding to the analytical stress values.

Both analytical optimization methods and numerical optimization based on finite element simulations were used to obtain optimal axisymmetric and non-axisymmetric actuation strain distributions.

2.2.2 Problem Formulation

The total stresses at a radius r is given as

$$\sigma_r^{tot} = \sigma_r^M + \sigma_r^I, \tag{2.4}$$

$$\sigma_\theta^{tot} = \sigma_\theta^M + \sigma_\theta^I, \tag{2.5}$$

$$\tau_{r\theta}^{tot} = \tau_{r\theta}^M + \tau_{r\theta}^I, \tag{2.6}$$

where σ_r^I , σ_θ^I and $\tau_{r\theta}^I$ are the radial, tangential and shear stresses due to actuation strains.

For the optimization, we seek the actuation strain distribution that minimizes the maximum equivalent stress in the plate, where for equivalent stress we use either the Von-Mises stress (Figure 2.5)

$$\sigma_{eq} = \sigma_V = \sqrt{\sigma_1^2 - \sigma_1\sigma_2 + \sigma_2^2}, \tag{2.7}$$

where σ_1 and σ_2 are the principal stresses and are defined as

$$\sigma_{1,2} = \frac{\sigma_r^{tot} + \sigma_\theta^{tot}}{2} \pm \sqrt{\frac{(\sigma_r^{tot} - \sigma_\theta^{tot})^2}{4} + \tau_{r\theta}^{tot^2}}, \tag{2.8}$$

or an equivalent stress based on the maximum shear stress criterion, given by (Figure 2.6)

$$\sigma_{eq} = \sigma_{MS} = |\sigma_1 - \sigma_2|, \tag{2.9}$$

when σ_1 and σ_2 are of the opposite sign. When σ_1 and σ_2 carry the same sign, then

$$\sigma_{eq} = \sigma_{MS} = max\,(|\sigma_1|, |\sigma_2|)\,. \tag{2.10}$$

The stress concentration factor was defined as the ratio of the maximum equivalent stress to the applied stress (i.e., σ_{eq} /S).

The maximum equivalent stress is not a smooth function of the design variables, and this nonsmoothness poses difficulties for the optimization algorithms. This problem was solved by standard device of adding the value of the maximum equivalent stress, σ_{max}, as an additional design variable. The optimization problem was then formulated as

$$\begin{aligned} &minimize \quad \sigma_{max} \\ &such\ that \quad \sigma_{eq}^j(\epsilon_k^i) \ \leq \ \sigma_{max}, \quad j = 1, ..., n_e, \end{aligned} \tag{2.11}$$

where ϵ_k^i, k=1,2,...,n are design variables, which are the values of the actuation strains in n regions of the plate or the values of multipliers that control the amplitudes of the assumed actuation strain distributions. The other design variable is σ_{max} , which is

also the objective function. The constraints require that the equivalent stress, σ_{eq} lower than σ_{max} at n_e element centers which were selected to represent the possible critical areas of the plate. Because it is expected that large values of actuation strain would be difficult to realize, optimizations were also performed with constraints on the magnitude of the actuation strains. Optimization was carried out by sequential linear programming (SLP) using the MINOS package [56].

2.2.3 Sequential Linear Programming Strategy

The SLP problem was formulated as described below. The partial derivatives of the equivalent stress with respect to each of the applied actuation strains were calculated by forward differences (step size $\Delta\epsilon^i{}_l = 10^{-10}$). The equivalent stress for an actuation strain distribution can be approximated linearly at each of the n_e points as

$$\left(\sigma^j_{eq}\right) \simeq \left(\sigma^j_{eq}\right)_o + \sum_{l=1}^{n} \Delta\epsilon^i{}_l \left(\frac{\partial \sigma^j_{eq}}{\partial \epsilon^i{}_l}\right)_o , \tag{2.12}$$

where subscript o denotes the configuration about which the equivalent stresses were approximated. The inequality constraint

$$\left(\sigma^j_{eq}\right) \leq \sigma_{max}, \quad j = 1, \ldots n_e, \tag{2.13}$$

can then be expressed in matrix form as

$$[A]\{x\} \geq \{\sigma^j_{eq}\}_o, \tag{2.14}$$

where $\{x\}$ is the design variable vector, i.e. $[\sigma_{max}, \Delta\epsilon^i{}_1, \Delta\epsilon^i{}_2, ..., \Delta\epsilon^i{}_n]^T$, and

$$[A] = \begin{pmatrix} 1 & -\left(\frac{\partial \sigma^1_{eq}}{\partial \epsilon^i{}_1}\right) & -\left(\frac{\partial \sigma^1_{eq}}{\partial \epsilon^i{}_2}\right) & \cdots & -\left(\frac{\partial \sigma^1_{eq}}{\partial \epsilon^i{}_n}\right) \\ 1 & -\left(\frac{\partial \sigma^2_{eq}}{\partial \epsilon^i{}_1}\right) & -\left(\frac{\partial \sigma^2_{eq}}{\partial \epsilon^i{}_2}\right) & \cdots & -\left(\frac{\partial \sigma^2_{eq}}{\partial \epsilon^i{}_n}\right) \\ \vdots & \vdots & \ddots & \vdots & \\ 1 & -\left(\frac{\partial \sigma^{n_e}_{eq}}{\partial \epsilon^i{}_1}\right) & -\left(\frac{\partial \sigma^{n_e}_{eq}}{\partial \epsilon^i{}_2}\right) & \cdots & -\left(\frac{\partial \sigma^{n_e}_{eq}}{\partial \epsilon^i{}_n}\right) \end{pmatrix}. \tag{2.15}$$

2.2.4 Analytical Optimization

Analytical optimization was carried out for both axisymmetric and non-axisymmetric actuation strain distributions.

2.2.4.1 Axisymmetric Case

As mentioned earlier, the plate was treated analytically as an infinite plate. The radial and tangential strains due to actuation strains in the plate can be written as

$$\epsilon_r^I = \frac{1}{E}(\sigma_r^I - \nu\sigma_\theta^I) + \epsilon_r^i \ , \tag{2.16}$$

$$\epsilon_\theta^I = \frac{1}{E}(\sigma_\theta^I - \nu\sigma_r^I) + \epsilon_\theta^i \ , \tag{2.17}$$

where ϵ_r^i , ϵ_θ^i are the radial and tangential actuation strains. For the axisymmetric response the compatibility equation can be written as

$$\epsilon_\theta^I - \epsilon_r^I + r\frac{d\epsilon_\theta^I}{dr} = 0, \tag{2.18}$$

and the equilibrium equation as

$$\sigma_\theta^I = \frac{d}{dr}(r\sigma_r^I) \ . \tag{2.19}$$

Substituting for ϵ_r^I and ϵ_θ^I from equations (2.16) and (2.17) and making use of the equilibrium equations, we obtain the compatibility equation in the following form

$$r\frac{d}{dr}(\frac{1}{r}\frac{d}{dr}(r^2\sigma_r^I)) = -Er\frac{d\epsilon_\theta^i}{dr} - E(\epsilon_\theta^i - \epsilon_r^i) \ . \tag{2.20}$$

Integrating the above equation with free edge boundary conditions at r=A and at r $\rightarrow \infty$, we obtain

$$\begin{aligned}\sigma_r^I =& \frac{E}{r^2}\int_A^r \epsilon_\theta^i \rho d\rho - \frac{E}{r^2}\int_A^r \int_A^{\rho_1} \frac{\rho_1}{\rho}(\epsilon_\theta^i - \epsilon_r^i) d\rho d\rho_1 \\ &+ \frac{E}{2}\int_A^r \frac{(\epsilon_\theta^i - \epsilon_r^i)}{\rho} d\rho - \frac{EA^2}{2r^2}\int_A^r \frac{(\epsilon_\theta^i - \epsilon_r^i)}{\rho} d\rho \ ,\end{aligned} \tag{2.21}$$

and substituting σ_r^I in the equilibrium equation (2.19), we get

$$\begin{aligned}\sigma_\theta^I =& \frac{E}{r^2}\int_A^r \epsilon_\theta^i \rho d\rho - \frac{E}{r^2}\int_A^r \int_A^{\rho_1} \frac{\rho_1}{\rho}(\epsilon_\theta^i - \epsilon_r^i) d\rho d\rho_1 \\ &+ \frac{E}{2}\int_A^r \frac{(\epsilon_\theta^i - \epsilon_r^i)}{\rho} d\rho - \frac{EA^2}{2r^2}\int_A^r \frac{(\epsilon_\theta^i - \epsilon_r^i)}{\rho} d\rho \\ &- E\int_A^r \frac{(\epsilon_\theta^i - \epsilon_r^i)}{\rho} d\rho - E\epsilon_\theta^i \ .\end{aligned} \tag{2.22}$$

If we consider axisymmetric isotropic actuation strains $\epsilon_r^i = \epsilon_\theta^i = \epsilon^i$, the radial and tangential stresses are obtained as

$$\sigma_r^I = -\frac{E}{r^2}\int_A^r \epsilon^i \rho d\rho \ , \tag{2.23}$$

$$\sigma_\theta^I = \frac{E}{r^2}\int_A^r \epsilon^i \rho d\rho - E\epsilon^i \ . \tag{2.24}$$

From equations (2.23) and (2.24), it can be seen that applying axisymmetric actuation strains in a circular ring will cause compressive stresses in the ring and tensile stresses in the exterior (larger radii) of the ring, without affecting the stresses in the interior (smaller radii) area. We also found that the tangential stresses exterior to the ring will be small compared to the stresses in the ring. This can be illustrated more clearly if we assume that constant strains ϵ_r^i and ϵ_θ^i are applied over the region $R_1 \leq r \leq R_2$. Then the radial and tangential stresses in the three regions, shown in Figure 2.7 are obtained as

$\underline{A < r < R_1}$

$$\sigma_r^I = \frac{E(\epsilon_\theta^i - \epsilon_r^i)}{2}\left[1 - \left(\frac{A}{r}\right)^2\right] ln\left(\frac{R_2}{R_1}\right), \tag{2.25}$$

$$\sigma_\theta^I = \frac{E(\epsilon_\theta^i - \epsilon_r^i)}{2}\left[1 + \left(\frac{A}{r}\right)^2\right] ln\left(\frac{R_2}{R_1}\right), \tag{2.26}$$

$R_1 < r < R_2$

$$\sigma_r^I = -\frac{E\epsilon_\theta^i}{2}\left[1-\left(\frac{R_1}{r}\right)^2\right] - \frac{E(\epsilon_\theta^i-\epsilon_r^i)}{2}\left[ln\left(\frac{r}{R_1}\right) - \frac{1}{2} + \frac{1}{2}\left(\frac{R_1}{r}\right)^2\right] + \frac{E(\epsilon_\theta^i-\epsilon_r^i)}{2}\left[1-\left(\frac{A}{r}\right)^2\right] ln\left(\frac{R_2}{R_1}\right), \tag{2.27}$$

$$\sigma_\theta^I = \frac{E\epsilon_\theta^i}{2}\left[1-\left(\frac{R_1}{r}\right)^2\right] - \frac{E(\epsilon_\theta^i-\epsilon_r^i)}{2}\left[ln\left(\frac{r}{R_1}\right) + \frac{1}{2} - \frac{1}{2}\left(\frac{R_1}{r}\right)^2\right] + \frac{E(\epsilon_\theta^i-\epsilon_r^i)}{2}\left[1+\left(\frac{A}{r}\right)^2\right] ln\left(\frac{R_2}{R_1}\right) - E\epsilon_\theta^i, \tag{2.28}$$

$r > R_2$

$$\sigma_r^I = -\frac{E\epsilon_\theta^i}{2r^2}\left(R_2^2-R_1^2\right) - \frac{E(\epsilon_\theta^i-\epsilon_r^i)}{2}\left(\frac{A}{r}\right)^2 ln\left(\frac{R_2}{R_1}\right) + \frac{E\left(\epsilon_\theta^i-\epsilon_r^i\right)}{4r^2}\left(R_2^2-R_1^2\right), \tag{2.29}$$

$$\sigma_\theta^I = \frac{E\epsilon_\theta^i}{2r^2}\left(R_2^2-R_1^2\right) + \frac{E(\epsilon_\theta^i-\epsilon_r^i)}{2}\left(\frac{A}{r}\right)^2 ln\left(\frac{R_2}{R_1}\right) - \frac{E\left(\epsilon_\theta^i-\epsilon_r^i\right)}{4r^2}\left(R_2^2-R_1^2\right), \tag{2.30}$$

We can see from equations (2.25) and (2.26) that when the applied actuation strains are isotropic, i.e., $\epsilon_r^i = \epsilon_\theta^i = \epsilon^i$, the radial and tangential stresses in the region interior to the actuation region are zero. If the applied actuation strains are not isotropic, i.e., $\epsilon_r^i \neq \epsilon_\theta^i$, then we can see from the equations (2.25) and (2.26) that applying actuation strains to exterior rings will affect stresses in the interior rings. Figure 2.8 shows the stresses when actuation strains are applied over the region $1.16 \leq r/A \leq 1.30$, which corresponds to the 4th ring as shown in the FE model in Figure 2.3, and $\epsilon_r^i = \epsilon_\theta^i = \epsilon^i$. It can be seen that there is no effect on the interior of the region where actuation strains are applied. It can also be seen that the tangential stresses are compressive and much higher in the region where actuation strains are applied, compared to the exterior region.

Radial stresses are small in magnitude compared to the tangential stresses. Figure 2.9 shows the stresses when $\epsilon_r^i = 0$ and we can see that the radial stresses are small compared to the tangential stresses, especially in the region where actuation strains are applied. When $\epsilon_\theta^i = 0$ (Figure 2.10), both tangential and radial stresses are small compared to the previous two cases.

For the case of isotropic actuation, the total radial and tangential stresses at radius r due to mechanical load and actuation action can be written as

$$\sigma_r^{tot} = \sigma_r^M - \frac{E}{r^2}\int_A^r \epsilon^i \rho d\rho \ , \tag{2.31}$$

$$\sigma_\theta^{tot} = \sigma_\theta^M + \frac{E}{r^2}\int_A^r \epsilon^i \rho d\rho - E\epsilon^i \ , \tag{2.32}$$

Our objective was to reduce the equivalent stresses (σ_V or σ_{MS}) to 2S by applying actuation strains to the smallest possible region. Optimum actuation strain distribution to minimize tangential stress was obtained first because closed-form solution is possible. The optimum was obtained based on the condition that $\sigma_\theta^{tot}(\pi/2)$ is equal to 2S throughout the region where actuation strains were applied. This condition implies that $d\sigma_\theta/dr = 0$ at $\theta = \pi/2$. Substituting from equation (2.2) into equation (2.32), multiplying by r^2 and differentiating this equation at $\theta = \pi/2$ with respect to r, we get

$$[\epsilon^i(r)]\prime + \frac{1}{r}\epsilon^i(r) = -\frac{S}{E}(\frac{2}{r} + 3\frac{A^4}{r^5}) \ , \tag{2.33}$$

where a prime denotes derivative with respect to r. The condition $\sigma_\theta^{tot} = 2S$ at r = A gives us boundary condition that at r = A, $\epsilon^i = S/E$. Solving equation (2.33) with this boundary condition we get

$$\epsilon^i(r) = \frac{S}{E}[2\frac{A}{r} + (\frac{A}{r})^4 - 2] \ , \tag{2.34}$$

with $\epsilon^i(r)$ reaching zero for r/A = 1.25 (Figure 2.11). For a general case, where K is the desired stress concentration factor, equation (2.34) becomes

$$\epsilon^r(r) = \frac{S}{E}[K\frac{A}{r} + (\frac{A^4}{r^4}) + 2(1-K)] \ . \tag{2.35}$$

Optimal actuation stress distributions for Von-Mises and maximum shear stress criteria were obtained by differentiating equations (2.7), (2.9), (2.10), (2.31) and (2.32) with respect to r and integrating them numerically by IMSL subroutine DIVPRK with initial values at r = A; $\sigma_{eq} = 2S$, $\sigma_r = 0$, and $\epsilon^i = S/E$.

The optimal actuation strain distributions for Von-Mises stress and maximum shear stress criteria are shown in Figure 2.12. We can see that for these two criteria, the actuation strains applied over $r \leq 1.21A$, and $r \leq 1.25A$, respectively. The Von-Mises stress criterion required a smaller region over which actuation strains need to be applied. The optimal actuation strain distribution for this case (Von-Mises) can be approximated closely by the expression

$$\epsilon^r(r) = \frac{S}{E}[K(\frac{A}{r})^2 + (\frac{A}{r})^{\frac{5}{2}} + 2(1-K)] \ , \tag{2.36}$$

for K = 2, as can be seen from Figure 2.12, and we can see that they compare quite well. The same problem was solved with an additional requirement that only tangential actuation strains could be applied (i.e. $\epsilon^i_r = 0$) to better simulate fiber type actuators. The optimal actuation strains distributions for Von-Mises and maximum shear stress criteria are shown in Figure 2.13. They were found to be about 12 percent higher than those required for the isotropic actuation strain case.

2.2.4.2 Non-axisymmetric Case

Analytical solutions of stresses for non-axisymmetric actuation strain distributions were obtained using a stress function $\phi(r,\theta)$ developed by Forray [57] for the case of ap-

plied temperature T(r, θ). The plane-stress equations of equilibrium and compatibility are satisfied if the stress function $\phi(r,\theta)$ is obtained such that

$$\nabla^4\phi = -E\alpha\nabla^2 T \ , \tag{2.37}$$

where

$$\begin{aligned} \nabla^2 =&(\frac{\partial^2}{\partial r^2}) + (\frac{1}{r})(\frac{\partial}{\partial r}) + (\frac{1}{r^2})(\frac{\partial^2}{\partial\theta^2}) \\ \nabla^4 =&\nabla^2\nabla^2 \ , \end{aligned} \tag{2.38}$$

and α is the coefficient of thermal expansion. For the isotropic actuation strains, $\epsilon_r^i = \epsilon_\theta^i = \epsilon^i$, we can replace αT by ϵ^i. If the prescribed actuation strain distribution $\epsilon^i(r,\theta)$ can be expressed in the form

$$\epsilon^i(r,\theta) = P_0(r) + \sum_{i=1}^{\infty}[P_n(r)cosn\theta + Q_n(r)sinn\theta] \ , \tag{2.39}$$

then the complete solution of equation (2.37) can be given as

$$\phi = \phi_c + \phi_p \ , \tag{2.40}$$

where ϕ_c and ϕ_p are the complementary solution and particular solution, respectively. General expressions for these can be found in Forray [57] and are reproduced below.

$$\phi_p = g_0(r) + \sum_{i=1}^{\infty}[g_n(r)cosn\theta + h_n(r)sinn\theta] \ , \tag{2.41}$$

$$\begin{aligned} \phi_c =&a_0 logr + b_0 r^2 + c_0 r^2 logr + d_0 r^2\theta + a_0'\theta \\ &+(a_1/2)r\theta sin\theta + (b_1 r^3 + a_1' r^{-1} + b_1' r logr)cos\theta \\ &-(c_1/2)r\theta sin\theta + (d_1 r^3 + c_1' r^{-1} + d_1' r logr)sin\theta \\ &+\sum_{n=2}^{\infty}(a_n r^n + b_n r^{n+2} + a_n' r^{-n} + b_n' r^{-n+2})cosn\theta \\ &+\sum_{n=2}^{\infty}(c_n r^n + d_n r^{n+2} + c_n' r^{-n} + d_n' r^{-n+2})sinn\theta \ , \end{aligned} \tag{2.42}$$

where the functions g_n and h_n are obtained from

$$\begin{aligned} g_n &= r^{-n} \int \Upsilon^{2n-1} \int P_n(\rho)\rho^{1-n} d\rho d\Upsilon \ , \\ h_n &= r^{-n} \int \Upsilon^{2n-1} \int Q_n(\rho)\rho^{1-n} d\rho d\Upsilon \ . \end{aligned} \tag{2.43}$$

The stress components are obtained from ϕ by

$$\begin{aligned} \sigma_r &= \frac{1}{r}\frac{\partial \phi}{\partial r} + \frac{1}{r^2}\frac{\partial^2 \phi}{\partial \theta^2} \ , \\ \sigma_\theta &= \frac{\partial^2 \phi}{\partial r^2} \ , \\ \tau_{r\theta} &= \frac{\partial}{\partial r}[\frac{1}{r}\frac{\partial \phi}{\partial \theta}] \ . \end{aligned} \tag{2.44}$$

Similar to axisymmetric case, actuation strains were applied over the region $A \leq r \leq R$, where R = 1.5A. The non-axisymmetric actuation strain distribution was chosen as

$$\epsilon^i_{Nx}(r,\theta) = -\epsilon^i(r) cos2\theta \ . \tag{2.45}$$

The above actuation strain distribution was chosen because it produces compressive stresses over $45^0 \leq \theta \leq 90^0$ and tensile stresses over $0^0 \leq \theta \leq 45^0$ of the plate and hence will reduce stress concentration over both the critical regions.

The particular solution ϕ_p for the region where actuation strains were applied (i.e., $r \leq R$), in the form of equation (2.45) was obtained as

$$\phi_p = [\frac{E}{r^2}\int_A^r \Upsilon^3 \int_A^\Upsilon \frac{\epsilon^i_{Nx}}{\rho} d\rho d\Upsilon] cos2\theta \ , \tag{2.46}$$

and ϕ_p for the region exterior to this region (i.e., $r \geq R$) was obtained as

$$\phi_p = [\frac{E}{r^2}\int_A^R \Upsilon^3 \int_A^\Upsilon \frac{\epsilon^i_{Nx}}{\rho} d\rho d\Upsilon + \frac{E}{r^2}\int_R^r \Upsilon^3 \int_A^R \frac{\epsilon^i_{Nx}}{\rho} d\rho d\Upsilon] cos2\theta \ . \tag{2.47}$$

In order to ensure single valuedness of the stress and displacement components for traction-free boundaries, ϕ_c assumes the reduced from

$$\phi_c = a_0 log r + b_0 r^2 + (a_2 r^2 + b_2 r^4 + a_2' r^{-2} + b_2') cos2\theta \ . \tag{2.48}$$

Using boundary conditions $\sigma_r = \tau_{r\theta} = 0$ at r = A and $r \to \infty$, we get the expressions for the stress components

<u>$A < r < R$</u>

$$\begin{aligned}\sigma_r =&[\frac{E}{2}(3+3(\frac{A}{r})^4-4(\frac{A}{r})^2)\int_A^R \frac{\epsilon - Nx^i}{\rho}d\rho]cos2\theta \\ &-[\frac{6E}{r^4}\int_A^r \Upsilon^3 \int_A^R \frac{\epsilon - Nx^i}{\rho}d\rho]cos2\theta \ ,\end{aligned} \tag{2.49}$$

$$\begin{aligned}\sigma_\theta =& -[\frac{E}{2}(1+3(\frac{A}{r})^4)\int_A^R \frac{\epsilon - Nx^i}{\rho}d\rho]cos2\theta \\ &+[E\epsilon - Nx^i - E\int_A^R \frac{\epsilon - Nx^i}{\rho}d\rho + \frac{6E}{r^4}\int_A^r \Upsilon^3 \int_A^R \frac{\epsilon - Nx^i}{\rho}d\rho]cos2\theta \ ,\end{aligned} \tag{2.50}$$

$$\begin{aligned}\tau_{r\theta} =&[\frac{E}{2}(3+3(\frac{A}{r})^4-2(\frac{A}{r})^2)\int_A^R \frac{\epsilon - Nx^i}{\rho}d\rho]sin2\theta \\ &-[\frac{6E}{r^4}\int_A^r \Upsilon^3 \int_A^R \frac{\epsilon - Nx^i}{\rho}d\rho]sin2\theta \ .\end{aligned} \tag{2.51}$$

<u>$r > R$</u>

$$\begin{aligned}\sigma_r =&[\frac{E}{2}(3+3(\frac{A}{r})^4-4(\frac{A}{r})^2)\int_A^R \frac{\epsilon - Nx^i}{\rho}d\rho]cos2\theta \\ &-[\frac{6E}{r^4}\int_A^R \Upsilon^3 \int_A^R \Upsilon\frac{\epsilon - Nx^i}{\rho}d\rho + \frac{6E}{r^4}\int_R^r \Upsilon^3 \int_A^R \frac{\epsilon - Nx^i}{\rho}d\rho]cos2\theta \ ,\end{aligned} \tag{2.52}$$

$$\begin{aligned}\sigma_\theta =& -[\frac{E}{2}(3+3(\frac{A}{r})^4)\int_A^R \frac{\epsilon - Nx^i}{\rho}d\rho]cos2\theta \\ &+[\frac{6E}{r^4}\int_A^R \Upsilon^3 \int_A^R \Upsilon\frac{\epsilon - Nx^i}{\rho}d\rho + \frac{6E}{r^4}\int_R^r \Upsilon^3 \int_A^R \frac{\epsilon - Nx^i}{\rho}d\rho]cos2\theta \ ,\end{aligned} \tag{2.53}$$

$$\begin{aligned}\tau_{r\theta} =&[\frac{E}{2}(3+3(\frac{A}{r})^4-2(\frac{A}{r})^2)\int_A^R \frac{\epsilon - Nx^i}{\rho}d\rho]sin2\theta \\ &-[\frac{6E}{r^4}\int_A^R \Upsilon^3 \int_A^R \Upsilon\frac{\epsilon - Nx^i}{\rho}d\rho + \frac{6E}{r^4}\int_R^r \Upsilon^3 \int_A^R \frac{\epsilon - Nx^i}{\rho}d\rho]sin2\theta \ ,\end{aligned} \tag{2.54}$$

To optimize the actuation strain distribution, the actuation strain was assumed to be of the form

$$\epsilon^i(r,\theta) = \lambda_A \epsilon^i_A(r) - \lambda_N \epsilon^i_N(r) cos2\theta \ . \tag{2.55}$$

Equations (2.35) and (2.36) were used as $\epsilon^i_A(r)$ and $\epsilon^i_N(r)$, respectively. The values of K were adjusted such that the actuation strains become zero at r = 1.5A. The two variables λ_A and λ_N were found by sequential linear programming problem using MINOS. The stress constraints were applied at points spaced by intervals of $\Delta r = 0.05$ inch in the radial direction and $\Delta\theta = 5^o$ along the tangential direction over the annular region $A \leq r \leq 1.6A$ of the quarter plate. The stress concentration factor for maximum shear stress criterion was reduced to 1.45 and corresponding values of λ_A and λ_N were obtained as 0.7397 and 0.5681, respectively. The actuation strain distributions at $\theta = 0^o, 45^o$, and 90^o are shown in Figure 2.14. The maximum required actuation strain in this case was 1.84 S/E as compared to S/E in the axisymmetric case. The stress contours are shown in Figure 2.15. The stress concentration factor for Von-Mises stress criterion was reduced to 1.58 and corresponding values of λ_A and λ_N were obtained as 0.7397 and 0.4305, respectively. The maximum required actuation strain was 1.64 S/E. The actuation strain distributions at $\theta = 0^o, 45^o$, *and* 90^o are shown in Figure 2.16 and the stress contours are shown in Figure 2.17.

Because the non-axisymmetric analytical optimization was performed with only two design variables, it is not clear whether the stress concentration can be reduced much further by a more general non-axisymmetric actuation strain distribution. This was checked by a procedure based on the finite element model described in the next section. It is shown there that the distribution of equation (2.55) is very close to optimal.

2.2.5 Finite Element Based Optimization

2.2.5.1 Axisymmetric Case

The analytical solution for the tangential stress minimization of equation (2.34) was used as a starting point for the numerical optimization. The optimal applied strain distributions for the two stress criteria are shown in Figure 2.18 along with the results obtained from analytical solutions. Considering the fact that we solved only a five-variable case for the finite element based optimization, we can see from the Figure 2.18 that the results are quite close. The stress concentration factors for Von-Mises and maximum shear stress criteria were reduced to 1.97 and 1.98, respectively. Equivalent stress distributions for Von-Mises and maximum shear stress criteria, along with the stress distribution obtained analytically, are shown in Figure 2.19 and Figure 2.20, respectively. The same problem was solved with additional requirement that only tangential actuation strains could be applied to better simulate the fiber-type actuators. The optimal strain distributions, which gave the same reduction in the stress concentration factor, were about 10 % higher than the strains required for the isotropic case.

2.2.5.2 Non-axisymmetric Case

Strains were first applied to five rings for a sector $45^o \leq \theta \leq 90^o$ in the quarter plate model (Figure 2.21). The optimal actuation strain distributions are shown in Figure 2.22. The stress concentration factors, as measured by the Von-Mises and maximum shear stress criteria, were reduced to 1.68 and 1.78, respectively (Table 2.1). Next, strains were also applied to the sector $0^o \leq \theta \leq 45^o$ (Figure 2.23), thus leading to a ten-variable representation of strain distributions. Very little improvement was observed. Results are shown in Table 2.1 and Table 2.2. Finally, the strain distribution was obtained by

dividing the quarter plate into four sectors, 22.5^o each (Figure 2.24), leading to twenty-variable representation of strain distribution. The stress concentrations for Von-Mises and maximum shear stress criteria were reduced to 1.62 and 1.65, respectively. Optimal actuation strain distributions for this case are given in Table 2.3. It can be seen that large actuation strains, upto 3.66 S/E, were required in some cases.

Due to limits imposed by the present technology on the available actuation strains, we may not be able to generate large actuation strains. To account for such technology limits, we investigated the effect of available actuation strain limits on the reduction in stress concentration factor. Optimal actuation strain distributions to minimize equivalent stresses for Von-Mises and maximum shear stress criteria were found for four different cases, in which the actuation strain values were constrained. The four cases were: (1) $\epsilon^i \geq 0$, (2) -1.38 S/E $\leq \epsilon^i \leq$ 1.38 S/E , (3) $0 \leq \epsilon^i \leq$ 1.38 S/E , (4) $0 \leq \epsilon^i \leq$ S/E . The stress concentration factors are shown in Table 2.4 and indicate that substantial reduction in the SCF can be achieved even with these limits on the magnitude of the actuation strains. In case (4), the maximum applied actuation strain was the same as that in the axisymmetric case. However, the SCFs were reduced to 1.72 and 1.71 for Von-Mises and maximum shear stress criteria, respectively as compared to 2.0 for the axisymmetric case. The optimal actuation strain distributions are presented in Tables 2.5 through 2.8.

2.2.5.3 FE check of Non-axisymmetric Analytical Optimum

The optimal non-axisymmetric actuation strain distribution, obtained analytically in the previous section, was checked using the finite element model. For the maximum shear stress criterion, the maximum stress concentration factor observed was 1.51 which was about 4.1 % higher than that obtained in the analytical case. The discrepancy may

be due to discretization error. In case of Von-Mises stress the discrepancy was about 1.3 %.

In order to check how close to the optimum is the two-parameter analytical solution, perturbations in the actuation strains at 40 nodes of the finite element model were selected as design variables and optimized to reduce the stress concentration. It was found that with perturbations limited to 10 % in the maximum actuation strains, it was possible to improve the SCF by only 0.04 %. This indicates that the two parameter optimum, based on equation (2.55) is very close in performance to the optimum.

2.3 Composite Plate with a Hole

In this section, the work of section 2.2 was extended to composite plates. The objective again was to find maximum possible reduction in the stress concentration factor in a composite plate with a hole by applying actuation strains in a small area near the hole. Numerical optimization based on finite element simulations was used to obtain axisymmetric and non-axisymmetric actuation strain distributions.

2.3.1 PROBLEM DEFINITION

A 30 inch square graphite/epoxy plate with a 1 inch diameter circular hole under in-plane tensile load (N_x), as shown in Figure 2.1 was used throughout this study. Two laminates with stacking sequences $(0_2^\circ/\pm 45^\circ/0_2^\circ)_s$ and $(\pm 45^\circ/0_2^\circ/\pm 45^\circ/0_2^\circ)_s$ were studied. The material properties are [58, page 10-8], E_1 = 2.944 x 10^7 psi, E_2 = 1.624 x 10^6 psi, and G_{12} = 1.218 x 10^5 psi and ν_{12} = 0.32.

To validate the finite element model, we compared stress concentration factors for the composite plate (defined as the ratios of the tangential stress resultant at the edge of the hole and away from the hole) to the experimental results of Hong and Crews [59]. The five-ring model used for our earlier study in section 2.2 did not give satisfactory results. The finite element model was refined and the region $A \leq r \leq 1.5A$ was divided into eleven rings as discussed in the previous section. The results are summarized in Table 2.9 and show good agreement.

The plate was modeled by a quarter plate finite element model using EAL. The finite element model in the vicinity of the hole is shown in Figure 2.25, and a complete finite element model is shown in Figure 2.26. The basic element mesh of the plate was formed by four-node quadrilateral elements. The transition region from dense to coarse element

mesh was modeled with three-node triangular elements. The model consists of 122 three-node (E33) and 880 four-node (E43) membrane elements. The plate was loaded in unidirectional tension by applying a constant displacement at one end of the quarter plate model. Free movement in the direction perpendicular to the applied load was allowed, and the outer edge was left free. Symmetry boundary conditions were applied to the other two edges of the quarter plate model. The number of active degrees of freedom in the model was 1219. Axisymmetric actuation strain variation was simulated by thermal loading and applied to eleven constant-width rings of elements around the hole. The outer radii of these rings were 0.509, 0.519, 0.531, 0.545, 0.561, 0.580, 0.603, 0.631, 0.664, 0.703 and 0.750 in.. In the non-axisymmetric case, the eleven rings were divided into constant strain sectors.

2.3.2 FAILURE CRITERION

The maximum strain criterion was chosen as the failure criterion for our study. With this criterion the material is said to have failed if one or more of the following inequalities is not satisfied [60].

$$\begin{aligned} \epsilon_{1c}^{*} < \epsilon_1 < \epsilon_{1t}^{*}, \\ \epsilon_{2c}^{*} < \epsilon_2 < \epsilon_{2t}^{*}, \\ |\gamma_{12}| < \gamma_{12}^{*}, \end{aligned} \tag{2.56}$$

where

ϵ_1, ϵ_2, γ_{12} = strains in principal material directions

ϵ_{1t}^{*}, (ϵ_{1c}^{*}) = allowable tensile (compressive) normal strain in the 1-direction

ϵ_{2t}^{*}, (ϵ_{2c}^{*}) = allowable tensile (compressive) normal strain in the 2-direction

γ_{12}^{*} = allowable shear strain in the 1-2 direction

The strength ratio (safety factor) R of this criterion is the lowest of three ratios of the maximum strain divided by the applied strain.

$$R_1 = \begin{cases} \epsilon_{1t}^*/\epsilon_1, & \text{if } \epsilon_1 \geq 0; \\ -\epsilon_{1c}^*/\epsilon_1, & \text{otherwise} \end{cases} \tag{2.57}$$

$$R_2 = \begin{cases} \epsilon_{2t}^*/\epsilon_2, & \text{if } \epsilon_1 \geq 0; \\ -\epsilon_{2c}^*/\epsilon_2, & \text{otherwise} \end{cases} \tag{2.58}$$

$$R_{12} = \gamma_{12}^*/|\gamma_{12}| \; ; \tag{2.59}$$

$$R = min(R_1, R_2, R_{12}) \; . \tag{2.60}$$

For the graphite/epoxy material chosen for our study, we have [58, page 10-8]

$$\begin{aligned} \epsilon_{1t}^* &= 17.24 \times 10^{-3}, \\ \epsilon_{1c}^* &= \; 7.59 \times 10^{-3}, \\ \epsilon_{2t}^* &= \; 5.00 \times 10^{-3}, \\ \epsilon_{2c}^* &= 13.39 \times 10^{-3}, \\ \gamma_{12}^* &= 11.67 \times 10^{-3}. \end{aligned} \tag{2.61}$$

As is common in aeronautical applications, it was assumed that beyond limit load matrix failure is acceptable, but not fiber failure. Since the ultimate load is 1.5 times the limit load, the maximum strains in 2 direction and 1-2 direction were multiplied by a factor of 1.5.

The stress concentration factor (SCF) was defined as the ratio of the safety factor away from the hole (R_∞) and that at the edge of the hole (R). Using maximum strain criterion, for an applied displacement of 0.015 inch, R_∞, R and SCF for the $(0_2^\circ/\pm 45^\circ/0_2^\circ)_s$ laminate were obtained as 9.8, 2.19, and 4.47, respectively. The critical element was the seventh element located at $\theta = 72^\circ$ in the 45° ply at the hole boundary. For the $(\pm 45^\circ/0_2^\circ/\pm 45^\circ/0_2^\circ)_s$ laminate, R_∞, R and SCF were obtained as 9.40,2.93, and 3.20 ,

respectively. In this laminate the first element, located at $\theta = 90°$ in the $\pm 45°$ plies, were the critical elements.

2.3.3 PROBLEM FORMULATION

For the optimization, we seek the actuation strain distribution that maximizes the safety factor for the laminate. The safety factor is not a smooth function of the design variables, and to avoid the problem of differentiability, we used the standard device of adding the value of the safety factor, R, as an additional design variable. The optimization problem was then formulated as

$$\begin{aligned} &maximize \quad R \\ &such\ that \quad R^j(\epsilon_k^i) \geq R, \quad j = 1, ..., n_e, \end{aligned} \tag{2.62}$$

where ϵ_k^i, k=1,2,...,n are design variables, which are the values of the actuation strains in n regions of the plate. The other design variable is R, which is also the objective function. The constraints require that the safety factor R^j for the element j is greater than R at n_e element centers which were selected to represent the possible critical areas of the plate. During the optimization, constraints were not applied to elements with very high values of R (low strains), but only to elements with R^j less than 5R. Because it is expected that large values of actuation strains would be difficult to realize, optimizations were also performed with constraints on the magnitude of the actuation strains. Optimization was carried out by sequential linear programming (SLP) using the MINOS package [56].

2.3.4 Sequential Linear Programming Strategy

The SLP problem was formulated as described below. The partial derivatives of the safety factor with respect to each of the applied actuation strains were calculated by forward differences (step size $\Delta\epsilon^i{}_l = 10^{-10}$). The safety factor for an actuation strain

distribution can be approximated linearly at each of the n_e points as

$$\left(R^j\right) \simeq \left(R^j\right)_o + \sum_{l=1}^{n} \Delta\epsilon^i{}_l \left(\frac{\partial R^j}{\partial \epsilon^i{}_1}\right)_o , \tag{2.63}$$

where subscript o denotes the configuration about which the safety factors were approximated. The inequality constraint

$$\left(R^j\right) \geq R, \quad j = 1, \ldots n_e, \tag{2.64}$$

can then be expressed in matrix form as

$$[A]\{x\} \leq \{R^j\}_o, \tag{2.65}$$

where $\{x\}$ is the design variable vector ,i.e. $[R, \Delta\epsilon^i{}_1, \Delta\epsilon^i{}_2, ..., \Delta\epsilon^i{}_n]^T$,

$$[A] = \begin{pmatrix} 1 & -\left(\frac{\partial R^1}{\partial \epsilon^i{}_1}\right) & -\left(\frac{\partial R^1}{\partial \epsilon^i{}_2}\right) & \cdots & -\left(\frac{\partial R^1}{\partial \epsilon^i{}_n}\right) \\ 1 & -\left(\frac{\partial R^2}{\partial \epsilon^i{}_1}\right) & -\left(\frac{\partial R^2}{\partial \epsilon^i{}_2}\right) & \cdots & -\left(\frac{\partial R^2}{\partial \epsilon^i{}_n}\right) \\ \vdots & \vdots & \ddots & \vdots & \\ 1 & -\left(\frac{\partial R^{n_e}}{\partial \epsilon^i{}_1}\right) & -\left(\frac{\partial R^{n_e}}{\partial \epsilon^i{}_2}\right) & \cdots & -\left(\frac{\partial R^{n_e}}{\partial \epsilon^i{}_n}\right) \end{pmatrix}, \tag{2.66}$$

.

2.3.5 RESULTS

As mentioned earlier, an applied displacement of 0.015 inch was used as the mechanical load in the analysis. This corresponds to nominal strain $\epsilon_\infty = 0.001$.

2.3.5.1 Unconstrained Actuation Strains

Axisymmetric actuation strain variation was simulated by thermal loading applied to eleven constant-width rings of element around the hole. To simulate non-axisymmetric actuation strain variation, the eleven rings were divided into 45 degree constant strain sectors (Figure 2.27), corresponding to 22-variable representation of the actuation strain

distribution and 22.5 degree constant strain sectors (Figure 2.28), corresponding to 44-variable representation of the actuation strain distribution. The optimal safety factors R and corresponding stress concentration factors (SCF) are shown in Table 2.10 and Table 2.11 for the $(0_2^\circ/\pm 45^\circ/0_2^\circ)_s$ laminate and $(\pm 45^\circ/0_2^\circ/\pm 45^\circ/0_2^\circ)_s$ laminate, respectively. Note that the optimization reduces SCF and increases the safety factor R by the same factor. The final results in Table 2.10 and Table 2.11 are comparable to results obtained in sections 2.2.4.2 and 2.2.5.2 for the isotropic case. However, since the original SCF for the isotropic case is 3.0, we see that the potential for improvement is greater for the composite case. The optimal actuation strain distributions for the axisymmetric case are shown in Figure 2.29 and Figure 2.30 for $(0_2^\circ/\pm 45^\circ/0_2^\circ)_s$ laminate and $(\pm 45^\circ/0_2^\circ/\pm 45^\circ/0_2^\circ)_s$ laminate, respectively. Optimal non-axisymmetric actuation strain distributions for $(0_2^\circ/\pm 45^\circ/0_2^\circ)_s$ laminate for two sector and four sector case are given in Table 2.12 and 2.13, respectively. The corresponding actuation strain distributions for $(\pm 45^\circ/0_2^\circ/\pm 45^\circ/0_2^\circ)_s$ laminate are shown in Table 2.14 and 2.15, respectively.

2.3.5.2 Effects of Limits on Available Actuation Strains

For the axisymmetric and non-axisymmetric actuation strain distributions, the maximum values of the strain ratio, defined as the ratio of the required actuation strain (ϵ^i) to the nominal strain (ϵ_∞) were obtained as 1.55 and 2.80, respectively, for the $(0_2^\circ/\pm 45^\circ/0_2^\circ)_s$ laminate. For the $(\pm 45^\circ/0_2^\circ/\pm 45^\circ/0_2^\circ)_s$ laminate, the corresponding strain ratios are 1.26 and 3.86. However, due to limits imposed by the present technology on the available actuation strains, we may not be able to generate such large actuation strains. To account for such technology limits, we investigated the effect of available actuation strain limits on the reduction in SCF. Figure 2.31 and Figure 2.32 illustrate the variation of SCF with available actuation strains for the axisymmetric and

44-variable non-axisymmetric cases, respectively. For the axisymmetric case, we can see that this variation is almost linear. Availability of actuation strains beyond $1.55\epsilon_\infty$ for the $(0_2^\circ/\pm 45^\circ/0_2^\circ)_s$ laminate and $1.26\epsilon_\infty$ for the $(\pm 45^\circ/0_2^\circ/\pm 45^\circ/0_2^\circ)_s$ laminate does not improve the SCF. For the non-axisymmetric case, a limit of 2.1 on the available strain ratio has little effect on the SCF for the $(0_2^\circ/\pm 45^\circ/0_2^\circ)_s$ laminate, which is reduced to 1.69, compared to 1.64, obtained with no limits on the magnitude of the actuation strains. Similarly, limiting the available strain ratio to 1.8, the SCF for the $(\pm 45^\circ/0_2^\circ/\pm 45^\circ/0_2^\circ)_s$ laminate can be reduced to 1.48, very close to the value of 1.46 obtained without limits. More stringent limits on the available strain ratio, however, have more serious consequences. For example, for a limit of 1.0 on the strain ratio, we get SCFs of 2.1 and 1.7 for $(0_2^\circ/\pm 45^\circ/0_2^\circ)_s$ and $(\pm 45^\circ/0_2^\circ/\pm 45^\circ/0_2^\circ)_s$ laminates, respectively.

2.3.5.3 Effects of Limits on Available Actuation Area

We also studied the effect of reducing the area over which the actuation strains are applied. Actuation strains were applied to groups of rings, starting from the first three rings (corresponding to area $r \leq 1.062A$, where A is the radius of the hole) to all eleven rings (corresponding to area $r \leq 1.5A$). Figure 2.33 illustrates the variation of SCF with the available area for the axisymmetric case. For both laminates, as we increase the area over which actuation strains are applied, the rate of change in SCF drops steadily. For the axisymmetric case, Figure 2.34 and Figure 2.35 show the variation of SCF for the $(0_2^\circ/\pm 45^\circ/0_2^\circ)_s$ laminate and $(\pm 45^\circ/0_2^\circ/\pm 45^\circ/0_2^\circ)_s$ laminate, respectively, with applied axisymmetric actuation strains for three cases where actuation strains were applied over areas $r \leq 1.062A, r \leq 1.206A$, and $r \leq 1.5A$. We can see that when the area over which the actuation strains were applied was increased, we could achieve greater reduction of SCF but at an ever increasing cost in terms of actuation strains.

Figure 2.36 shows the variation of SCF with the available area for the 44-variable non-axisymmetric case. For both laminates, the SCF varies almost linearly when actuation strains are applied over the area $r \leq 1.206A$. After that, the rate of change drops substantially. By applying actuation strains over $r \leq 1.206A$, the SCF of the $(0_2^\circ/\pm 45^\circ/0_2^\circ)_s$ laminate can be reduced from 4.47 to 1.74, compared to 1.64, which corresponds to an available area of $r \leq 1.5A$. For the $(\pm 45^\circ/0_2^\circ/\pm 45^\circ/0_2^\circ)_s$ laminate, the corresponding values of SCF are 1.6 and 1.46. Figure 2.37 and Figure 2.38 show the variation of SCF with applied actuation strains for the two laminates for the same areas. The results indicate that for a given limit of available actuation strain, the SCF can be reduced further by using more area. For example, for the $(0_2^\circ/\pm 45^\circ/0_2^\circ)_s$ laminate, a limit of $\epsilon^i/\epsilon_\infty = 1$ leads to SCF values of 2.83, 2.43, and 2.10 corresponding to the three radii. Similarly, from Figure 2.38, a limit of 1 on the available strain ratio gives SCF values of 2.41, 1.97, and 1.70 corresponding to the three radii for the $(\pm 45^\circ/0_2^\circ/\pm 45^\circ/0_2^\circ)_s$ laminate.

2.4 Summary

With axisymmetric actuation strain distributions, the stress concentration factor for an isotropic plate with a hole was reduced for 3 to 2. Actuation strains were required in a ring around the hole with $r \leq 1.21A$ and $r \leq 1.25A$ for Von-Mises stress and maximum shear stress criteria, respectively. When actuation strains were applied only in the tangential direction, the same reduction were achieved with a higher actuation strain magnitudes. Non-axisymmetric actuation strains were applied to an area with outer diameter 1.5 times the diameter of the hole. With analytical optimization, the stress concentration factor for maximum shear stress and Von-Mises stress criteria were reduced to 1.45 and 1.58, respectively. With finite element based optimization, the stress

concentration facors for twenty-variable (4-sector) case were reduced to 1.62 and 1.65 for Von-Mises and maximum shear stress criteria, respectively, which are quite close to the results obtained from the analytical optimizations. In this case, high actuation strains, up to 3.66 S/E, were required in some cases. Constraints imposed on the magnitude of the applied actuation strains lead to only slightly higher maximum stresses.

Numerical optimizations based on finite element simulations were carried out for a composite plate with a hole. It was found that the stress concentration factors for a composite plate with a hole can be reduced substantially by applying actuation strains over an area with outer diameter 1.5 times the diameter of the hole. Two laminates with stacking sequences $(0_2^o/\pm 45^o/0_2^o)_s$ and $(\pm 45^o/0_2^o/\pm 45^o/0_2^o)_s$ were studied. With axisymmetric actuation strain distributions, the stress concentration factor was reduced from 4.47 to 2.45 for the $(0_2^o/\pm 45^o/0_2^o)_s$ laminate and 3.20 to 1.97 for the $(\pm 45^o/0_2^o/\pm 45^o/0_2^o)_s$ laminate. Non-axisymmetric actuation strain distributions reduced the stress concentation factor from 4.47 to 1.64 for the $(0_2^o/\pm 45^o/0_2^o)_s$ laminate and 3.20 to 1.46 for the $(\pm 45^o/0_2^o/\pm 45^o/0_2^o)_s$ laminate. We also studied the effect of reducing the area over which the actuation strains are applied. It was found that when the area over which the actuation strains were applied was increased, we could achieve greater reduction of SCF but at an ever increasing cost in terms of actuation strains. The results indicate that for a given limit of available actuation strain, the SCF can be reduced further by using more area. It was also found that the effects of limits on actuation strains depended on the area available for applying the actuation strains, with larger areas reducing the effects of the limits.

Table 2.1. Maximum stress concentration factors for axisymmetric, one sector and two sector isotropic cases (Reductions in SCFs are shown in parenthesis)

Criteria/Max. SCFs	Region of applied actuation strains		
	0^o - 90^o (axisymmetric)	0^o - 45^o and 45^o - 90^o	45^o - 90^o
Von-Mises criterion	1.97 (-34 %)	1.65 (-45 %)	1.68 (-44 %)
Max. shear criterion	1.98 (-34 %)	1.71 (-46 %)	1.78 (-45 %)

Table 2.2. Optimal actuation strain distributions for two sector isotropic case

Normalized actuation strains; $\epsilon^i_N = E\epsilon^i/S$	Regions	ϵ^i_{1N}	ϵ^i_{2N}	ϵ^i_{3N}	ϵ^i_{4N}	ϵ^i_{5N}
Von-Mises	45^o - 90^o	1.31	1.13	0.97	0.60	0.28
criterion	0^o - 45^o	-0.79	-1.02	-0.22	1.02	0.59
Max. shear	45^o - 90^o	1.21	1.05	0.92	0.58	0.27
criterion	0^o - 45^o	0.76	0.89	1.00	0.40	0.47

Table 2.3. Optimal unconstrained actuation strain distributions for four sector isotropic case

Normalized actuation strains; $\epsilon_N^i = E\epsilon^i/S$	Regions	ϵ_{1N}^i	ϵ_{2N}^i	ϵ_{3N}^i	ϵ_{4N}^i	ϵ_{5N}^i
Von-Mises	90^o - 67.5^o	0.91	0.75	0.63	0.40	0.20
criterion	67.5^o - 45^o	3.66	2.89	1.21	0.60	0.23
	45^o - 22.5^o	1.13	0.60	0.70	1.62	0.24
	22.5^o - 0^o	-1.77	-1.99	-1.66	0.54	1.13
Max. shear	90^o - 67.5^o	0.84	0.70	0.59	0.36	0.18
criterion	67.5^o - 45^o	3.06	2.85	1.26	0.57	0.22
	45^o - 22.5^o	1.69	1.85	2.12	1.03	0.12
	22.5^o - 0^o	-1.20	-1.00	-0.48	0.33	1.28

Table 2.4. Maximum reduction in stress concentration factors when actuation strains are applied to four sectors : (1) $\epsilon_N^i \geq 0$, (2) $-1.38 \leq \epsilon_N^i \leq 1.38$, (3) $0 \leq \epsilon_N^i \leq 1.38$, (4) $0 \leq \epsilon_N^i \leq 1.00$, (5) unconstrained ϵ_N^i (Isotropic case, Reduction in SCFs are given in parenthesis)

Max. SCFs	Case				
	(1)	(2)	(3)	(4)	(5)
Von-Mises	1.62	1.65	1.65	1.72	1.62
criterion	(-46 %)	(-45 %)	(-45 %)	(-43 %)	(-46 %)
Max. shear	1.65	1.67	1.68	1.71	1.65
criterion	(-45 %)	(-44 %)	(-44 %)	(-43 %)	(-45 %)

Table 2.5. Constrained optimal actuation strain distributions for four sector isotropic case : $\epsilon^i_N \geq 0$

Normalized actuation strains; $\epsilon^i_N = E\epsilon^i/S$	Regions	ϵ^i_{1N}	ϵ^i_{2N}	ϵ^i_{3N}	ϵ^i_{4N}	ϵ^i_{5N}
Von-Mises	90^o - 67.5^o	1.05	0.88	0.75	0.47	0.23
criterion	67.5^o - 45^o	2.92	3.08	1.22	0.55	0.18
	45^o - 22.5^o	0.37	0.37	0.01	0.00	0.36
	22.5^o - 0^o	0.00	0.00	0.00	1.27	1.63
Max. shear	90^o - 67.5^o	0.87	0.72	0.61	0.38	0.19
criterion	67.5^o - 45^o	3.30	2.84	1.22	0.56	0.21
	45^o - 22.5^o	1.36	1.58	2.00	0.74	0.08
	22.5^o - 0^o	0.00	0.00	0.00	0.00	1.37

Table 2.6. Constrained optimal actuation strain distributions for four sector isotropic case : $-1.38 \leq \epsilon^i_N \leq 1.38$

Normalized actuation strains; $\epsilon^i_N = E\epsilon^i/S$	Regions	ϵ^i_{1N}	ϵ^i_{2N}	ϵ^i_{3N}	ϵ^i_{4N}	ϵ^i_{5N}
Von-Mises	90^o - 67.5^o	1.08	0.91	0.77	0.46	0.21
criterion	67.5^o - 45^o	1.38	1.38	1.38	0.45	0.19
	45^o - 22.5^o	0.60	1.25	1.35	1.38	0.45
	22.5^o - 0^o	-1.38	-1.38	-1.38	0.69	1.23
Max. shear	90^o - 67.5^o	0.99	0.84	0.74	0.46	0.22
criterion	67.5^o - 45^o	1.38	1.38	1.38	0.70	0.20
	45^o - 22.5^o	1.38	1.38	1.38	1.38	0.24
	22.5^o - 0^o	-1.38	-1.38	-1.07	0.77	-1.29

Table 2.7. Constrained optimal actuation strain distributions for four sector isotropic case : $0 \leq \epsilon_N^i \leq 1.38$

Normalized actuation strains; $\epsilon_N^i = E\epsilon^i/S$	Regions	ϵ_{1N}^i	ϵ_{2N}^i	ϵ_{3N}^i	ϵ_{4N}^i	ϵ_{5N}^i
Von-Mises	90^o - 67.5^o	1.14	0.97	0.82	0.50	0.22
criterion	67.5^o - 45^o	1.38	1.38	1.38	0.43	0.16
	45^o - 22.5^o	0.00	0.00	0.88	1.38	0.22
	22.5^o - 0^o	0.00	0.00	0.00	0.45	1.38
Max. shear	90^o - 67.5^o	1.38	0.89	0.69	0.38	0.11
criterion	67.5^o - 45^o	1.05	1.38	1.38	0.58	0.15
	45^o - 22.5^o	0.00	1.38	1.38	1.38	0.10
	22.5^o - 0^o	1.38	0.00	0.00	0.00	1.38

Table 2.8. Constrained optimal actuation strain distributions for four sector isotropic case : $0 \leq \epsilon_N^i \leq 1.00$

Normalized actuation strains; $\epsilon_N^i = E\epsilon^i/S$	Regions	ϵ_{1N}^i	ϵ_{2N}^i	ϵ_{3N}^i	ϵ_{4N}^i	ϵ_{5N}^i
Von-Mises	90^o - 67.5^o	1.00	0.84	0.69	0.38	0.11
criterion	67.5^o - 45^o	1.00	1.00	1.00	0.75	0.24
	45^o - 22.5^o	1.00	1.00	0.00	1.00	0.79
	22.5^o - 0^o	0.00	0.00	0.00	0.00	1.00
Max. shear	90^o - 67.5^o	1.00	0.85	0.75	0.46	0.19
criterion	67.5^o - 45^o	1.00	1.00	1.00	1.00	0.28
	45^o - 22.5^o	1.00	1.00	1.00	1.00	0.59
	22.5^o - 0^o	0.00	0.00	0.00	0.00	0.54

Table 2.9. Comparison of stress concentration factors for composite plate

Laminate	EAL model	Hong & Crews [59]
$0°$	5.95	6.04
$(0°/90°)_s$	4.57	4.54
$(0°/\pm 45°/90°)_s$	2.89	2.85

Table 2.10. Safety factors (R) and stress concentration factors (SCF) for stacking sequence $(0_2^\circ/\pm 45°/0_2^\circ)_s$ (original R = 2.19 and SCF = 4.47)

	Axisymmetric Case	Non-axisymmetric Case	
		22 Strain Variables	44 Strain Variables
R	4.00	5.61	5.96
SCF	2.45	1.75	1.64

Table 2.11. Safety factors (R) and stress concentration factors (SCF) for laminate $(\pm 45°/0_2^\circ/\pm 45°/0_2^\circ)_s$ (Original R = 2.93 AND SCF = 3.20)

	Axisymmetric Case	Non-axisymmetric Case	
		22 Strain Variables	44 Strain Variables
R	4.76	6.26	6.44
SCF	1.97	1.50	1.46

Table 2.12. Optimal actuation strain distributions in eleven rings for four sectors for stacking sequence $(0_2^\circ/\pm 45°/0_2^\circ)_s$

Normalized actuation strains; $\epsilon_N^i = \epsilon^i/(S/E)$	Regions			
	90° - 67.5°	67.5° - 45°	45° - 22.5°	22.5° - 0°
ϵ_{1N}^i	2.71	1.46	-0.16	-2.80
ϵ_{2N}^i	2.36	1.43	-0.49	-2.80
ϵ_{3N}^i	2.00	1.19	-0.69	-2.71
ϵ_{4N}^i	1.64	1.02	-0.57	-2.15
ϵ_{5N}^i	1.26	0.79	-0.77	-2.41
ϵ_{6N}^i	0.88	0.54	-0.40	-1.89
ϵ_{7N}^i	0.42	0.26	1.18	-1.30
ϵ_{8N}^i	0.54	0.00	-0.43	-1.87
ϵ_{9N}^i	0.38	0.26	0.24	-0.79
ϵ_{10N}^i	0.54	0.65	-0.25	0.17
ϵ_{11N}^i	0.47	1.11	0.61	0.29

Table 2.13. Optimal actuation strain distributions in eleven rings for two sectors for stacking sequence $(0_2^o/\pm 45^o/0_2^o)_s$

Normalized actuation strains; $\epsilon_N^i = \epsilon^i$ /(S/E)	Regions	
	90^o - 45^o	45^o - 0^o
ϵ_{1N}^i	2.46	-1.98
ϵ_{2N}^i	2.11	-1.46
ϵ_{3N}^i	1.76	-1.13
ϵ_{4N}^i	1.47	-0.88
ϵ_{5N}^i	1.18	-0.74
ϵ_{6N}^i	0.86	-0.61
ϵ_{7N}^i	0.51	-0.68
ϵ_{8N}^i	0.15	-0.49
ϵ_{9N}^i	-1.44	-0.96
ϵ_{10N}^i	-0.34	-0.22
ϵ_{11N}^i	0.49	-1.09

Table 2.14. Optimal actuation strain distributions in eleven rings for four sectors for stacking sequence $(\pm 45^o/0_2^o/\pm 45^o/0_2^o)_s$

Normalized actuation strains; $\epsilon_N^i = \epsilon^i$ /(S/E)	Regions			
	90^o - 67.5^o	67.5^o - 45^o	45^o - 22.5^o	22.5^o - 0^o
ϵ_{1N}^i	1.89	3.86	0.17	-3.75
ϵ_{2N}^i	1.71	3.34	-0.36	-3.47
ϵ_{3N}^i	1.53	2.71	-0.53	-3.49
ϵ_{4N}^i	1.34	1.64	-0.64	-3.25
ϵ_{5N}^i	1.16	1.26	-0.66	-3.08
ϵ_{6N}^i	0.99	1.38	-0.67	-3.34
ϵ_{7N}^i	0.81	1.43	0.04	-2.45
ϵ_{8N}^i	0.59	0.38	1.19	-2.17
ϵ_{9N}^i	0.36	0.24	1.04	-1.85
ϵ_{10N}^i	0.10	-0.13	-0.42	-0.94
ϵ_{11N}^i	1.23	0.88	0.90	0.84

Table 2.15. Optimal actuation strain distributions in eleven rings for two sectors for stacking sequence $(\pm 45^o/0_2^o/\pm 45^o/0_2^o)_s$

Normalized actuation strains; $\epsilon_N^i = \epsilon^i$ /(S/E)	Regions	
	90^o - 45^o	45^o - 0^o
ϵ_{1N}^i	2.04	-2.73
ϵ_{2N}^i	1.85	-1.03
ϵ_{3N}^i	1.65	-1.46
ϵ_{4N}^i	1.43	-1.33
ϵ_{5N}^i	1.19	-1.42
ϵ_{6N}^i	0.94	-1.59
ϵ_{7N}^i	0.67	0.19
ϵ_{8N}^i	0.38	0.69
ϵ_{9N}^i	0.09	0.18
ϵ_{10N}^i	-0.21	-1.03
ϵ_{11N}^i	0.78	-1.15

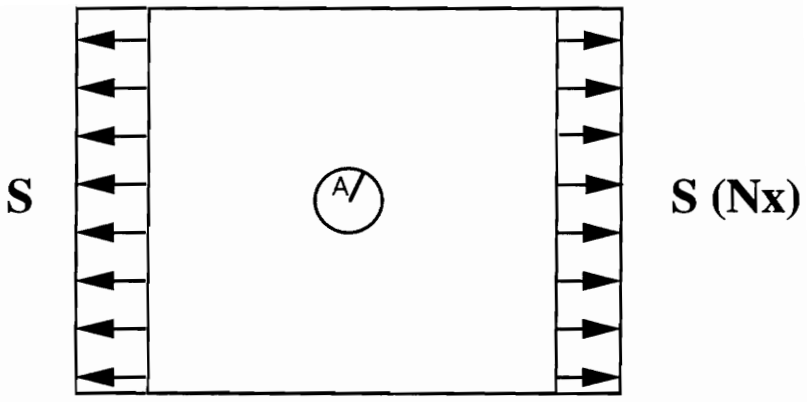

Figure 2.1: Plate with a hole under uniaxial tension

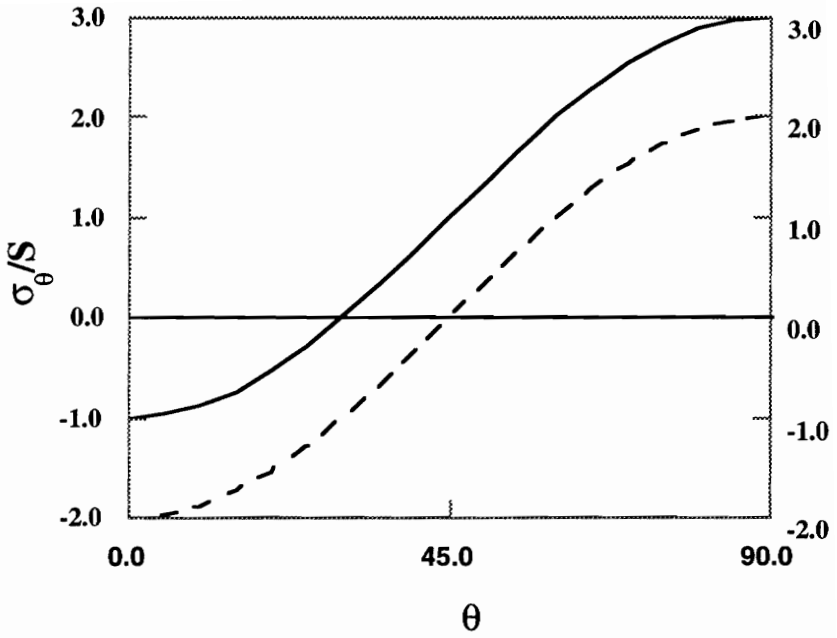

Figure 2.2 : Variation of stress concentration factor for axisymmetric case at r = A

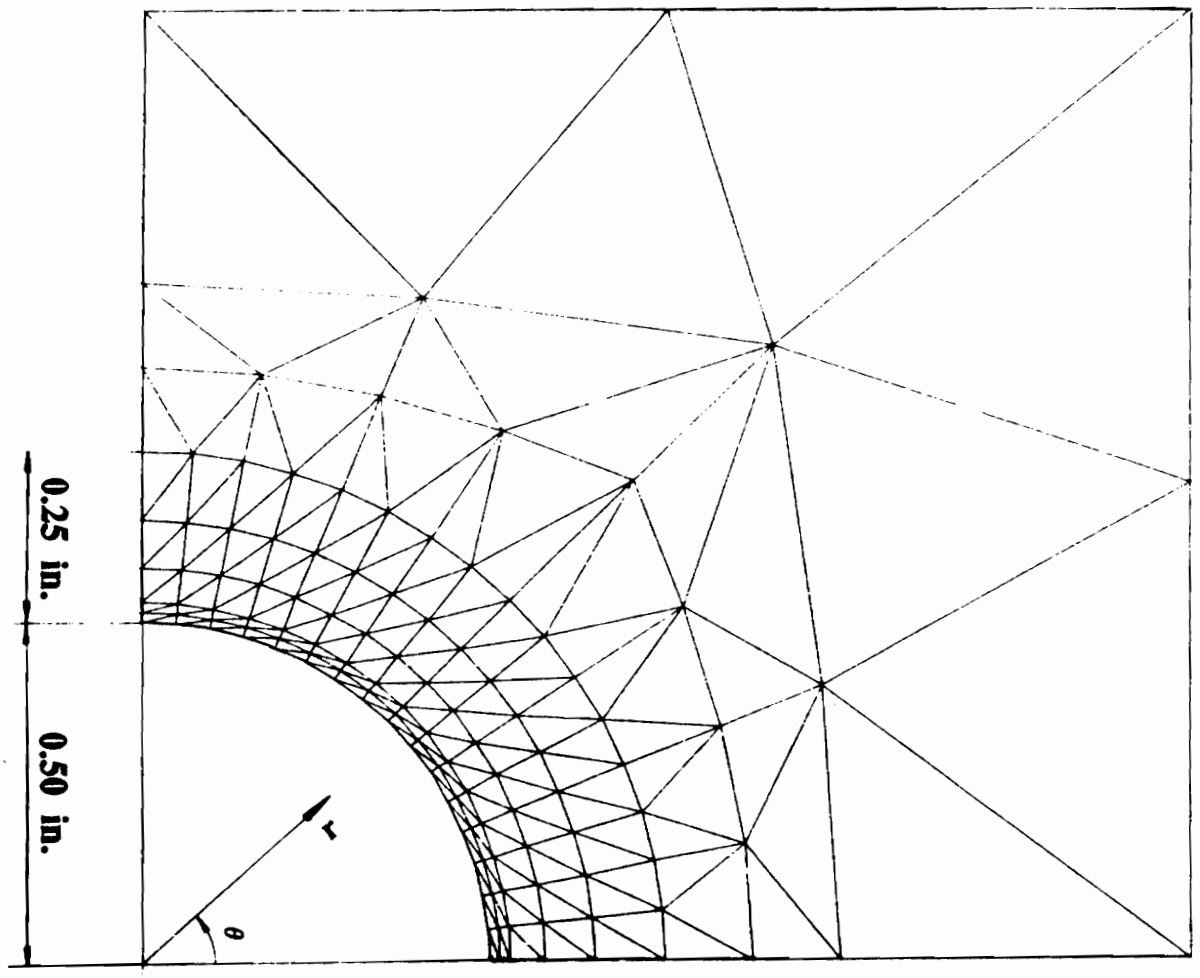

Figure 2.3 : Finite element mesh in the vicinity of the hole for isotropic plate

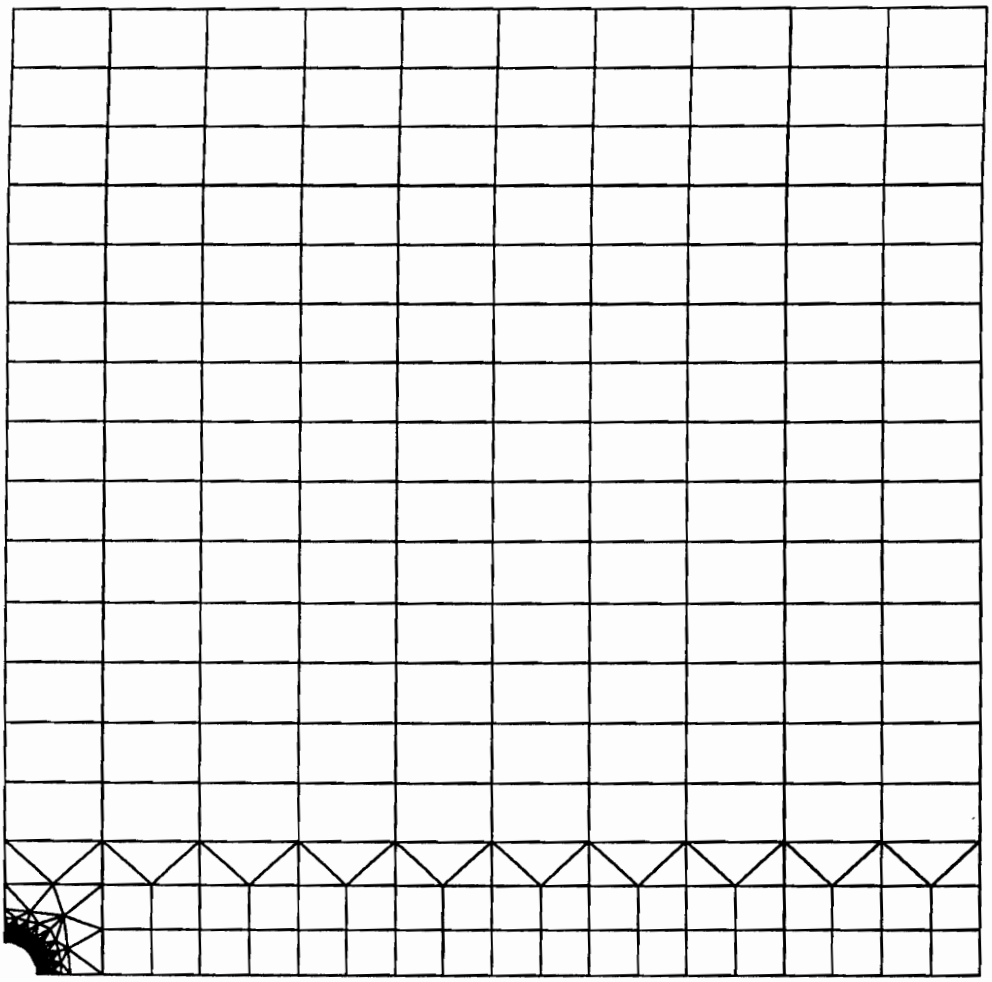

Figure 2.4 : Finite element mesh of the quarter plate model for isotropic plate

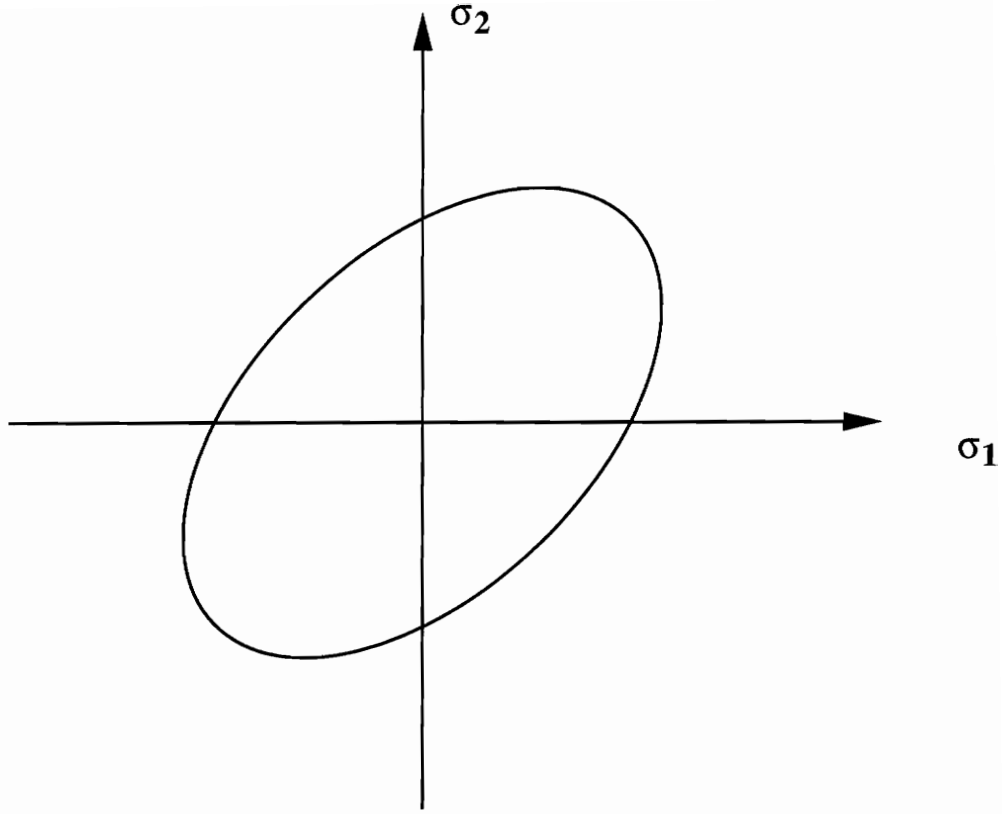

Figure 2.5 : Von-Mises stress criterion

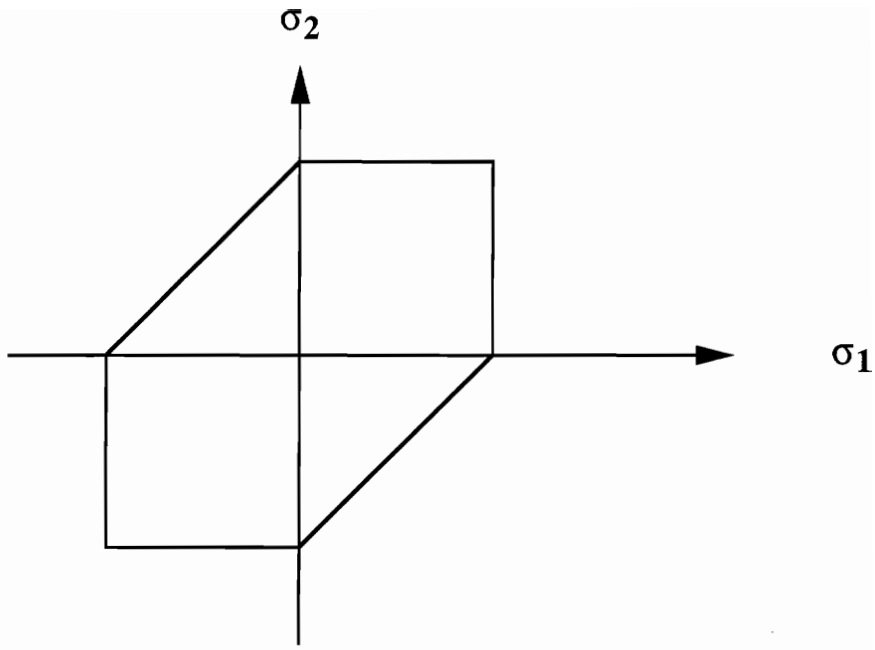

Figure 2.6 : Maximum shear stress criterion

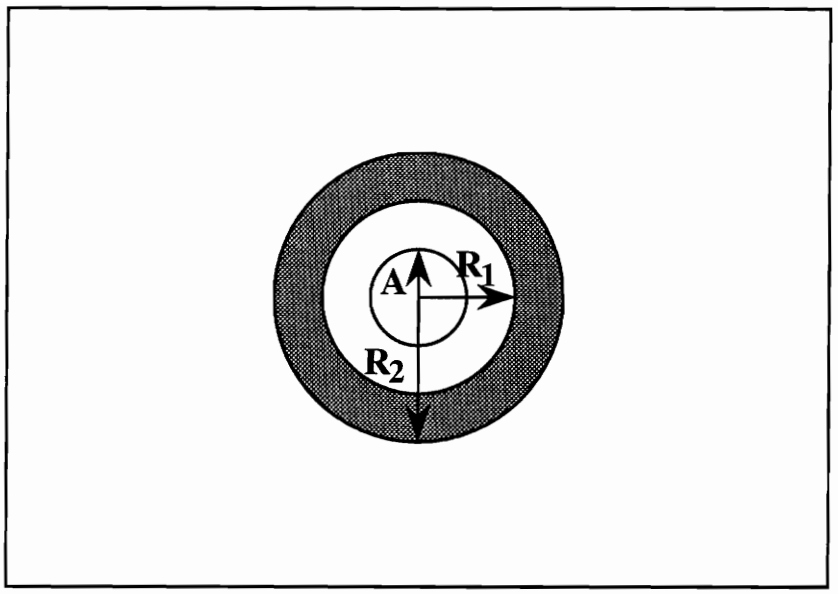

Figure 2.7 : Plate with a hole with three regions, actuation strains applied over R1 < r < R2

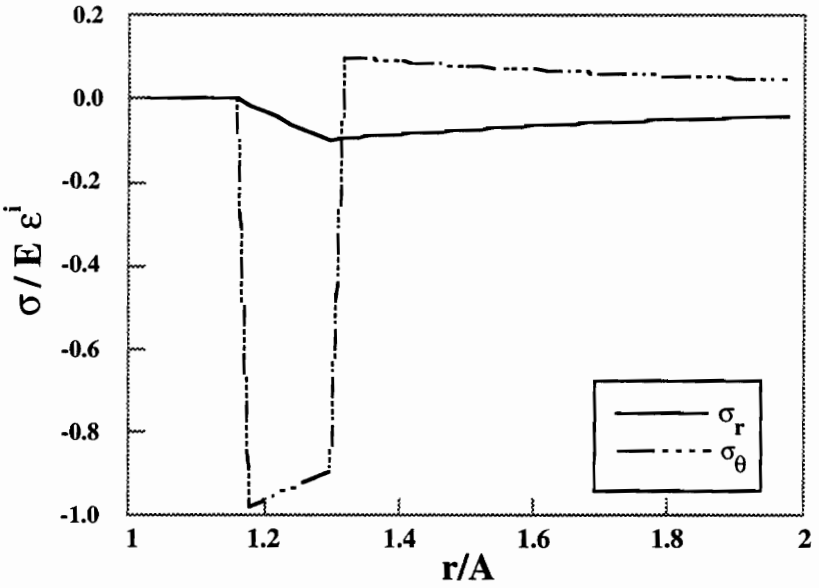

Figure 2.8 : Radial and tangential stresses due to isotropic axisymmetric actuation strains ($\varepsilon_r^{\,i} = \varepsilon_\theta^{\,i}$) applied over the region $1.16 < r/A < 1.3$

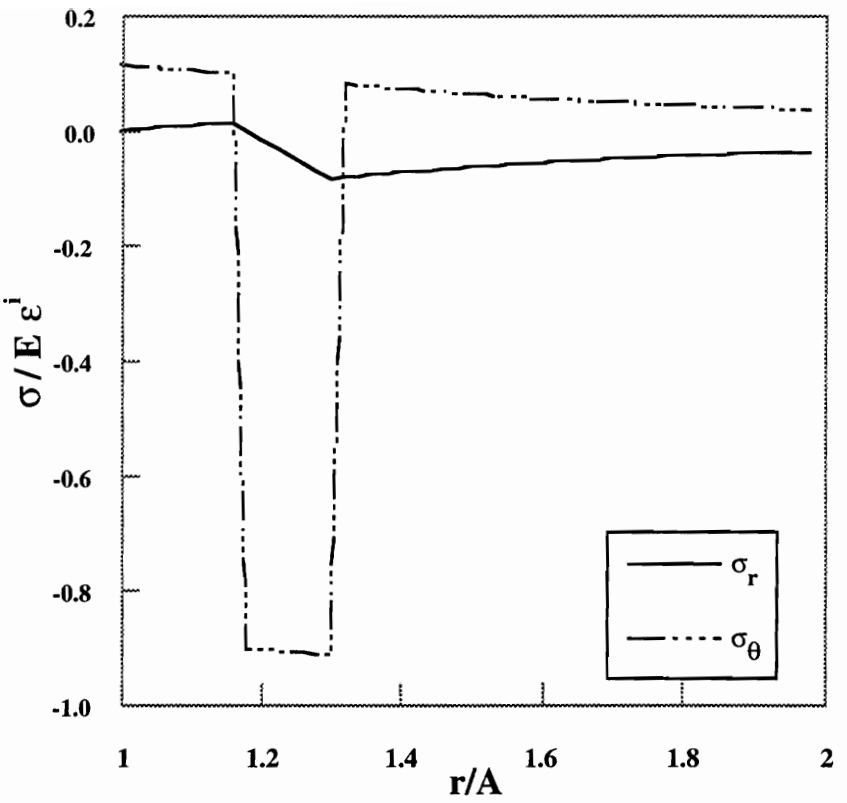

Figure 2.9 : Radial and tangential stresses due to tangential axisymmetric actuation strains ($\varepsilon_r^i = 0$) applied over the region $1.16 < r/A < 1.3$

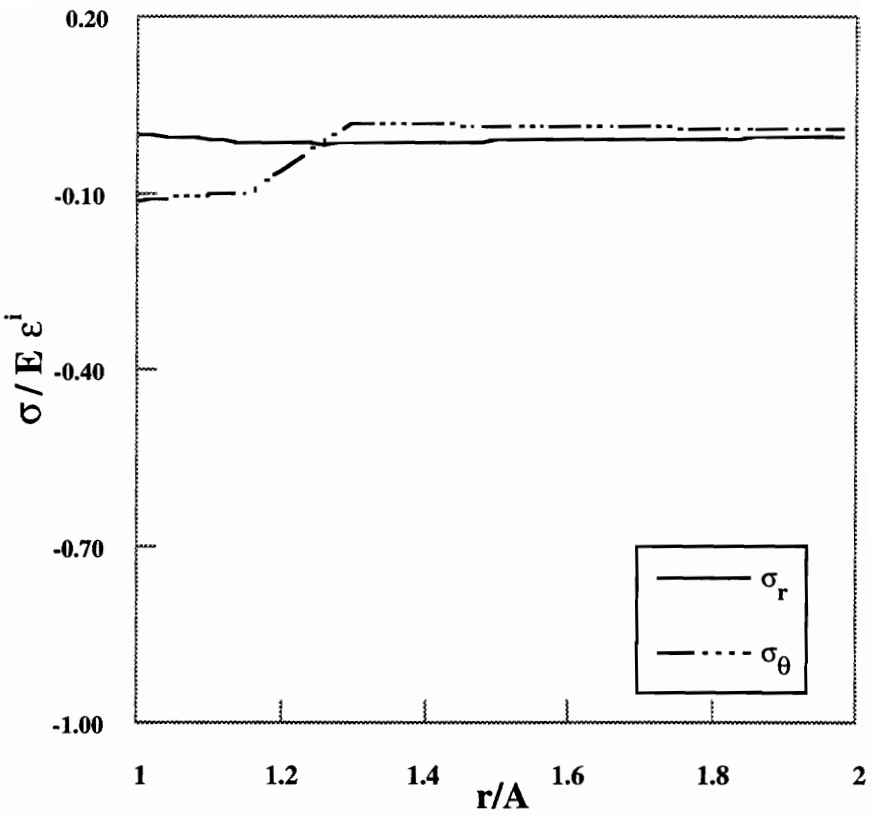

Figure 2.10 : Radial and tangential stresses due to radial axisymmetric actuation strains ($\varepsilon_\theta^{\,i} = 0$) applied over the region $1.16 < r/A < 1.3$

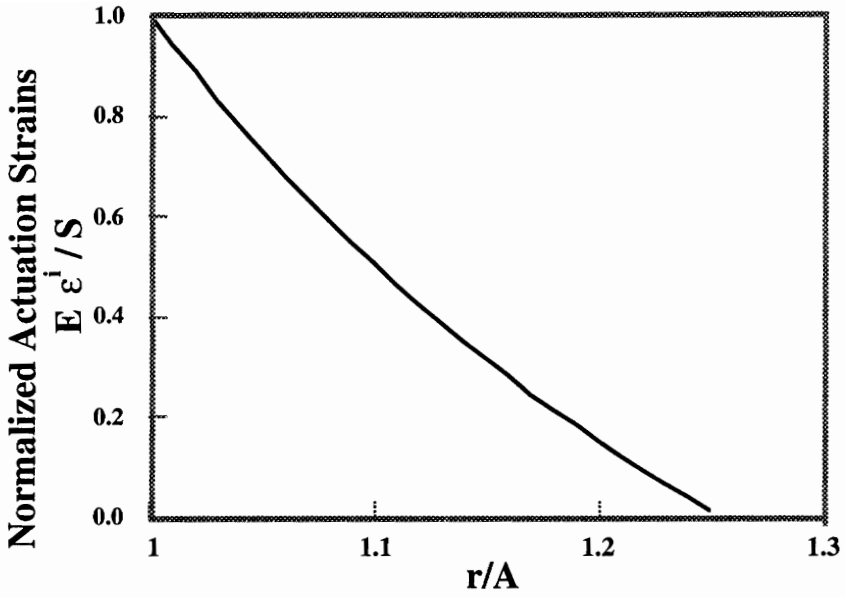

Figure 2.11 : Optimal axisymmetric actuation strain distribution to minimize tangential stresses at $\theta = 90^{o}$

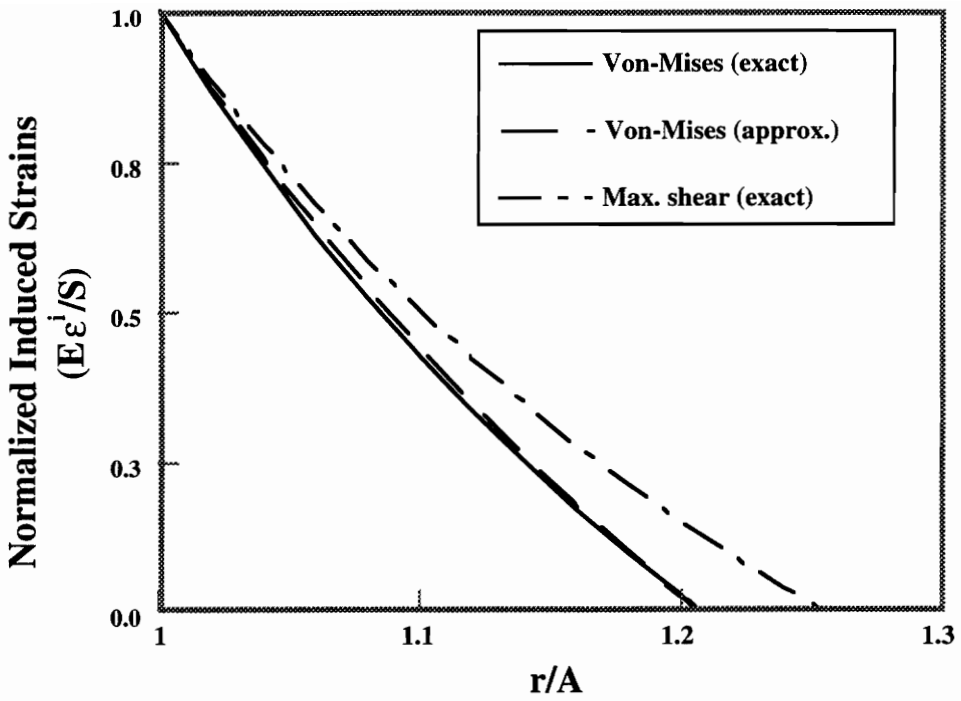

Figure 2.12 : Comparison of exact and approximate actuation strain distribution for Von-Mises stress criterion and exact solution for max. shear criterion (Analytical solutions)

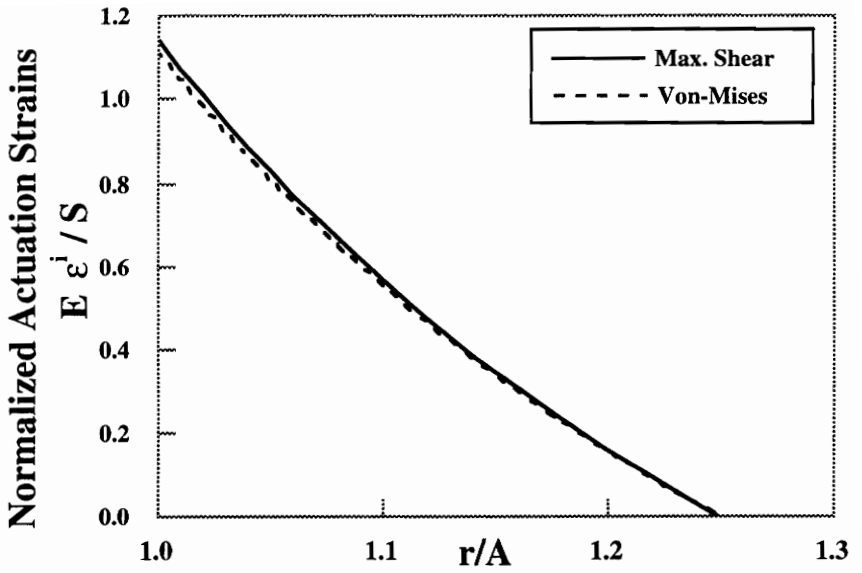

Figure 2.13 : Optimal axisymmetric actuation strain distributions (Analytical solutions, $\varepsilon_r^i = 0$)

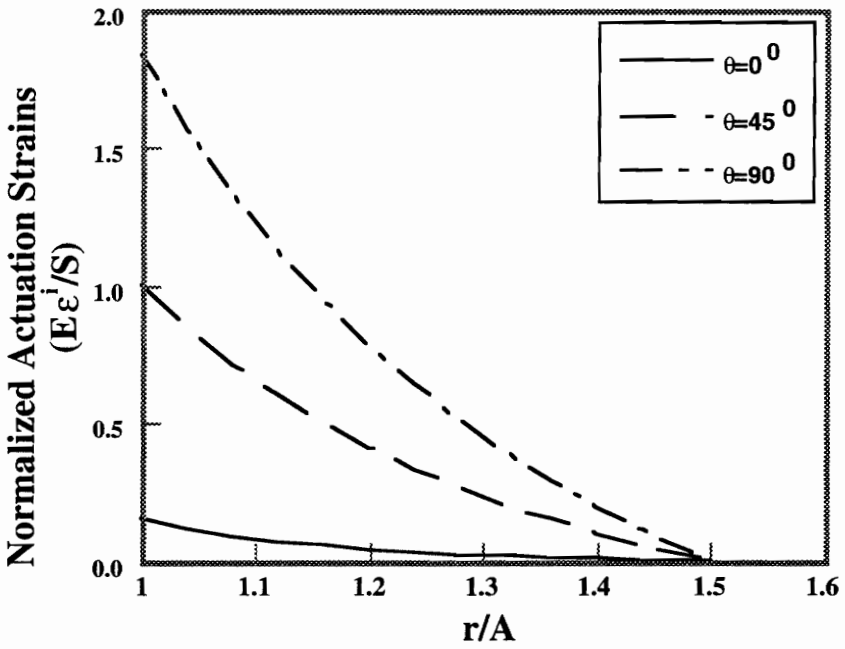

Figure 2.14 : Optimal non-axisymmetric actuation strain distributions for maximum shear stress criterion (Analytical solutions)

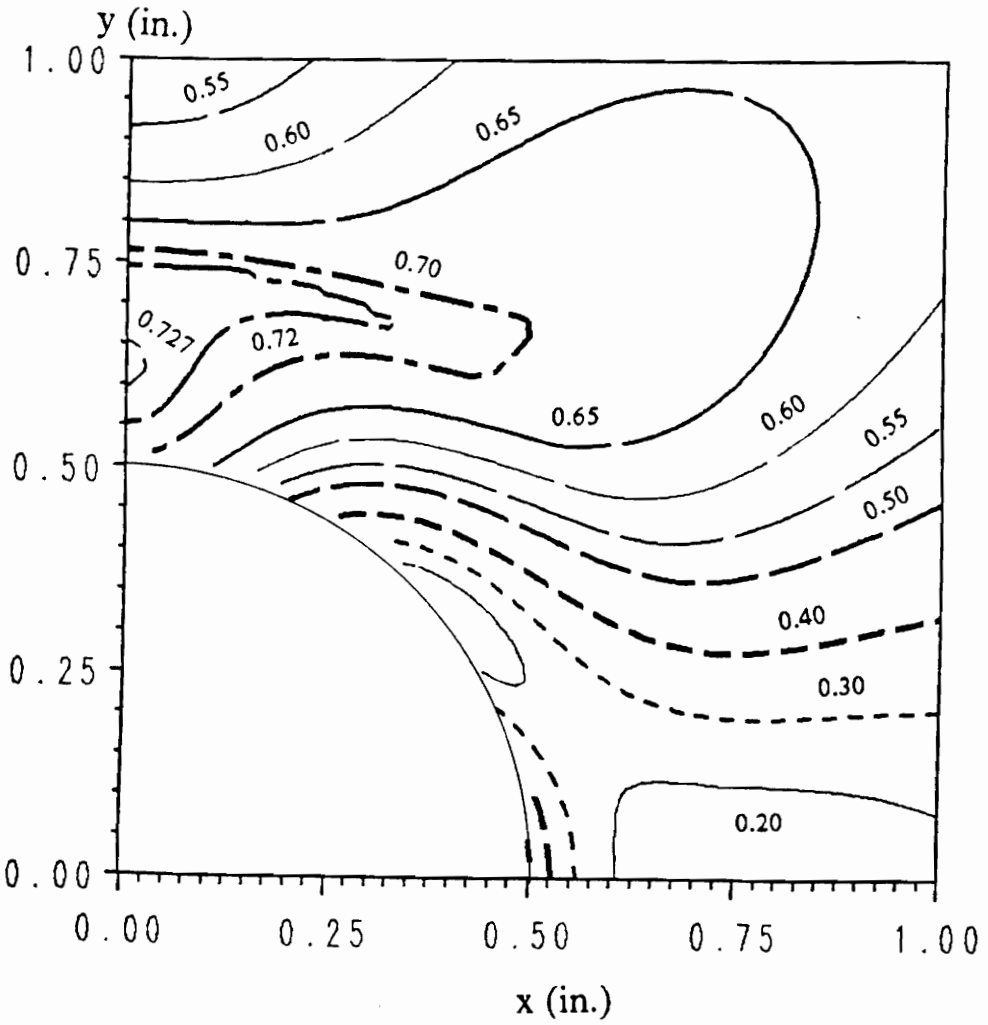

Figure 2.15 : Normalized maximum shear equivalent stress (σ_{MS}/S) contours for optimal analytical non-axisymmetric actuation strain dstribution

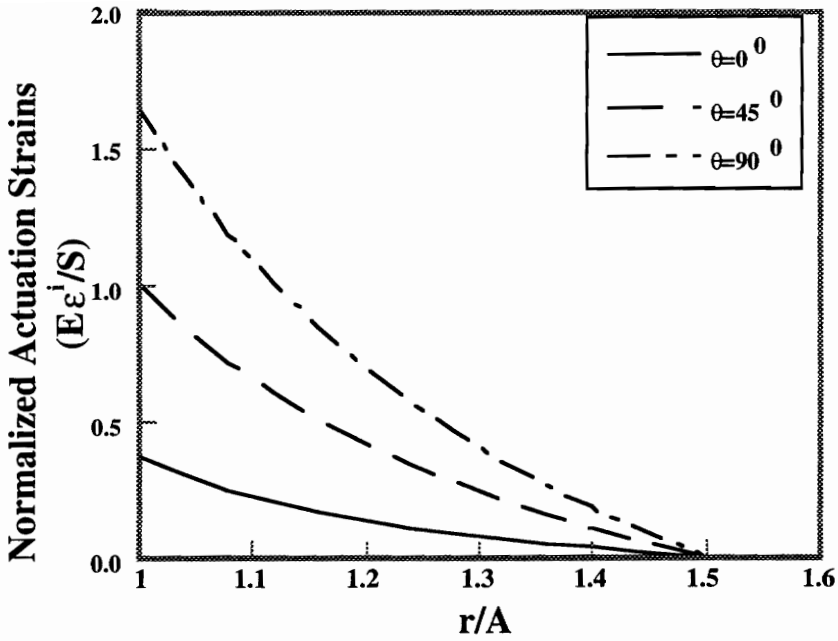

Figure 2.16 : Optimal non-axisymmetric actuaton strain distributions for Von-Mises stress criterion (Analytical solutions)

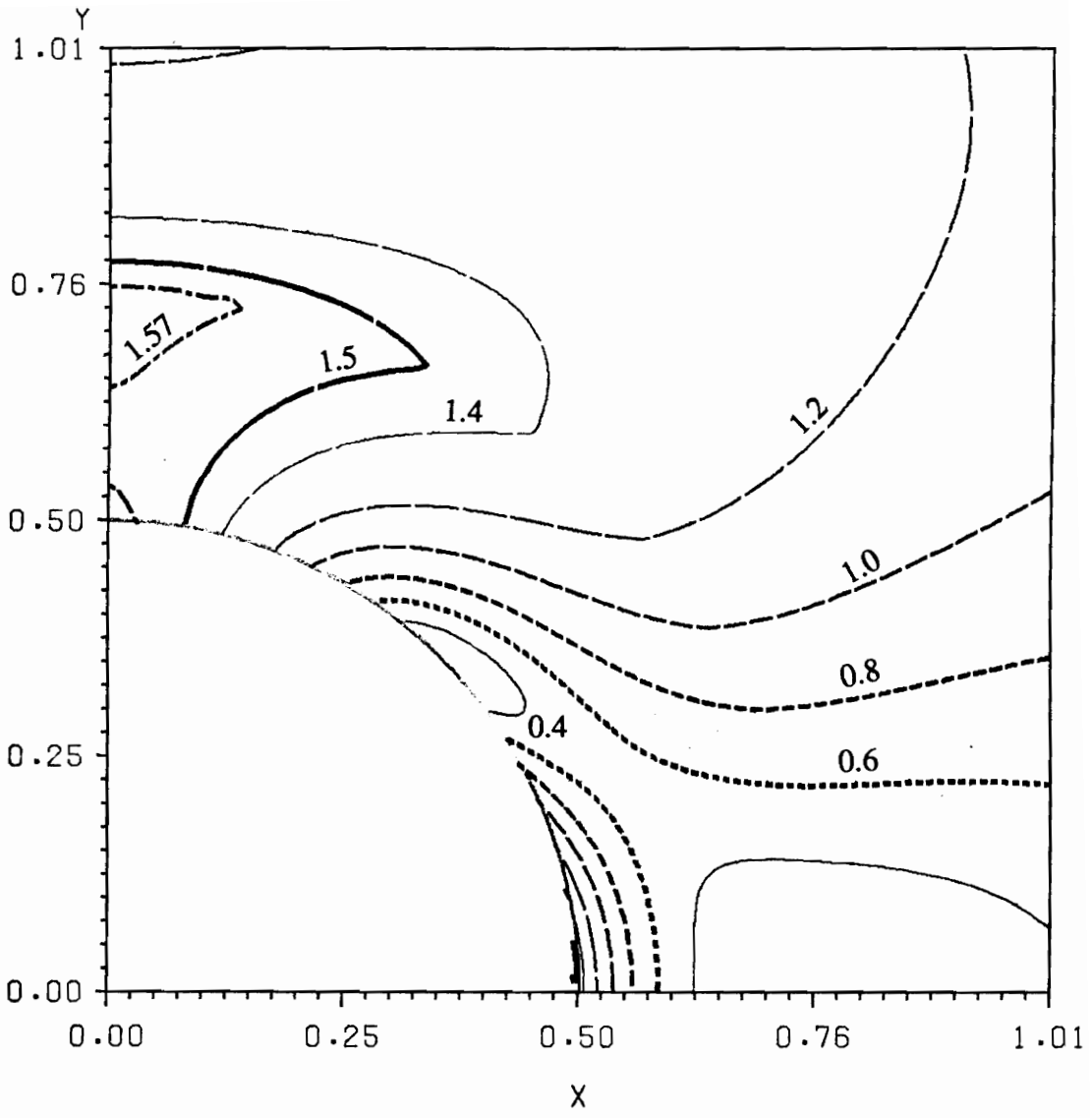

Figure 2.17 : Normalized Von-Mises equivalent stress (σ_V/S) contours for optimal analytical non-axisymmetric actuation strain dstribution

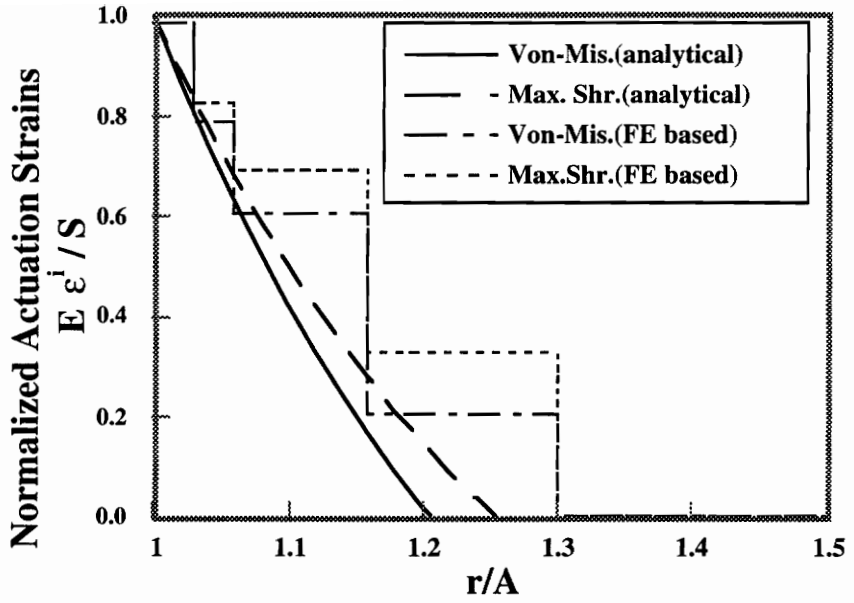

Figure 2.18 : Comparison of analytical and finite element based optimal actuation strain distributions (Axisymmetric case)

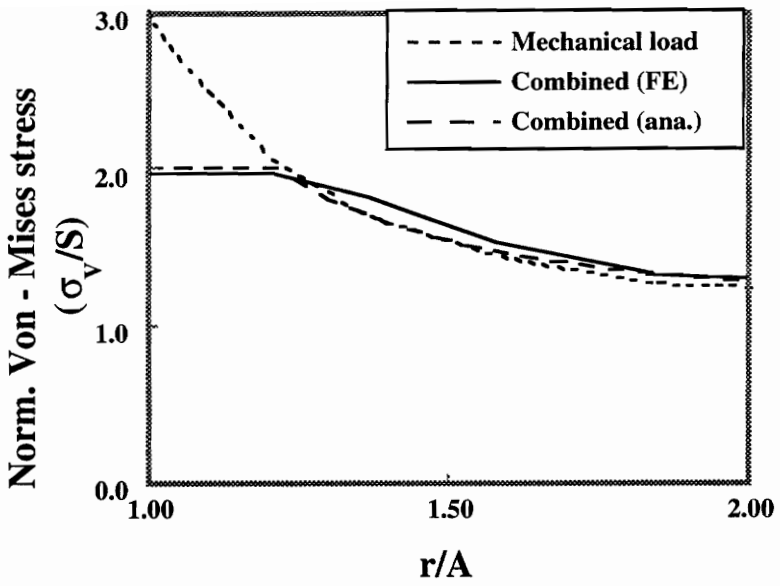

Figure 2.19 : Yield stress distribution for Von-Mises stress criterion at $\theta=90^0$ (axisymmetric optimum)

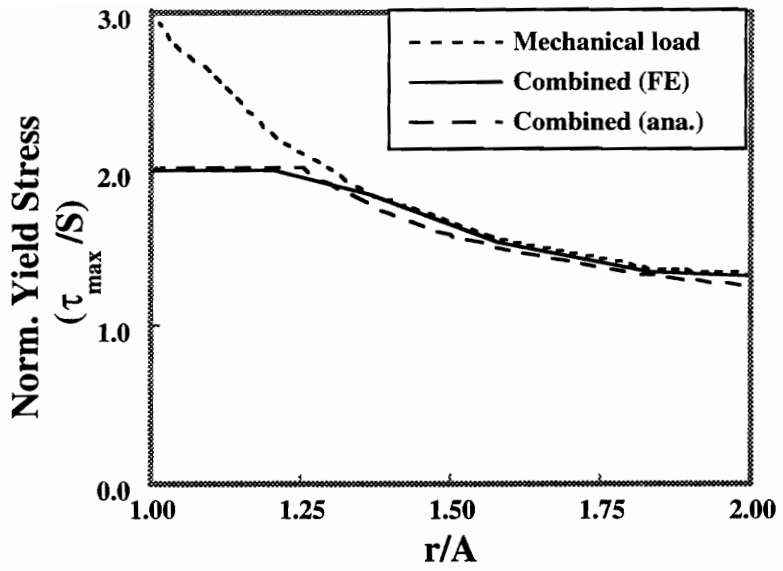

Figure 2.20 : Yield stress distribution for maximum shear stress criterion at $\theta=90^0$(axisymmetric optimum)

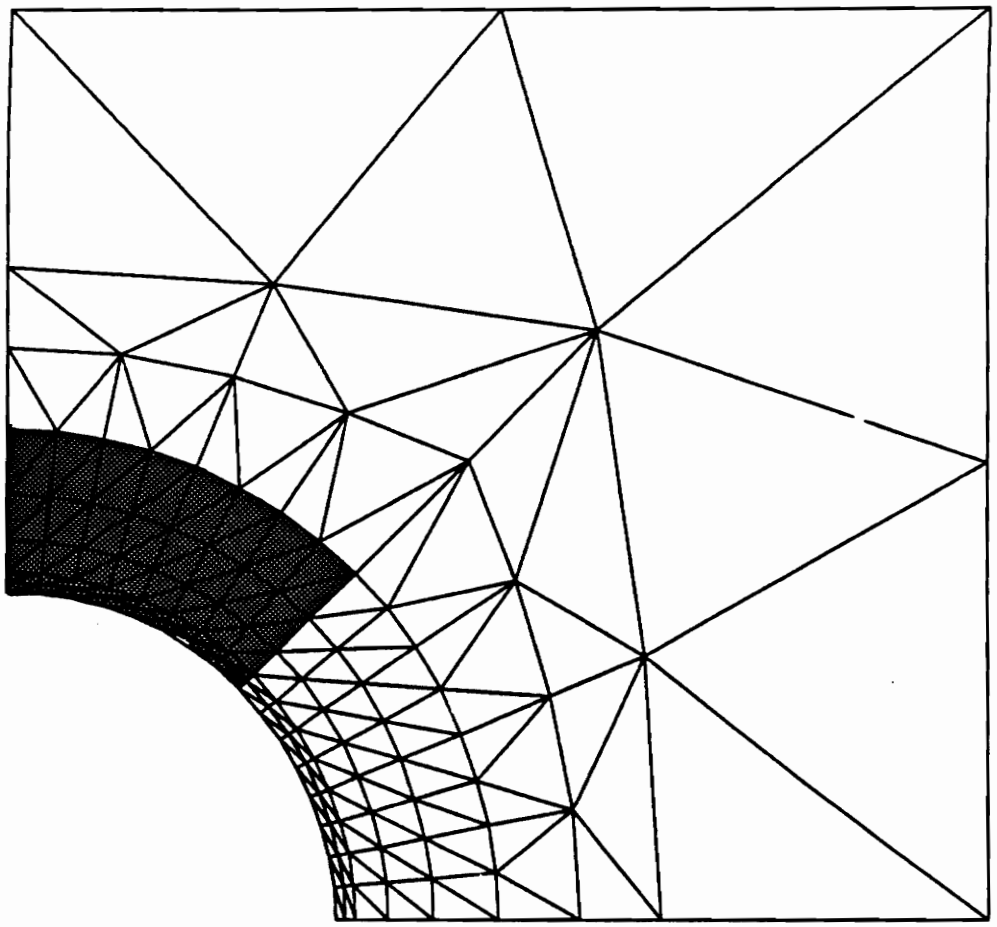

Figure 2.21 : Finite element mesh showing region of applied actuation strain for five-variable case, actuation strain applied over $45^{o} < \theta < 90^{o}$

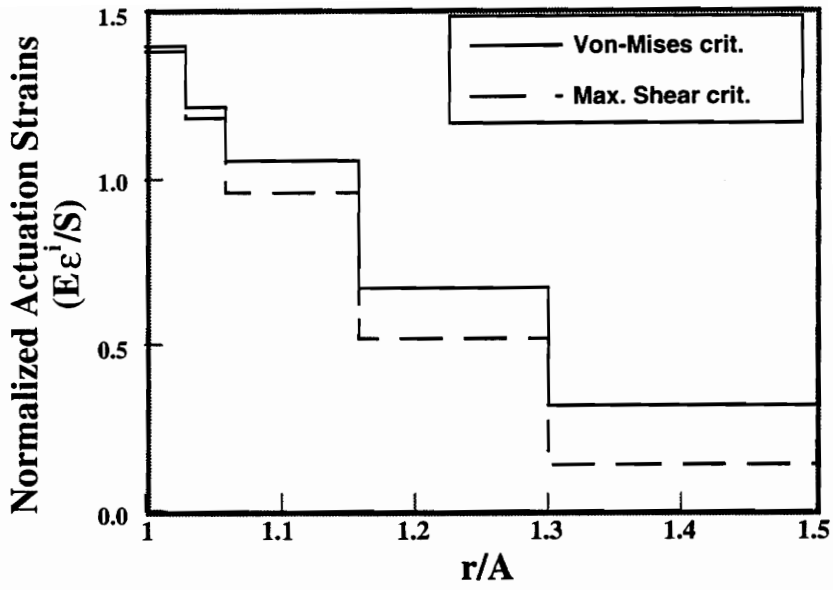

Figure 2.22 : Optimal actuation strain distributions strains applied over $45^0 < \theta < 90^0$, (FE based solution)

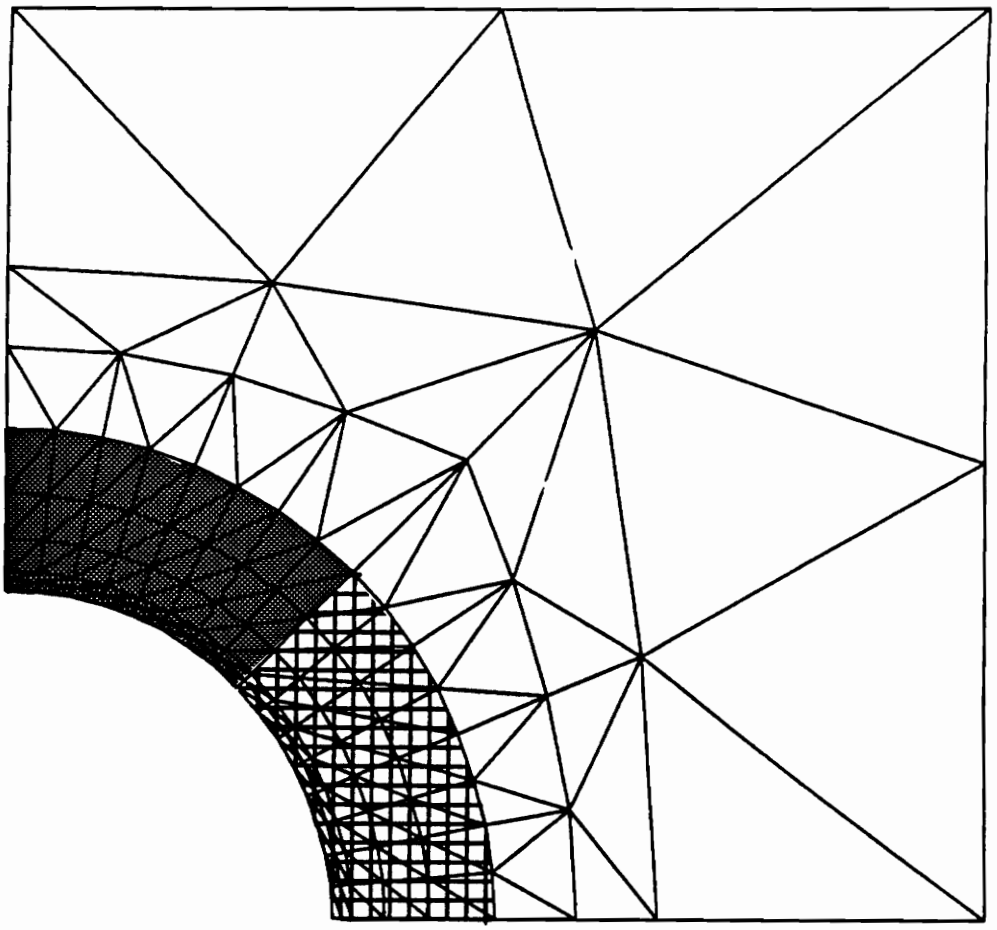

Figure 2.23 : Finite element mesh showing region of applied actuation strain for ten-variable (2-sector) case, actuation strain applied over $45^{o} < \theta < 90^{o}$ and $0 < \theta < 45^{o}$

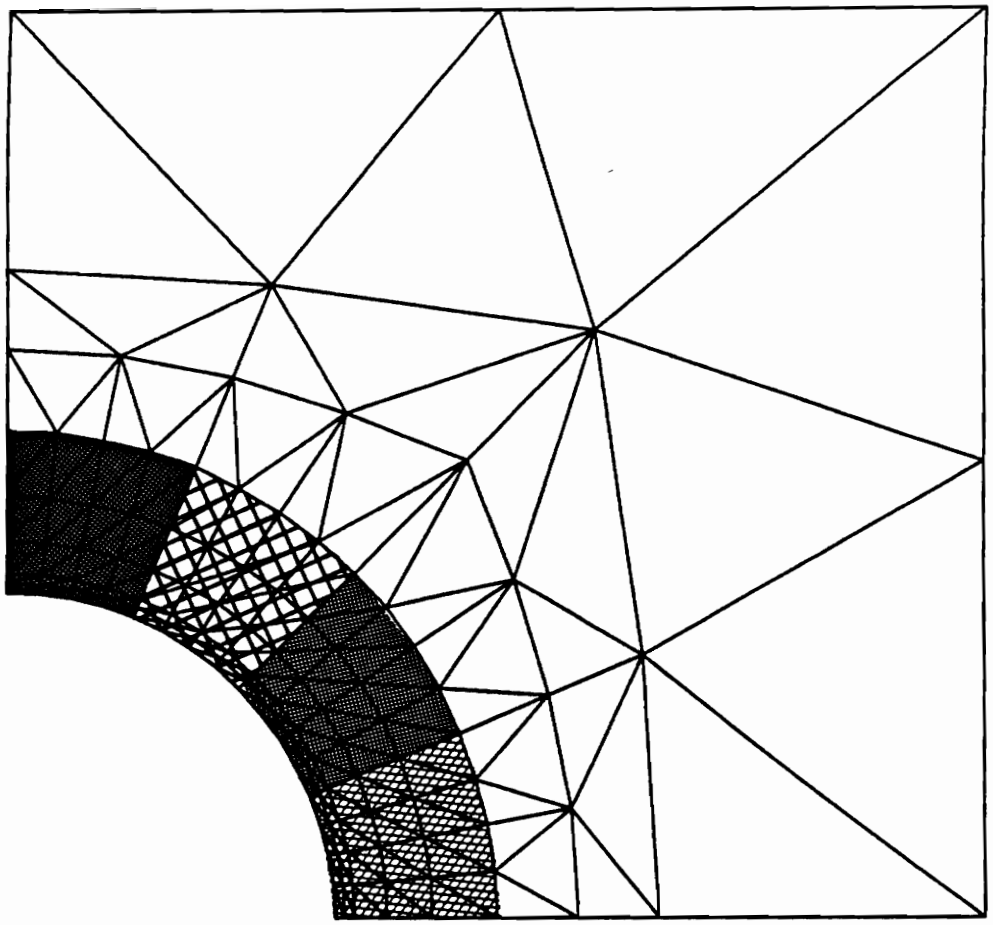

Figure 2.24 : Finite element mesh showing region of applied actuation strain for twenty-variable (4-sector) case

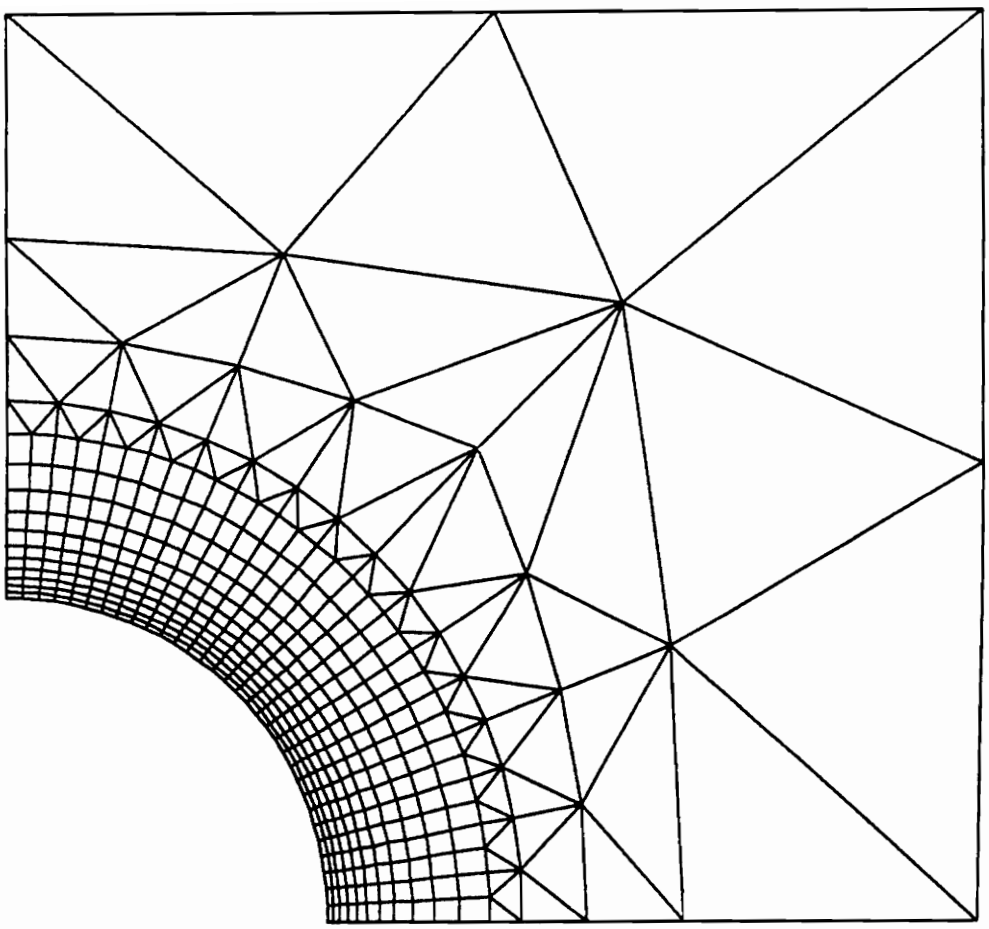

Figure 2.25 : Finite element mesh in the vicinity of the hole for composite plate

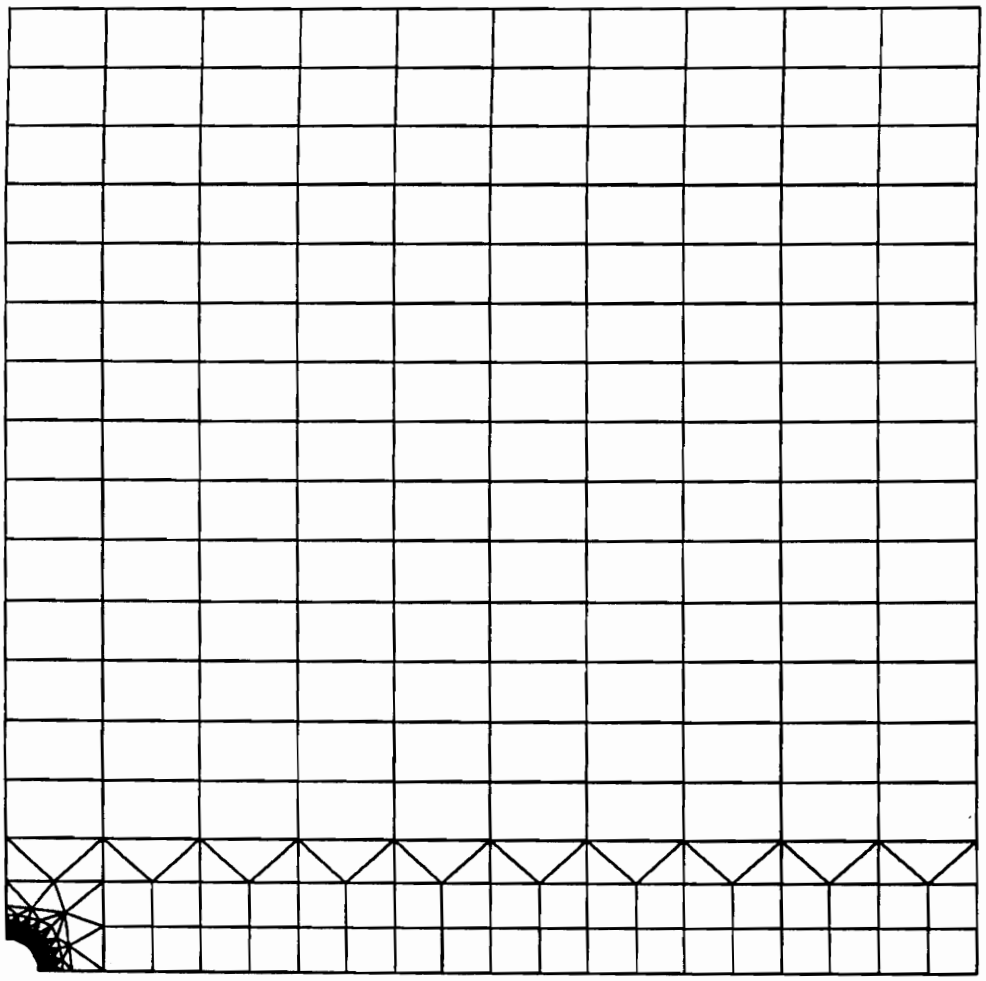

Figure 2.26 : Finite element mesh of the quarter plate model for composite plate

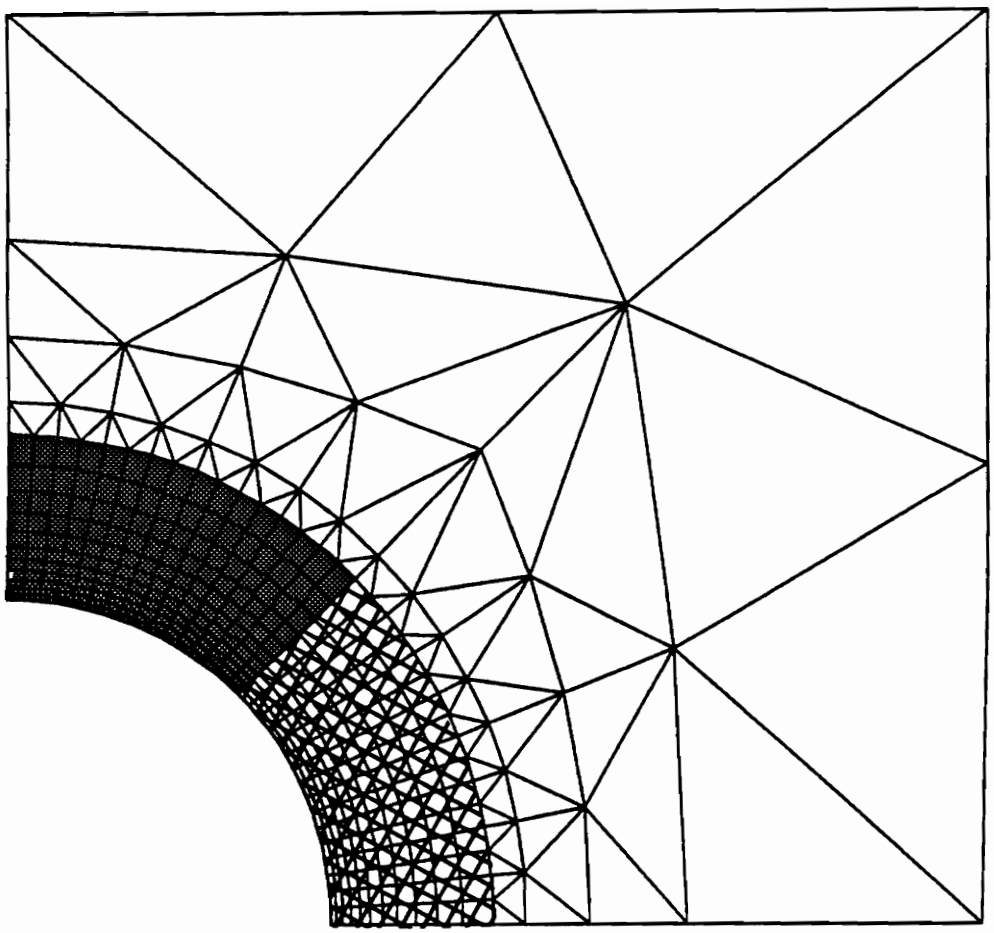

Figure 2.27 : Finite element mesh showing region of applied actuation strain for 22-variable (2-sector) case, actuation strain applied over $45^{o} < \theta < 90^{o}$ and $0 < \theta < 45^{o}$

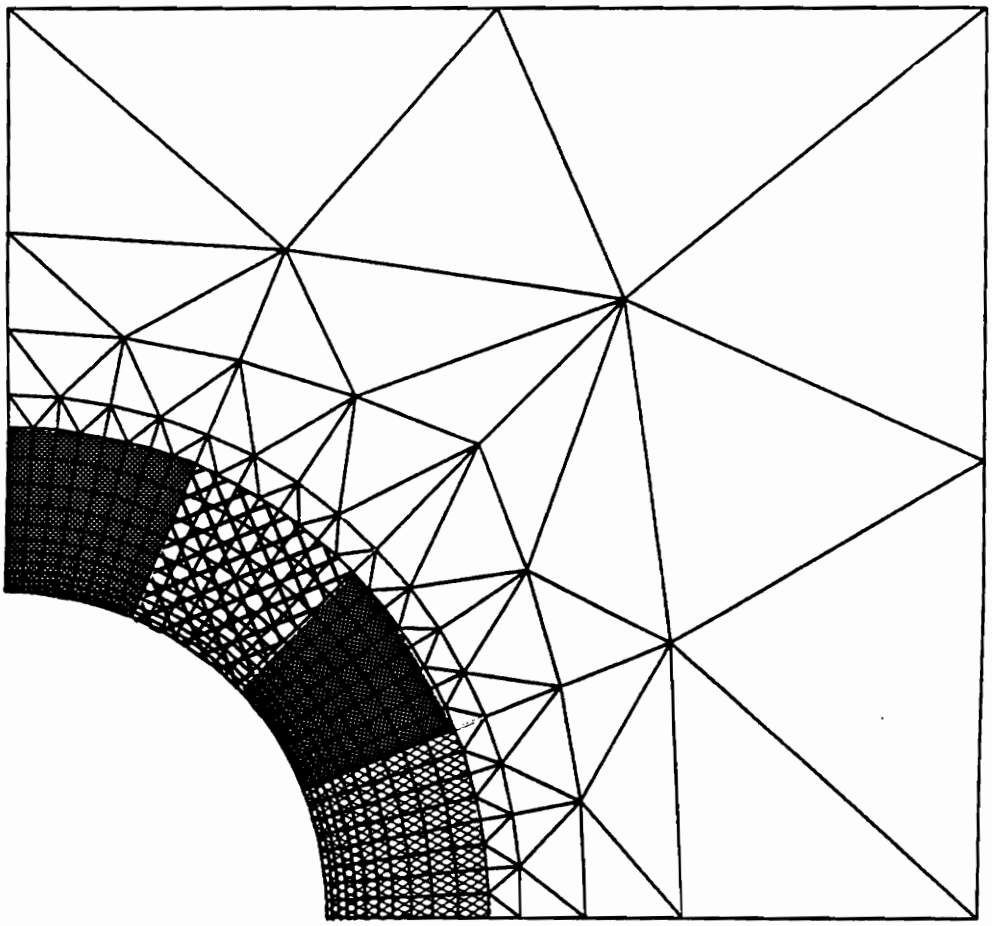

Figure 2.28 : Finite element mesh showing region of applied actuation strain for 44-variable (4-sector) case

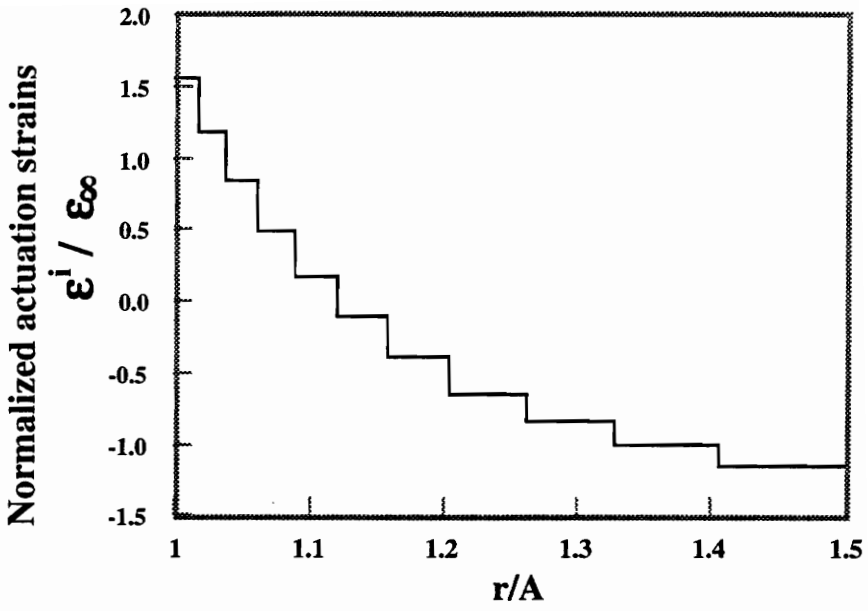

Figure 2.29 : Optimal axisymmetric actuation strain distribution; laminate $(0^\circ_2 / \pm 45^\circ / 0^\circ_2)_s$

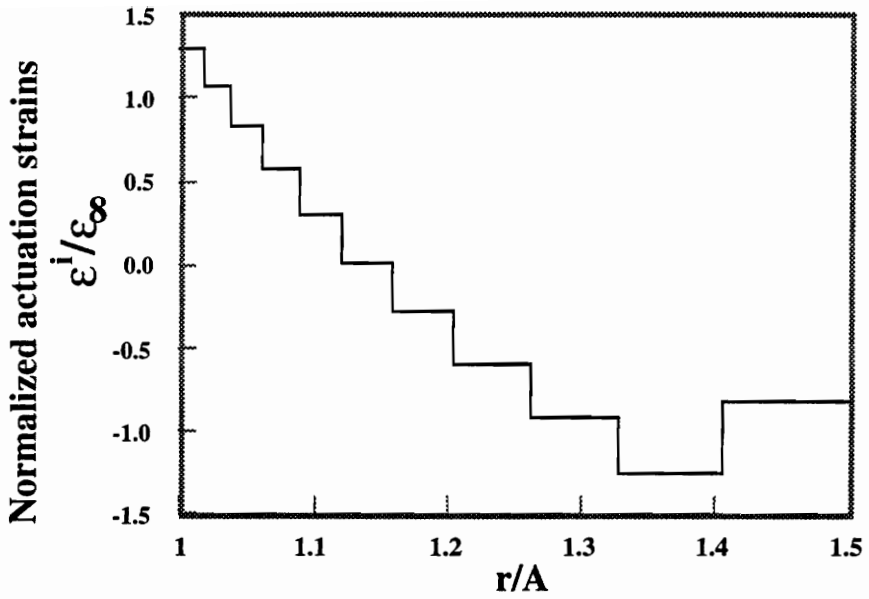

Figure 2.30 : Optimal axisymmetric actuation strain distribution; laminate $(\pm 45^{\circ} / 0^{\circ}_2 / \pm 45^{\circ} / 0^{\circ}_2)_s$

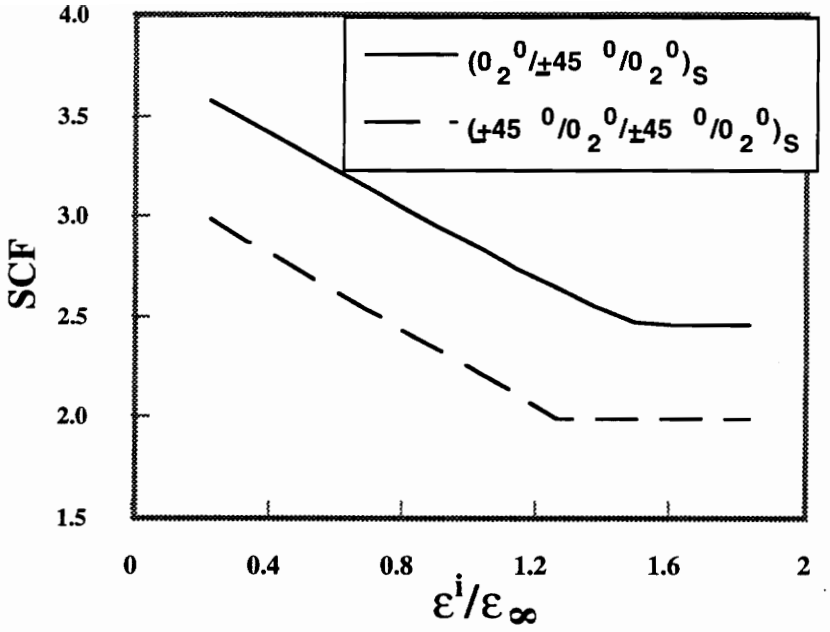

Figure 2.31 : Variation of SCF with available actuation strain magnitude (Axisymmetric case)

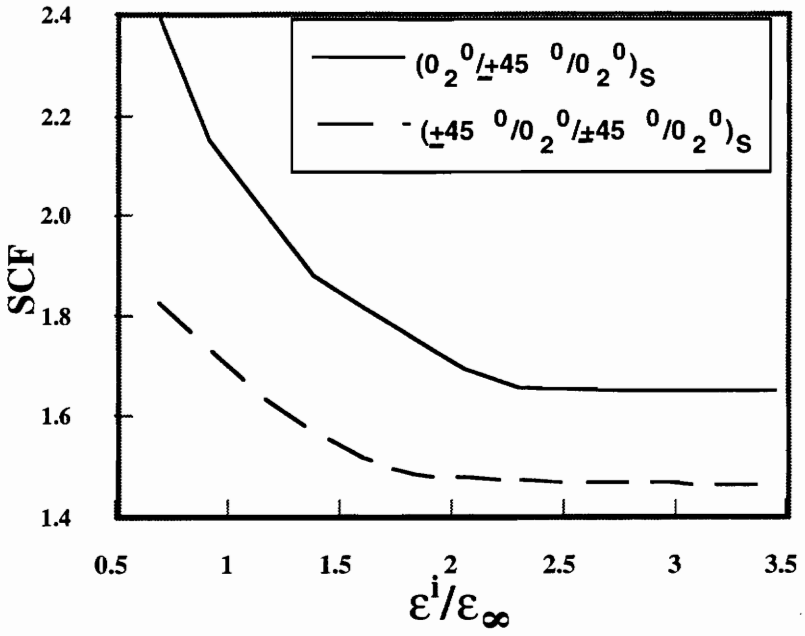

Figure 2.32 : Variation of SCF with available actuation strain magnitude (Non-axisymmetric case)

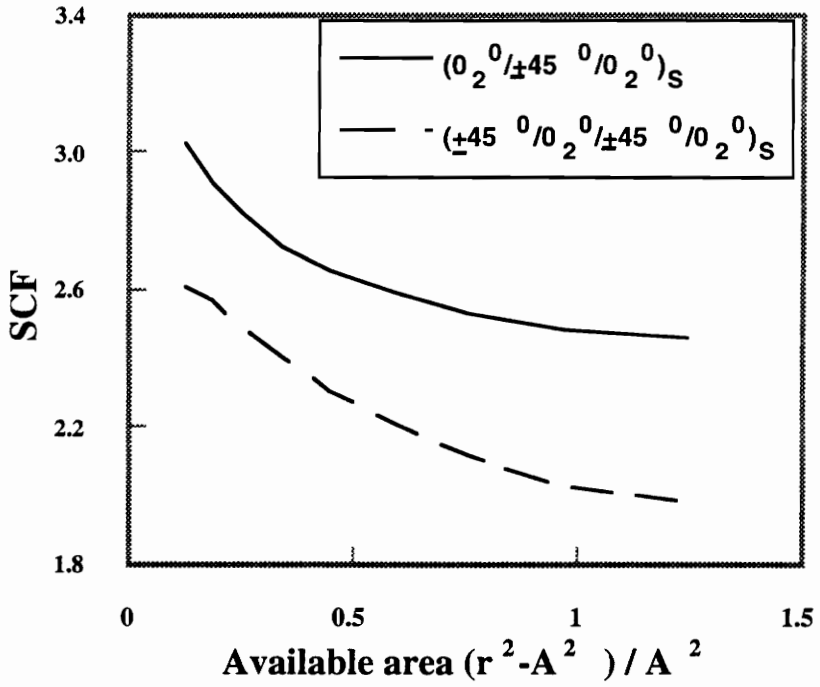

Figure 2.33 : Variation of SCF with available area over which actuation strains are applied (Axisymmetric case)

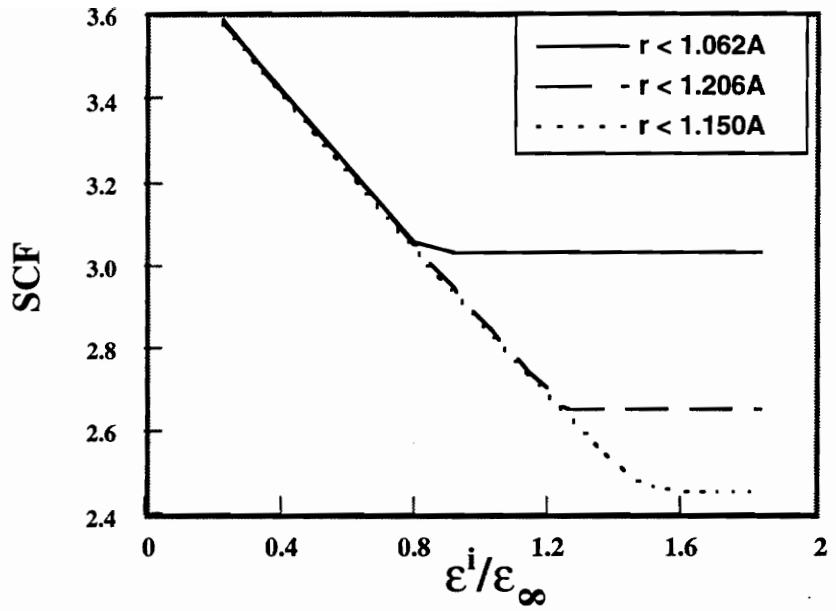

Figure 2.34 : Variation of SCF with available actuation strains for three different available area for,
Axisymmetric case ,Laminate $(0_2^0/\pm 45^0/0_2^0)_S$

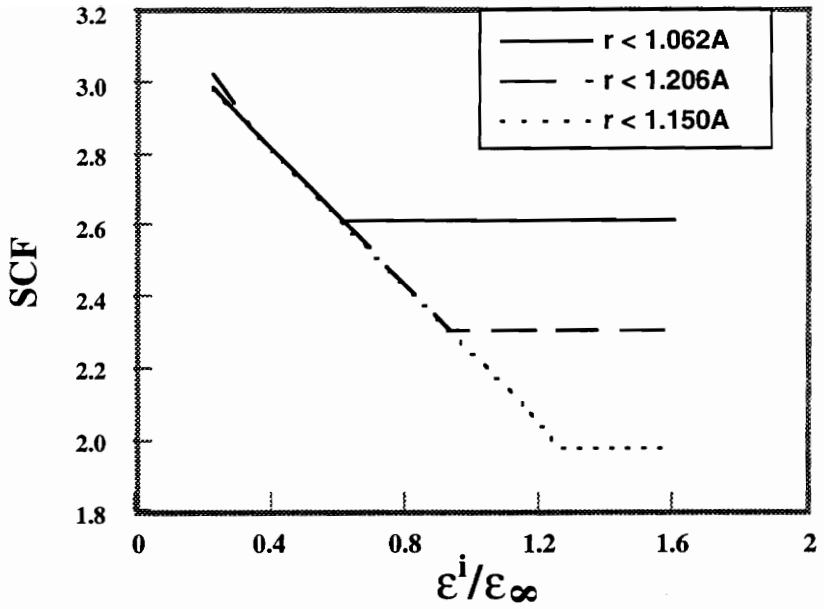

Figure 2.35 : Variation of SCF with available actuation strains
Axisymmetric case ,Laminate $(\pm 45^\circ/0_2^\circ/\pm 45^\circ/0_2^\circ)_S$

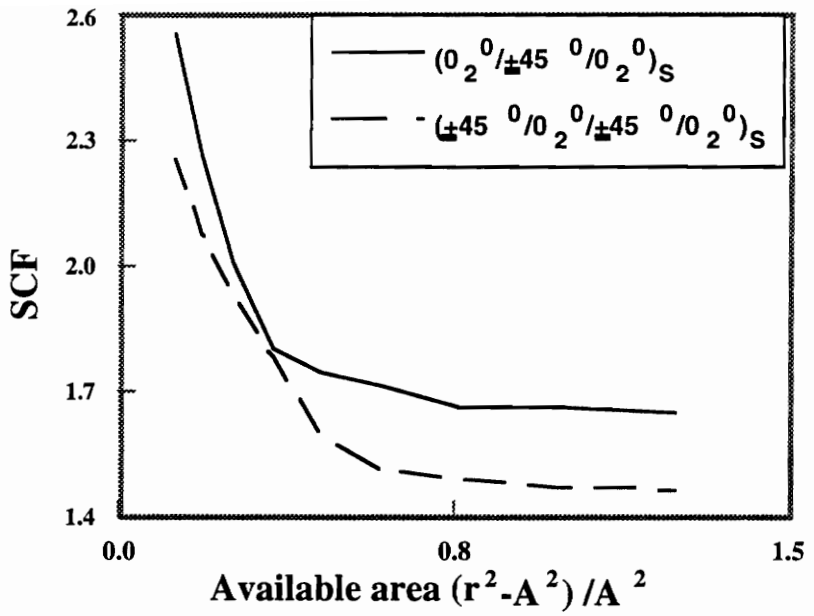

Figure 2.36 : Variation of SCF with available area over which actuation strains are applied (Non-axisymmetric case)

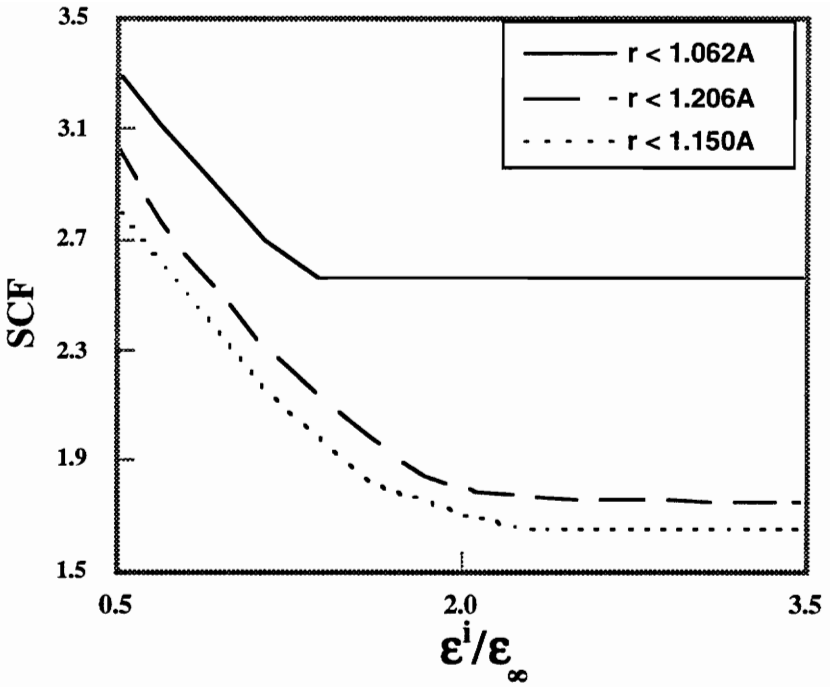

Figure 2.37 : Variation of SCF with available actuation strains for three different available area for 4-sector case non-axisymmetric case Laminate $(0^0_2/\pm 45^0/0^0_2)_S$

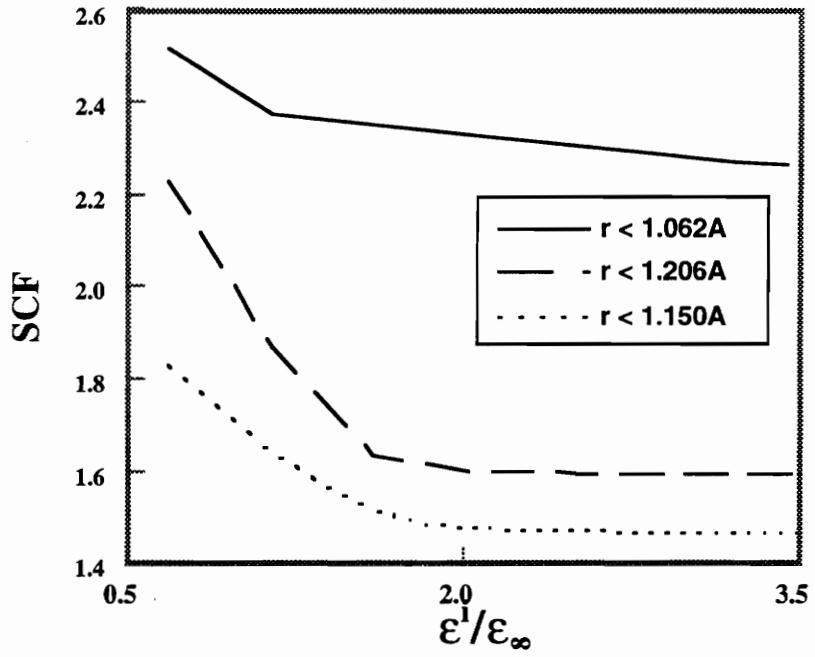

Figure 2.38 : Variation of SCF with available actuation strains for three different actuator area for 4-sector case non-axisymmetric case Laminate $(\pm 45^0/0^0_2/\pm 45^0/0^0_2)_S$

CHAPTER 3

AXISYMMETRIC PARTIAL THICKNESS ACTUATION

3.1 INTRODUCTION

In section 2.2.4.1 we have seen that the full-thickness axisymmetric actuation (ideal actuators) could reduce the stress concentraton factor for an isotropic plate with a hole from 3 to 2. However, in most cases actuators are either bonded to or embedded in the plate as shown in Figure 3.1, and do not occupy the entire thickness of the plate. Here, t_a is the thickness of each actuator and t_p is the thickness of the plate. Young's modulus and Poisson's ratio for the piezoelectric actuators were taken as E_a = 9 msi and ν_a = 0.3, respectively. In this chapter we investigate the effects of such partial-thickness actuators (realistic actuators) due to axisymmetric actuation.

3.2 ANALYSIS

The radial and tangential strains due to the actuator action in the plate and in the actuators can be written as

$$\epsilon_r^I = \frac{1}{E}(\sigma_r^I - \nu\sigma_\theta^I) + \epsilon_r^i \ , \tag{3.1}$$

$$\epsilon_\theta^I = \frac{1}{E}(\sigma_\theta^I - \nu\sigma_r^I) + \epsilon_\theta^i \ , \tag{3.2}$$

where ϵ_r^i , ϵ_θ^i are the radial and tangential applied induced strains and σ_r^I and σ_θ^I are the radial and tangential stresses due to actuator action. Note that the applied induced strains and the resulting stresses are not constant through the thickness. However, we assume that the actuation regions are symmetric through the thickness and that

the strains are constant through the thickness. For the axisymmetric partial thickness actuation, elastic properties of actuators were assumed to be identical to the plate material ($E = E_p = E_a$ and $\nu = \nu_p = \nu_a$). This simplication was used to obtain analytical solutions for the induced stresses in the plate and actuators. Integrating equations (3.1) and (3.2) through the thickness and dividing by the total thickness t_T, where

$$t_T = 2t_a + t_p \ , \tag{3.3}$$

we get

$$\epsilon_r^I = \frac{1}{t_T E}(N_r^I - \nu N_\theta^I) + \epsilon_r^* \ , \tag{3.4}$$

$$\epsilon_\theta^I = \frac{1}{t_T E}(N_\theta^I - \nu N_r^I) + \epsilon_\theta^* \ , \tag{3.5}$$

where ϵ_r^* , ϵ_θ^* are the average radial and tangential applied induced strains, i.e.,

$$\epsilon^* = \frac{1}{t_T}\int_{-\frac{t_T}{2}}^{\frac{t_T}{2}} \epsilon^i(z)dz \ . \tag{3.6}$$

In the present study we assume that we have constant applied induced strain in the actuator ($\epsilon^i = \epsilon_a^i$) and none in the plate, so that

$$\epsilon^* = \frac{2t_a}{t_T}\epsilon_a^i = \beta\epsilon_a^i \ , \tag{3.7}$$

where

$$\beta = \frac{2t_a}{t_T} \ . \tag{3.8}$$

N_r^I, N_θ^I are the stress resultants

$$N_r^I = \int_{-\frac{t_T}{2}}^{\frac{t_T}{2}} \sigma_r^I dz \ , \tag{3.9}$$

$$N_\theta^I = \int_{-\frac{t_T}{2}}^{\frac{t_T}{2}} \sigma_\theta^I dz \ . \tag{3.10}$$

For axisymmetric response the compatibility equation can be written as

$$\epsilon_\theta^I - \epsilon_r^I + r\frac{d\epsilon_\theta^I}{dr} = 0 \ , \tag{3.11}$$

and the equilibrium equation as

$$N_\theta^I = \frac{d}{dr}(rN_r^I) \ . \tag{3.12}$$

Substituting for ϵ_r^I and ϵ_θ^I from equations (3.4) and (3.5), and making use of the equilibrium equation, we obtain the compatibility equation in the following form

$$r\frac{d}{dr}\left(\frac{1}{r}\frac{d}{dr}(r^2N_r^I)\right) = -t_TEr\frac{d\epsilon_\theta^*}{dr} - t_TE(\epsilon_\theta^* - \epsilon_r^*) \ . \tag{3.13}$$

Integrating the above equation with free edge boundary conditions at r=A and at r $\rightarrow \infty$, we obtain

$$\begin{aligned} N_r^I = &-\frac{t_TE}{r^2}\int_A^r \epsilon_\theta^*\rho d\rho - \frac{t_TE}{r^2}\int_A^r\int_A^{\rho_1}\frac{\rho_1}{\rho}(\epsilon_\theta^* - \epsilon_r^*)d\rho d\rho_1 \\ &+\frac{t_TE}{2}\int_A^r\frac{(\epsilon_\theta^* - \epsilon_r^*)}{\rho}d\rho - \frac{t_TEA^2}{2r^2}\int_A^r\frac{(\epsilon_\theta^* - \epsilon_r^*)}{\rho}d\rho \ , \end{aligned} \tag{3.14}$$

and substituting N_r^I in the equilibrium equation, we get

$$\begin{aligned} N_\theta^I = &-t_TE\epsilon_\theta^* + \frac{t_TE}{r^2}\int_A^r \epsilon_\theta^*\rho d\rho + \frac{t_TE}{r^2}\int_A^r\int_A^{\rho_1}\frac{\rho_1}{\rho}(\epsilon_\theta^* - \epsilon_r^*)d\rho_1 d\rho \\ &-t_TE\int_A^r\frac{(\epsilon_\theta^* - \epsilon_r^*)}{\rho}d\rho + \frac{t_TE}{2}\int_A^r\frac{(\epsilon_\theta^* - \epsilon_r^*)}{\rho}d\rho \\ &+\frac{t_TEA^2}{2r^2}\int_A^r\frac{(\epsilon_\theta^* - \epsilon_r^*)}{\rho}d\rho \ . \end{aligned} \tag{3.15}$$

Equating ϵ_r^I and ϵ_θ^I from equations (3.1) , (3.2) and equations (3.4), (3.5), and solving for σ_r^I and σ_θ^I we get

$$\sigma_r^I = \frac{E}{t_TE}N_r^I + \frac{E}{1-\nu^2}[(\epsilon_r^* - \epsilon_r^i) + \nu(\epsilon_\theta^* - \epsilon_\theta^i)] \ , \tag{3.16}$$

$$\sigma_\theta^I = \frac{E}{t_TE}N_\theta^I + \frac{E}{1-\nu^2}[\nu(\epsilon_r^* - \epsilon_r^i) + (\epsilon_\theta^* - \epsilon_\theta^i)] \ , \tag{3.17}$$

where N_r^I and N_θ^I are given by equations (3.14) and (3.15). For the axisymmetric isotropic actuation with constant applied induced strain in the actuator, i.e. , $\epsilon_r^i = \epsilon_\theta^i = \epsilon_a^i$, and zero applied induced strain in the plate, the expressions for the stresses simplify. In the actuators we get

$$\sigma_{ra}^I = -\frac{E}{r^2}\int_A^r \epsilon^* \rho d\rho + \frac{E(\epsilon^* - \epsilon_a^i)}{1-\nu} , \tag{3.18}$$

$$\sigma_{\theta a}^I = \frac{E}{r^2}\int_A^r \epsilon^* \rho d\rho + \frac{E(\nu\epsilon^* - \epsilon_a^i)}{1-\nu} , \tag{3.19}$$

while in the plate we get

$$\sigma_{rp}^I = -\frac{E}{r^2}\int_A^r \epsilon^* \rho d\rho + \frac{E\epsilon^*}{1-\nu} , \tag{3.20}$$

$$\sigma_{\theta p}^I = \frac{E}{r^2}\int_A^r \epsilon^* \rho d\rho + \frac{\nu E\epsilon^*}{1-\nu} . \tag{3.21}$$

Note that equations (3.18) and (3.20) predict nonzero radial stresses at the hole boundary, r=A. This incorrect prediction is due to the 2-dimensional nature of analysis. Thus we can expect that above equations provide reasonable results only at a small distance away from the hole. For the full-thickness we have only actuators and $\beta = 1$ and the induced stresses are obtained from equations (3.18) and (3.20) as

$$\sigma_r^i = -\frac{E}{r^2}\int_A^r \epsilon^i \rho d\rho , \tag{3.22}$$

$$\sigma_\theta^i = \frac{E}{r^2}\int_A^r \epsilon^i \rho d\rho - E\epsilon^i . \tag{3.23}$$

The above stress expressions for the full-thickness actuation are same as those obtained in section 2.2.4.1.

3.3 DISCUSSION

The variation of stress concentration factor in the plate near the edge of the hole at $\theta = 90^0$ with normalized applied induced strains for full-thickness and partial-thickness actuations are shown in Figure 3.2 and Figure 3.3 for maximum shear stress and Von-Mises stress criteria, respectively.

In the case of full thickness actuation, when positive applied induced strains are applied, it can be seen from equations (3.22) and (3.23) that the induced stresses are compressive. Also, the induced tangential stresses are large in magnitude compared to the induced radial stresses. These induced stress distributions can produce large reduction in the total tangential stresses at the edge of the hole and the stress concentration factor. Figure 3.2 and Figure 3.3 confirm the results obtained in section 2.2.4.1 that the stress concentration can be reduced from 3 to 2 (at which point $\theta = 0^0$ becomes critical in compression).

For partial thickness actuation the situation is different because of the large radial stresses generated in the plate. Two partial-thickness actuation cases of bonded actuators are shown. For $\beta = 1/6$, the actuator thickness is small compared to the thickness of the plate. In the second case the thicknesses of the actuators and plate are same , i.e., $\beta = 1/2$. For both cases, the induced stress distributions are completely different from that obtained with full thickness actuation. We can see from equations (3.20) and (3.21), that near the hole the radial induced stress is larger than the induced tangential stress by a factor of $1/\nu$. When we apply negative applied induced strains, the induced radial stresses in the plate increase near the edge of the hole. This increases the stress concentration factor for both criteria, as shown in Figure 3.2 and Figure 3.3, even though the total tangential stress decreases. Positive applied induced strains, on

the other hand, induce tensile stresses in the plate and as we can see from the Figure 3.2, the SCF based on maximum shear stress criterion increases with the applied induced strains. However, the SCF based on the Von-Mises stress criterion, as can be seen from Figure 3.3, decreases as we increase the applied induced strain. But the decrease in stress concentration factor with partial-thickness actuation is small compared to the full-thickness actuation case. Similar results were obtained with embedded actuators also. Stresses in the actuators for Von-Mises stress criteria and maximum shear stress are shown in Figure 3.4 and 3.5, respectively. We can see that they are similar to those obtained in the plate for full-thickness actuation.

Thus it can be seen that the partial thickness actuation is ineffective for axisymmetric applied induced strain distribution. This is due to the large radial stresses produced by the actuators. This is in marked contrast to full-thickness actuation where the stress concentration factor could be reduced from 3 to 2 by axisymmetric distributions. However, non-axisymmetric induced strain distributions can be used, as discussed in Chapter 4 and Chapter 5, to reduce stresses in the region of high stress concentration.

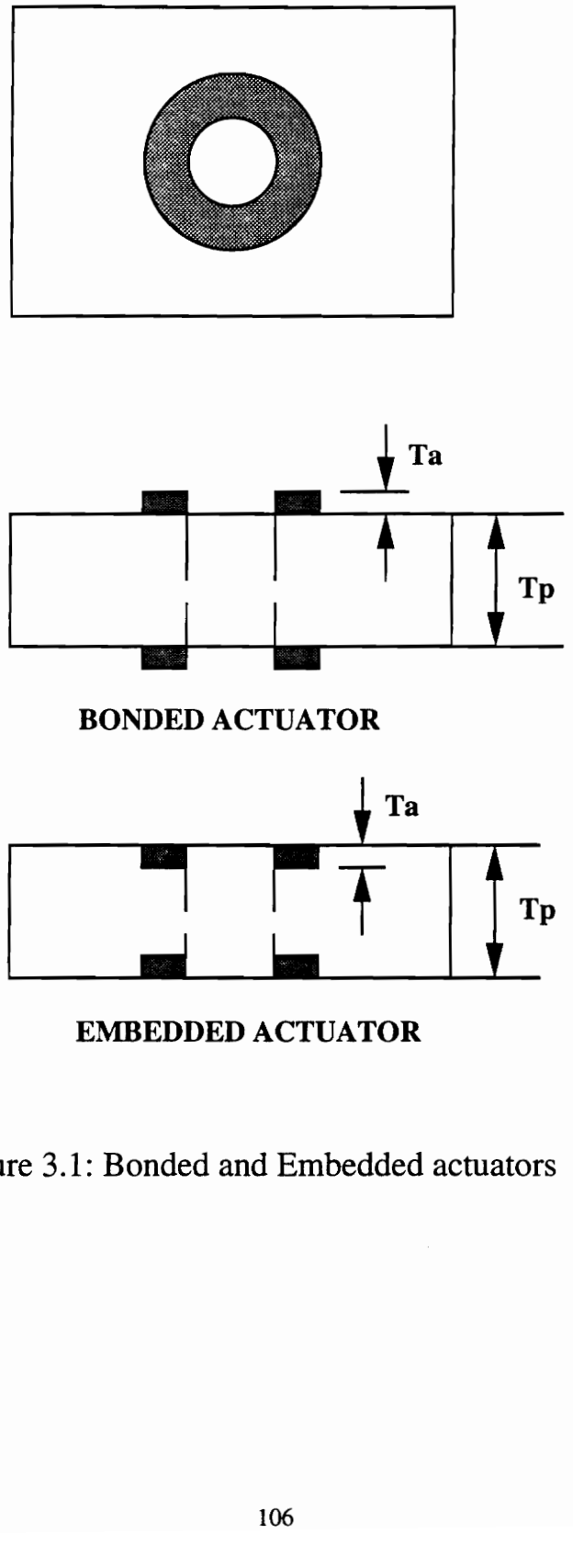

Figure 3.1: Bonded and Embedded actuators

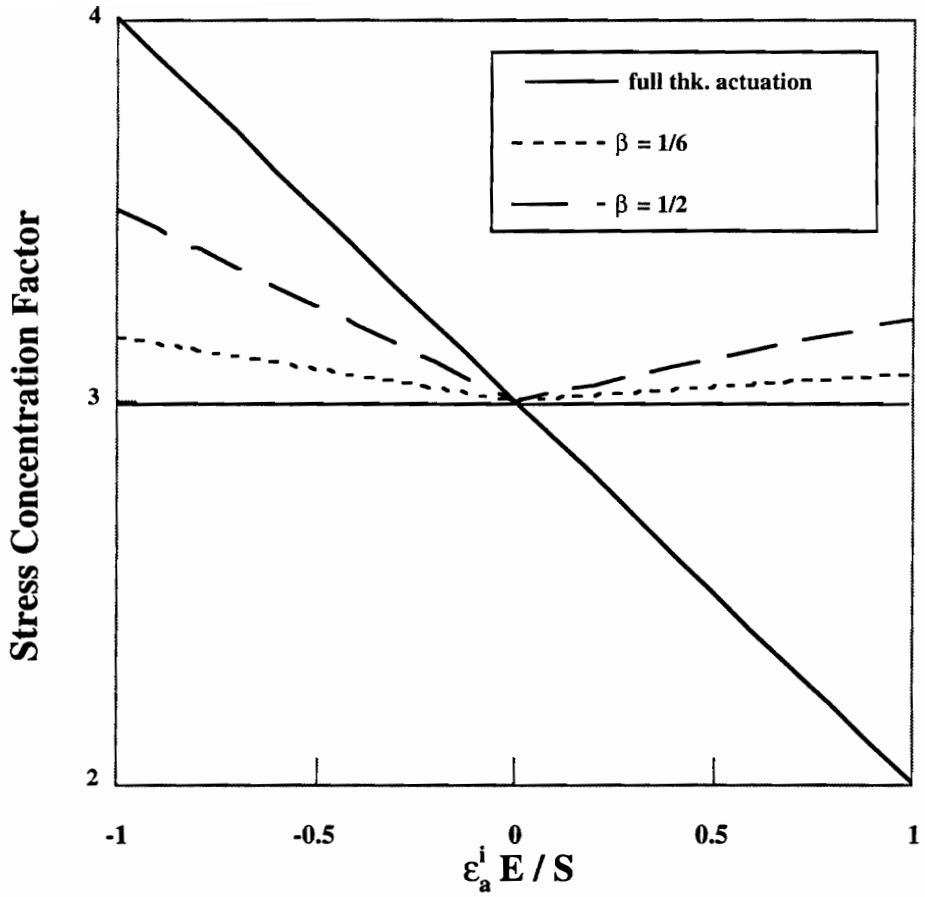

Figure 3.2 : Effect of full and partial thickness actuation on stress concentration factor in the plate near the edge of the hole at $\theta=90^0$, $\nu=0.3$, for axisymmetric actuation for two ratios of actuator thickness to plate thickness, β (Maximum shear stress criterion)

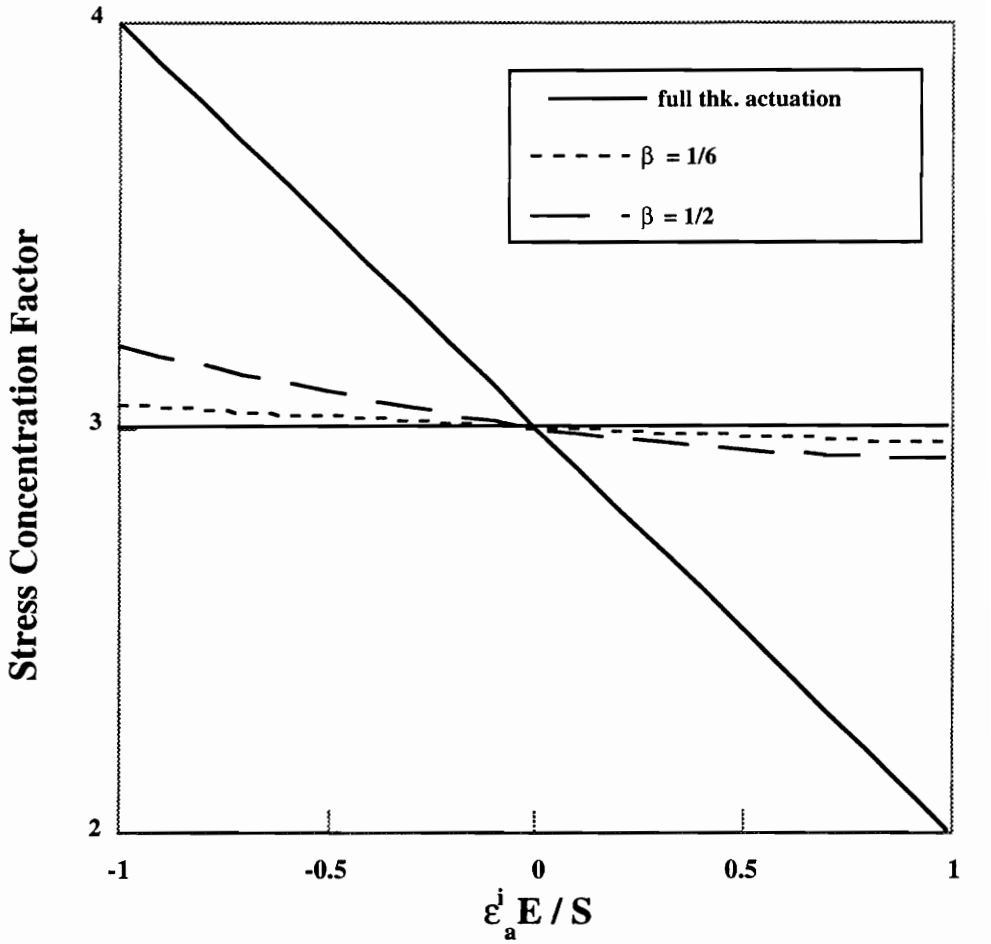

Figure 3.3 : Effect of full and partial thickness actuation on stress concentration factor in the plate near the edge of the hole at $\theta=90^0$, $\nu=0.3$, for axisymmetric actuation for two ratios of actuator thickness to plate thickness, β (Von-Mises stress criterion)

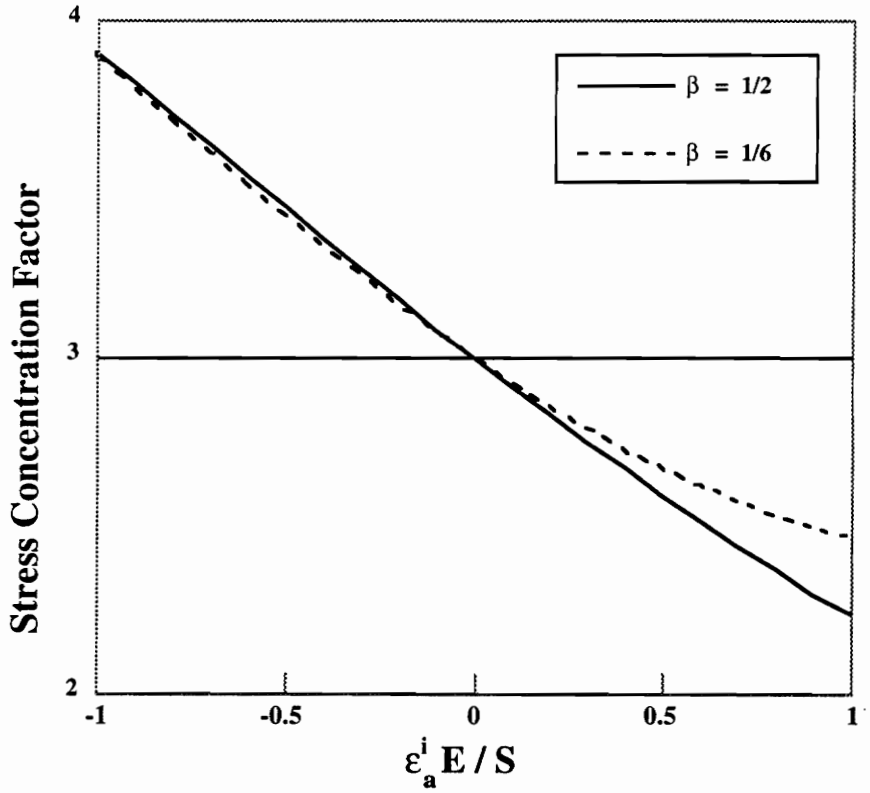

Figure 3.4 : Effect of full and partial thickness actuation on stress concentration factor in actuator near the edge of the hole at $\theta=90^0$, $\nu=0.3$, for axisymmetric actuation for two ratios of actuator thickness to plate thickness, β (Von-Mises stress criterion)

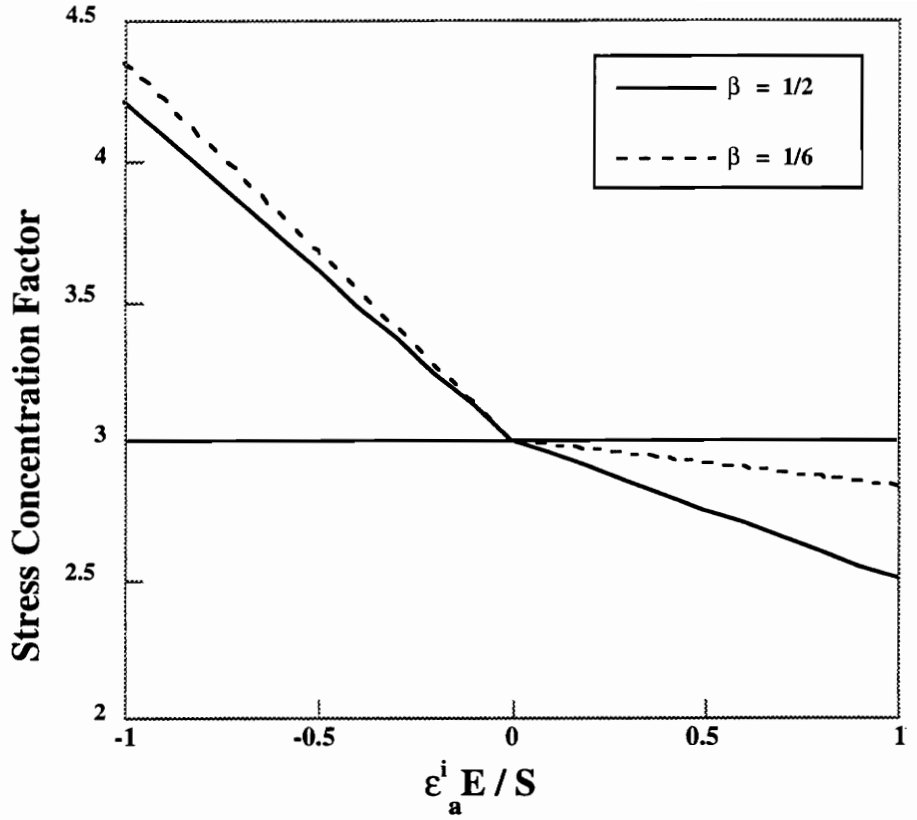

Figure 3.5 : Effect of full and partial thickness actuation on stress concentration factor in actuator near the edge of the hole at $\theta=90^0$, $\nu=0.3$, for axisymmetric actuation for two ratios of actuator thickness to plate thickness, β (Maximum shear stress criterion)

CHAPTER 4

STRESS REDUCTION USING REALISTIC LIMITS ON ACTUATORS - FATIGUE LOAD CASE (NON-AXISYMMETRIC ACTUATION)

4.1 REALISTIC ACTUATORS

In this chapter we investigate the effects of present technology limitations on piezoelectric actuators (non-axisymmetric actuation) on the potential reductions in stress concentrations when the loads are repetitive in nature. Compared to the work in Chapter 2, we considered four limitations on the effectiveness of actuators:

(i) Actuators account for only part of the thickness of the plate,

(ii) the magnitude of applied induced strains is limited to 1000 $\mu\epsilon$,

(iii) the actuators may fail,

(iv) small actuators suffer shear lag effects.

As in Chapter 2, we dealt with reduction of stress concentration in a plate with a hole. Numerical optimization based on finite element simulations was used to obtain applied induced strain distributions in an isotropic plate with a hole. We applied uniform compression of S=-10 ksi which corresponds to a fatigue limit of 30 ksi for aluminum without active actuation.

4.2 PROBLEM DEFINITION

A 0.1 inch thin 30 inch square plate with a 1 inch diameter circular hole under uniax-

ial compressive load S, as shown in Figure 2.1 was used throughout this study. We studied uniaxial load case of -10 ksi. The plate is made of aluminum with Young's modulus E_p = 10 Msi, Poisson's ratio ν_p = 0.3, and coefficient of thermal expansion $\alpha_r = \alpha_\theta = \alpha$ = 2.3 x $10^{-5} 1/^oC$. Our goal, again, was to reduce the stress concentration as measured by Von-Mises or the maximum shear stress criteria by adding non-axisymmetric applied induced strain fields with the piezoelectric actuators. In this case, as shown in Figure 3.1, the actuators are either bonded to or embedded in the plate. Young's modulus and Poisson's ratio for the piezoelectric actuators were taken as E_a = 9 msi and ν_a = 0.3, respectively.

The plate was modeled by a quarter plate finite element model and was analyzed using EAL. The finite element model was same as described in section 2.2.1 and shown in Figure 2.2 and Figure 2.3.

4.3 VALIDATION OF FINITE ELEMENT MODEL

To validate the EAL finite element model, we compared the strains predicted by EAL with the experimental and theoretical results of Crawley and Lazarus [42]. For this comparison one quarter of the 5.1 cm square substrate/actuator/substrate, shown in Figure 4.1, was modeled with sixteen plain stress elements. The results are shown in Table 4.1 and show very good agreement.

4.4 CRITERION FOR ACTUATOR FAILURE

Piezoceramics have low tensile strength (9 ksi assumed here) and high compressive strength (75 ksi assumed here), so that strength criteria used for ductile materials (e.g., Von-Mises, maximum shear) are not applicable. Since piezoceramics are brittle, we used a simplified version of the Mohr's criterion for brittle materials to predict actuator

failure. This criterion predicts the effect of a given state of plane stress on a brittle material when the tensile strength (σ_{UT}) and the compressive strength (σ_{UC}) for the material are available [61, page 318-319]. If both principal stresses (σ_1, σ_2) are positive, the state of stress is safe as long as (Figure 4.2)

$$max\,(\sigma_1, \sigma_2) \leq \sigma_{UT}. \tag{4.1}$$

If both the principal stresses are negative, the state of stress is safe as long as

$$max\,(|\sigma_1|, |\sigma_2|) \leq \sigma_{UC}. \tag{4.2}$$

If the principal stresses have opposite sign, then the state of stress is safe when the stresses are within the shaded region in Figure 4.2 bounded by straight lines in the 2nd and 4th quadrant. To alleviate problems with actuator failure and increase the effectiveness of the actuators we considered prestressing them by heating and cooling before they are attached to the plate.

Since civil aircraft upper wing skins experience fluctuating compressive loads most of the time, compressive strength of piezoceramics was reduced to 30 ksi (40 % of the actual strength) without affecting the tensile strength for the fatigue load case. However, compressive strength was not changed for prestressed actuators.

4.5 PROBLEM FORMULATION

The total stresses in the plate are given as

$$\sigma_r^{tot} = \sigma_r^M + \sigma_r^I, \tag{4.3}$$

$$\sigma_\theta^{tot} = \sigma_\theta^M + \sigma_\theta^I, \tag{4.4}$$

$$\tau_{r\theta}^{tot} = \tau_{r\theta}^M + \tau_{r\theta}^I, \tag{4.5}$$

where σ_r^I , σ_θ^I and $\tau_{r\theta}^I$ are the radial, tangential and shear stresses, respectively, due to actuator action and σ_r^M , σ_θ^M and $\tau_{r\theta}^M$ are the corresponding stresses due to applied loading.

For the optimization, we seek the applied induced strain distribution that minimizes the maximum equivalent stress in the plate, where for equivalent stress we use either the Von-Mises stress or an equivalent stress based on the maximum shear stress criterion, as described in section 2.2.2. The stress concentration factor was defined as the ratio of the maximum equivalent stress to the applied stress (i.e., σ_{eq} /S).

The design variables were the values of applied induced strains ϵ_k^i, k=1,...,n in n regions of the plate as well as prestressing temperatures in these regions T_k^i. As before the value of the maximum equivalent stress, σ_{max}, was an additional design variable. Stresses in actuators were limited by Mohr's criterion and the applied induced strains in the actuators were limited to 1000 $\mu\epsilon$. As an additional safety margin, actuator stresses due to prestressing only (σ_a^p) were limited between -60 ksi (σ_a^{pm})and 0. The optimization problem was then formulated as

$$
\begin{aligned}
&\textit{minimize} \quad \sigma_{max} \\
&\textit{such that} \quad \sigma_{eq}^j(\epsilon_k^i, T_k^i) \leq \sigma_{max} \quad j = 1, ..., n_e, \\
&\qquad \sigma_a^M(\epsilon_k^i, T_k^i) \leq \sigma_a^{max} \\
&\qquad \sigma_a^{pm} \leq \sigma_a^p(T_k^i) \leq 0 \\
&\qquad |\epsilon_k^i| \leq 1000\mu\epsilon \ , \\
&\qquad T_k^i \leq 300^oC \ .
\end{aligned}
\tag{4.6}
$$

The constraints require that the equivalent stress, σ_{eq} for the element j is lower than σ_{max} at n_e element centers which were selected to represent the possible critical areas of the plate. σ_a^M are the stresses in actuators, and σ_a^{max} are the allowable stresses in actuators

according to the Mohr's criterion (Figure 4.2). σ_a^p are the stresses in actuators due to prestressing only, and σ_a^{pm} are the allowable stresses in actuators due to prestressing, as explained above. The maximum temperature in the actuators was limited to 300 ^oC, which is the Curie temperature of piezoceramics because the spontaneous polarizations in ceramics are lost if the temperature is raised above Curie temperature. Optimization was carried out by sequential linear programming (SLP) using the MINOS package [56].

4.6 NON-AXISYMMETRIC PARTIAL THICKNESS ACTUATION

An applied displacement of -0.015 inch was used as the mechanical load in the analysis. This corresponds to nominal strain ϵ_∞ = - 0.001 and compressive stress σ_∞ = -10 ksi in the absence of the hole. From the analysis, the highest yield stresses for Von-Mises and maximum shear stress criteria were obtained as 28.45 ksi and 28.89 ksi, respectively. Since the analytical solution for a plate with a hole predicts 30 ksi for the equivalent stresses, all the numerical results were scaled corresponding to the analytical stress values. Actuators were placed over the area $A \leq r \leq 1.5A$ consisting of 5 rings as shown in Figure 4.3.

4.6.1 Effect of applied induced strain constraint

First we considered the effect due to applied induced strain constraint only. In this case, the five rings in the vicinity of the hole were divided into four sectors, 22.5^0 each and actuators were placed on each of these sectors, leading to a twenty-variable optimization problem. When actuators are bonded to or embedded in the plate, we have both passive as well as active effects on the stress concentration factor. Passively (i.e., before actuation), bonded actuators will reduce the SCF whereas embedded actuators

will increase the SCF. Optimizations were carried out for seven different actuator thicknesses ($2t_a/t_p$ = 0.2, 0.3, 0.4, 0.5, 0.6, 0.7, 0.8) with constraints on actuation strains only. The reduction in SCF for the Von-Mises and maximum shear stress criteria for the bonded and embedded actuator are shown in Figure 4.4 and Figure 4.5, respectively. Passive and total reductions are shown in Table 4.2 and Table 4.3 for Von-Mises and maximum shear stress criteria, respectively. The figures show that for thin actuators the limit on applied induced strains does not permit much reduction in SCF. But for thick actuators the SCF reduction is substantial. For $2t_a/t_p$ = 0.8, the SCF based on Von-Mises stress criterion could be reduced to 1.84 and 2.15 with bonded and embedded actuators, respectively. We get smaller reductions in SCF with embedded actuators than with bonded actuators. In the bonded case, however, we may have shear lag effects, unmodelled in the present analysis, which will reduce the effectiveness of the actuators. The shear lag effect is absent in the embedded case.

In the finite element modelling, we ignored the through-the-thickness variation of the stresses, and the shear lag effect. The shear lag effect was checked with the linear shear stress variation model (LSSVM) using a program developed by Lin and Rogers [62]. It was found that the thick and small actuators exacerbate the shear lag effect. To alleviate this problem to some extent, the lengths of the actuators were increased from 0.015 inch to 0.08 inch by combining the first three rings, as shown in Figure 4.6, leading to a twelve-variable problem. The variation of axial stresses through the actuator thickness (for applied induced strain of 1000 $\mu\epsilon$) at stations S1 and S2 (Figure 4.7) for small (l_a=0.015 inch) and long actuators (l_a = 0.07 inch) and, for $2t_a/t_p$ = 0.2 are shown in Figure 4.8. We can see that for l_a = 0.07 inch, at both the stations, axial stresses are almost constant through the thickness of the actuator, whereas for l_a = 0.015 inch, axial stress at S1 drops from 8253 psi at the plate-actuator interface to 2213 psi at the top

surface of the actuator and at S2 stresses drop from 8313 psi to 1686 psi. Figure 4.9 shows similar results for $2t_a/t_p = 0.8$. In this case, we can see that for both, long as well as short actuators, axial stresses drop drastically from the plate-actuator interface to the top surface of the actuator. For our subsequent analysis, to reduce the shear lag effect, $2t_a/t_p$ was taken as 0.2 for bonded actuators. The optimization with 12 variables was carried out for the actuator thickness $2t_a/t_p = 0.2$. Results for 12-variable case are compared that with the 20-variable case in Table 4.4. With twelve actuators, the SCF for the Von-Mises criterion was reduced from 3 to 2.62, compared to 2.56 obtained with twenty actuators.

For the embedded case, the optimizations were also carried out with the additional requirement that only tangential actuation strains can be applied. Results for embedded actuators are shown in Table 4.5 for Von-Mises and maximum shear stress criteria. We can see that the reduction in SCF is smaller than that obtained in the isotropic expansion case. For $2t_a/t_p = 0.8$, the SCF was reduced to 2.27 in this case for Von-Mises stress criterion, compared to 2.15 obtained for the isotropic expansion case (see Table 4.2).

4.6.2 Effect of applied induced strain and actuator stress constraints

Optimizations were next carried out by putting additional constraints on the actuator stresses using the Mohr's criterion described before. Due to the low tensile strength of piezoceramics, stress constraints were active in the region of high tensile stresses, i.e., near the hole around $\theta = 0^o$. With bonded actuators, for $2t_a/t_p = 0.2$ (12 variable case), the SCF was reduced from 3 to 2.66 for the Von-Mises criterion, compared to 2.56 obtained for the case when actuator failure was not accounted for. For the embedded case, the optimizations were carried out for seven different thicknesses ($2t_a/t_p = 0.2, 0.3, 0.4, 0.5, 0.6, 0.7, 0.8$). Figure 4.10 and Figure 4.11 compare the Von-Mises and maximum

shear stress based SCF with and without actuator stress constraints, respectively. It can be seen that, the actuator stress constraints increase the SCF by 2 to 3 percent.

4.6.3 Prestressing

To improve their performance, actuators can also be prestressed and then bonded or embedded to the structure. If the actuators are cooled below room (or operating) temperature and then bonded or embedded to the structure, the actuators will try to expand as the temperature rises. The structure restricts this expansion and this process will generate compressive stresses in the actuators and tensile stresses in the structure. If the actuators are heated above room temperature and then bonded or embedded to the structure, tensile stresses will be induced in the actuators and compressive stresses in the structures. These properties can be used to reduce the stresses in the structure.

In all our previous work, we have considered that the plate is either in compression or in tension. However, in reality, most structures undergo both compressive and tensile loadings. The relative magnitudes of the compressive and tensile loading depend on the applications. For civil aircraft upper wing skins, a typical relative magnitude is about 2.5:1. The structure must be designed so that it is capable of withstanding both kinds of loadings.

For prestressing, we need to consider both kinds of loading, i.e., tensile and compressive loadings. If the structure is designed only for one kind of loading, for example, say tensile loading, then the actuators can be prestressed to induce compressive stresses in the structure to reduce the stress concentration factor. However, in this prestressed state if compressive loads are applied, the compressive stresses due to combined effect of prestressing and applied loading may fail the structure. For our study, it was assumed

that the uniaxial loading on the plate varies between -10 ksi and 4 ksi. Since the SCF is 3, the maximum stresses will vary between -30 ksi and 12 ksi without the actuators. Twelve actuators were placed between $A \leq r \leq 1.5A$, as described before. We considered all the three effects, i.e., passive, prestressing and active effects of piezoelectric actuators on the reduction of SCF. For the bonded case, optimization was carried out for $2t_a/t_p = 0.2$. The results are shown in the Table 4.6 for Von-Mises stress criterion. Optimal temperatures for prestressing and optimal applied induced strains are given in Table 4.7. We can see that prestressing can reduce the SCF by an additional 7 to 9 percent. Table 4.8 and Table 4.9 show the corresponding results for maximum shear stress criterion.

4.7 SUMMARY

With non-axisymmetric actuation strains, the reductions obtained in SCF were small due to limits on applied induced strains. However, by increasing the thicknesses of the actuators large reductions in SCF were still possible. For $2t_a/t_p = 0.8$, where t_p is the thickness of the plate and t_a is the thickness of the actuators on each side of the plate, the SCF could be reduced to 1.84 and 2.15 with bonded and embedded actuators, respectively.

Actuator failure was considered next, with stresses in the actuators limited by a simplified Mohr's criterion. This additional constraint was found to increase SCF by 2 - 3 %. The results obtained with the bonded actuators also did not account for the shear lag effect, which was found to be large for small and thick actuators. To increase the effectiveness of the actuators and also to alleviate the problem of actuator failure, actuators were prestressed before attaching to the plate. It was found that prestressing could reduce the SCF by an additional 7 - 9 %.

For the fatigue load case, as can be seen from the results that the actuators are effective even with present technology limitations. However, in this case actuators will be called upon frequently and due to that the energy expenditure could be substantial. Also we may have fatigue problems with the actuators themselves.

Table 4.1. Comparison of EAL results with Crawley et al. [42]

Plate thickness (cm)	Actuation Strains ($\mu\epsilon$)	Strains ($\mu\epsilon$)		
		Crawley et al.		EAL
		Experimental	Theoretical	Model
0.32	150	38.10	39.70	39.02
0.51	145	28.10	26.60	26.20
0.84	141	14.60	16.90	16.65

Table 4.2. Stress Concentration Factors with Bonded and Embedded actuators for Von-Mises stress Criterion. Non-axisymmetric actuation, Free strain limited to 1000 $\mu\epsilon$

2ta/tp	*Stress Concentration Factor**			
	Bonded Actuators		Embedded Actuators	
	Passive effect	Total effect	Passive effect	Total effect
0.2	2.83	2.56	3.02	2.68
0.3	2.76	2.38	3.03	2.53
0.4	2.69	2.22	3.04	2.41
0.5	2.62	2.10	3.05	2.32
0.6	2.56	2.00	3.06	2.24
0.7	2.50	1.91	3.07	2.19
0.8	2.44	1.84	3.08	2.15

* The stress concentration factor without actuators is 3.00

Table 4.3.Stress Concentration Factors with Bonded and Embedded actuators for Max. shear stress Criterion. Non-axisymmetric actuation, free strain limited to 1000 $\mu\epsilon$

2ta/tp	*Stress Concentration Factor**			
	Bonded Actuators		Embedded Actuators	
	Passive effect	Total effect	Passive effect	Total effect
0.2	2.83	2.55	3.02	2.68
0.3	2.76	2.38	3.03	2.55
0.4	2.69	2.23	3.04	2.45
0.5	2.62	2.12	3.05	2.36
0.6	2.56	2.03	3.06	2.30
0.7	2.50	1.94	3.07	2.25
0.8	2.44	1.86	3.08	2.20

* The stress concentration factor without actuators is 3.00

Table 4.4. Comparison of reduction in SCF for 12-variable and 20-variable cases (Bonded, 2ta/tp=0.2) Free induced strain limited to 1000 $\mu\epsilon$

Criterion	20-variable	12-variable
Von-Mises	2.56	2.62
Max. Shear	2.46	2.58

Table 4.5. Reduction in SCF for embedded actuators,

Tangential actuation strain only, $\epsilon_r^i = 0$

Free induced strain limited to 1000 $\mu\epsilon$

2ta/tp	*Stress Concentration Factor**			
	Von-Mises crit.		Max. shear crit.	
	Passive effect	Total effect	Passive effect	Total effect
0.2	3.02	2.79	3.02	2.77
0.3	3.03	2.69	3.03	2.65
0.4	3.04	2.59	3.04	2.56
0.5	3.05	2.50	3.05	2.47
0.6	3.06	2.42	3.06	2.39
0.7	3.07	2.34	3.07	2.33
0.8	3.08	2.27	3.08	2.26

* The stress concentration factor without actuators is 3.00

Table 4.6. Reduction in SCF for Bonded and Embedded actuators, Von-mises stress criterion (2ta/tp = 0.2), constraints on actuation strains and actuator stresses

Actuators	Stress Concentration Factor		
	Passive	Passive & Prestressing	Passive, Prestressing & Active
Bonded	2.83	2.56	2.35
Embedded	3.02	2.72	2.47

Table 4.7. Optimal prestressing temperatures and actuation strains for bonded and embedded actuators, Von-Mises stress criterion (2ta/tp = 0.2)

Actuators locations (Figure 4.6)	Pres. Temperatures ($°C$)		Actuation Strains ($\mu\epsilon$)	
	Bonded	Embedded	Bonded	Embedded
1	44.6	48.7	-533	-510
2	15.3	11.4	-405	-520
3	18.6	7.7	-751	-1000
4	37.0	32.5	-826	-1000
5	225.9	202.1	158	-340
6	31.7	32.7	-966	-1000
7	19.5	19.7	-1000	-1000
8	21.9	22.8	-1000	-1000
9	178.0	180.4	897	1000
10	27.8	26.2	-883	-1000
11	10.9	20.5	-1000	-781
12	19.1	3.0	-612	-1000

Table 4.8. Reduction in SCF for Bonded and Embedded actuators, Maximum shear stress criterion, (2ta/tp = 0.2), constraints on actuation strains and actuator stresses

Actuators	Stress Concentration Factor		
	Passive	Passive & Prestressing	Passive, Prestressing & Active
Bonded	2.83	2.59	2.33
Embedded	3.02	2.78	2.47

Table 4.9. Optimal prestressing temperatures and actuation strains for bonded and embedded actuators, Maximum Shear stress criterion (2Ta/Tp = 0.2)

Actuators locations (Figure 4.6)	Pres. Temperatures ($°C$)		Actuation Strains ($\mu\epsilon$)	
	Bonded	Embedded	Bonded	Embedded
1	63.2	66.4	-1000	-1000
2	16.1	-23.4	-539	398
3	18.7	18.6	-1000	-1000
4	17.1	38.1	-551	-1000
5	203.0	201.8	157	-115
6	31.7	33.4	-1000	-1000
7	9.6	9.9	-771	-774
8	22.0	22.8	-1000	-1000
9	177.2	184.2	1000	795
10	26.6	28.3	-977	-933
11	10.6	8.0	-773	-238
12	0.0	10.0	-559	-771

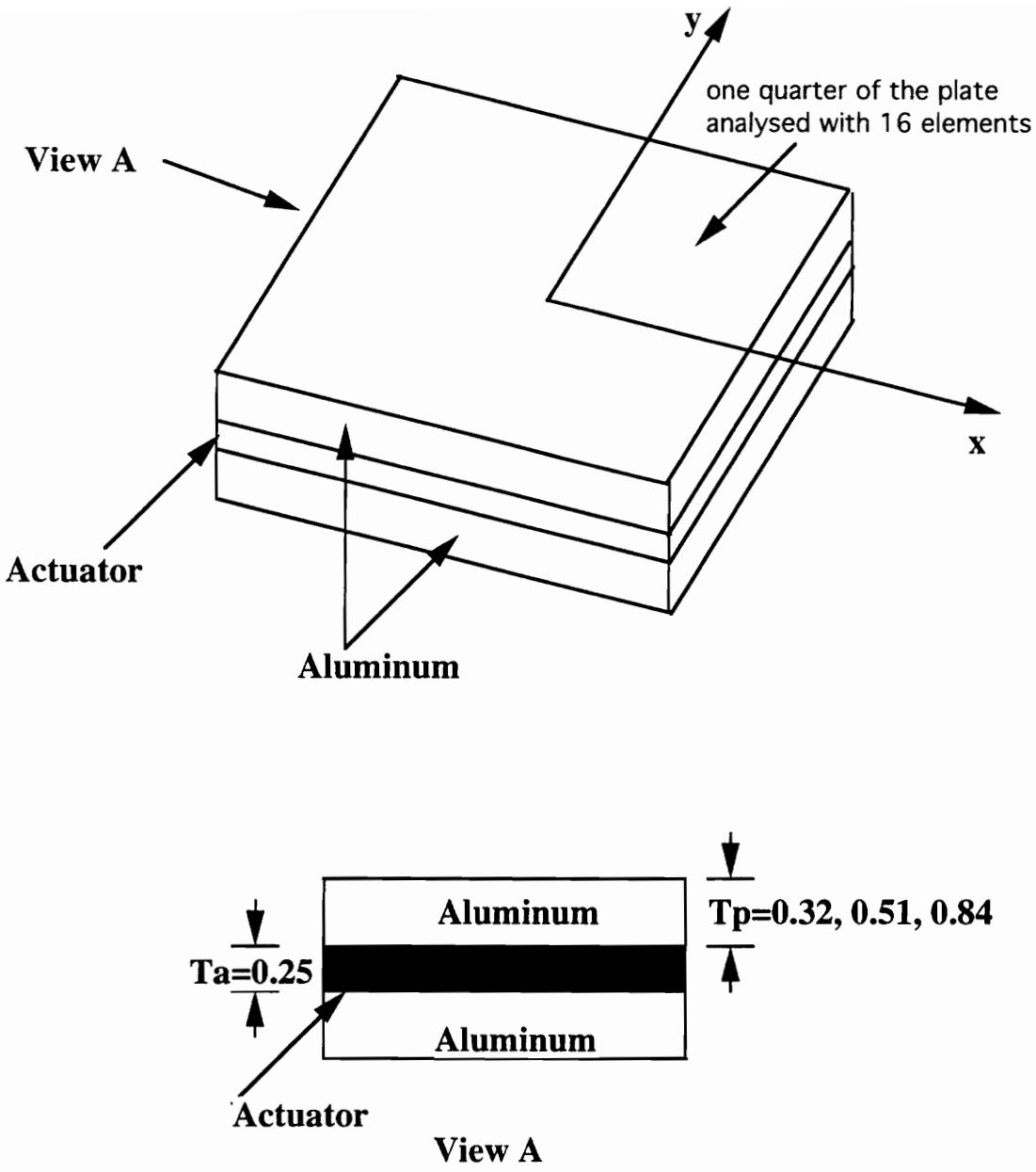

Figure 4.1 : EAL validation model for strain prediction

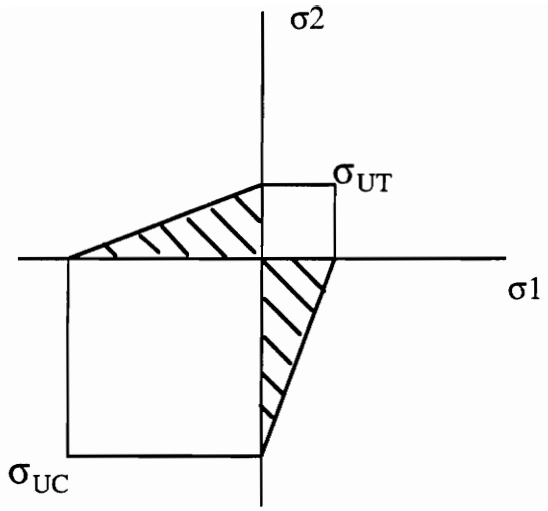

Figure 4.2 : Simplified Mohr's failure criterion for brittle material

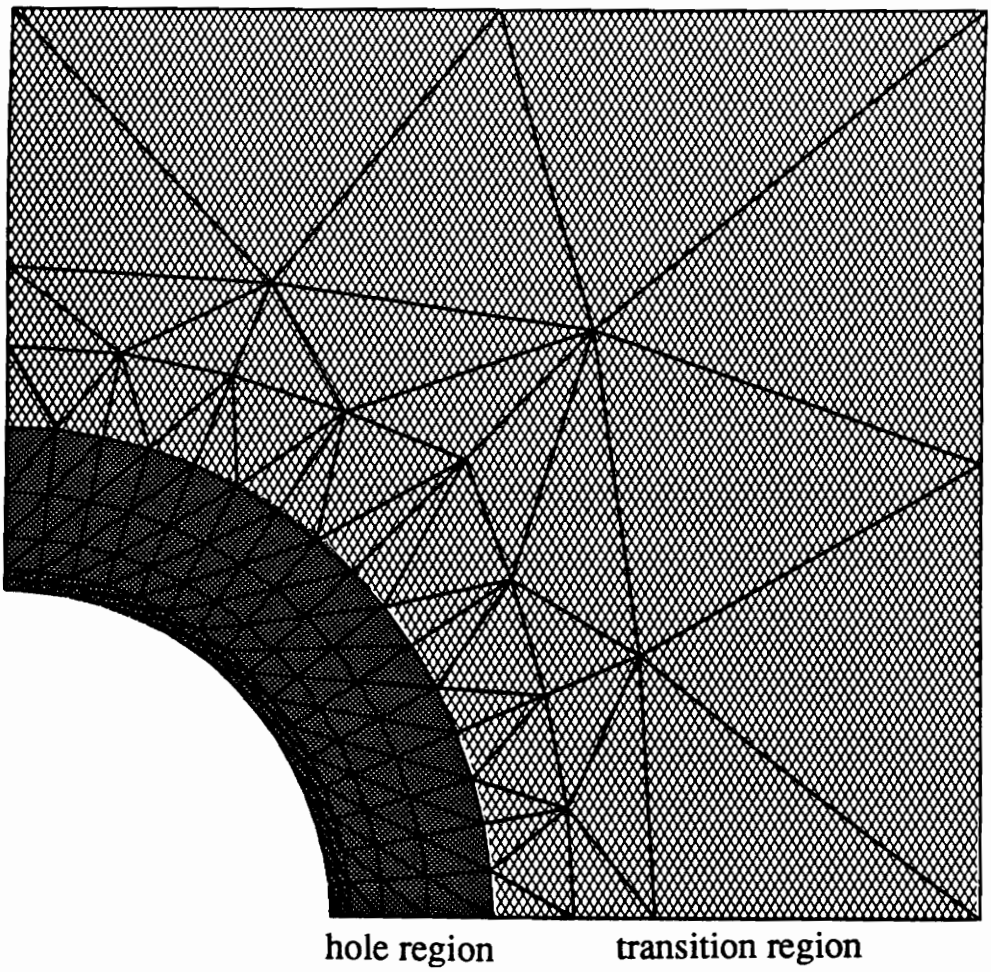

Figure 4.3 : Finite element mesh showing actuator locations in the hole region

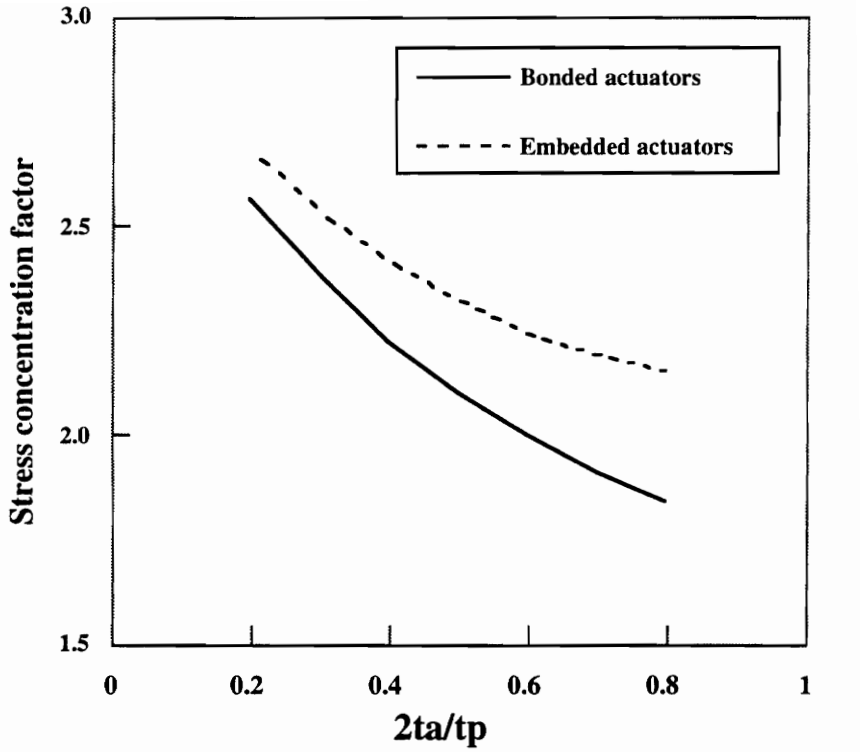

Figure 4.4 : Variation of SCF with actuator thickness for bonded and embedded actuators for Von-Mises criterion (with only induced strain constraint of 1000 με)

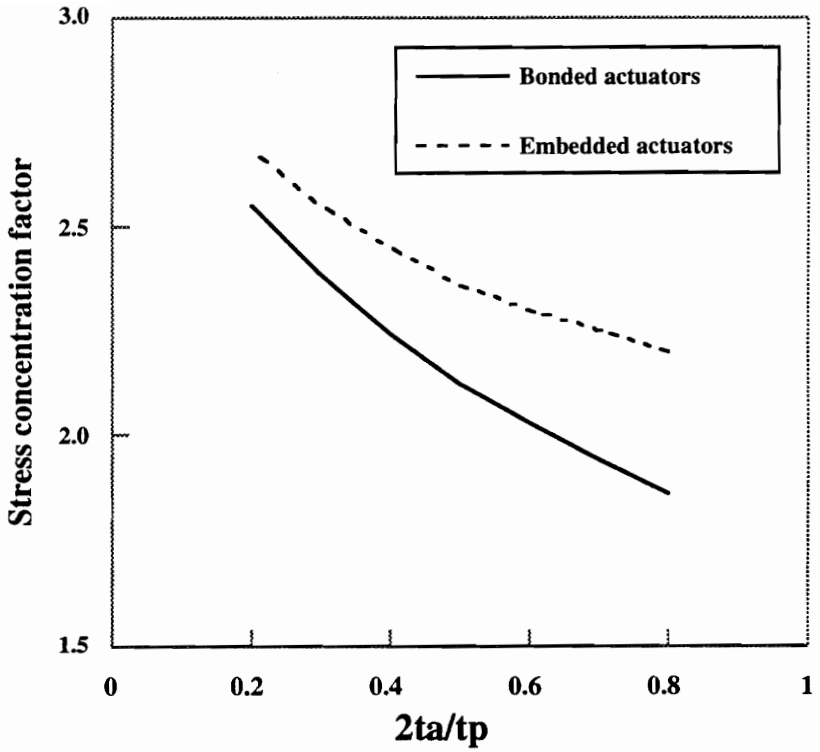

Figure 4.5 : Variation of SCF with actuator thickness for bonded and embedded actuators for max. shear criterion (with only induced strain constraint of 1000 με)

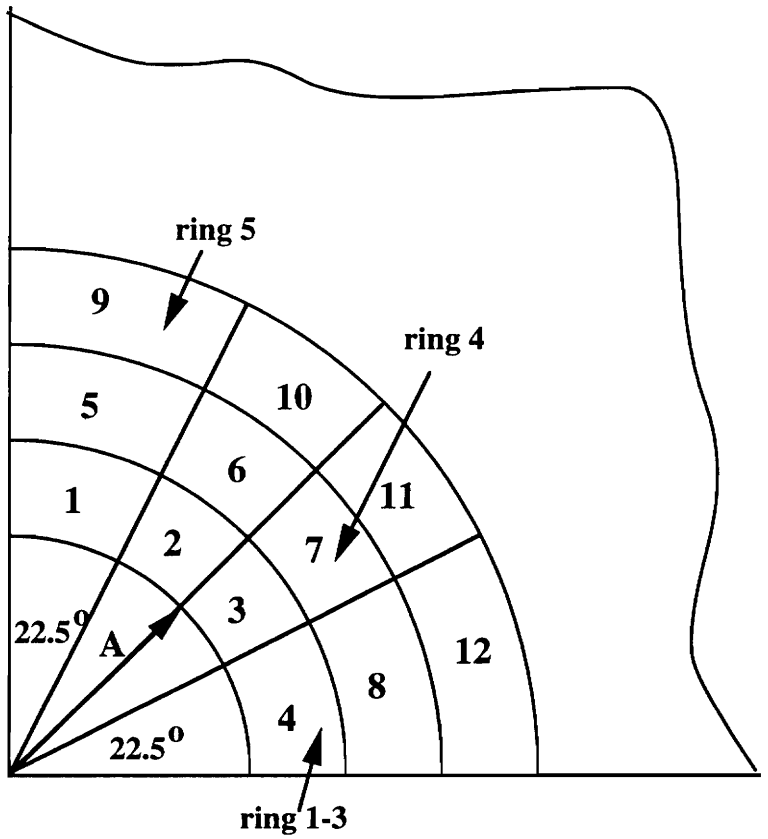

Figure 4.6 : Quarter plate with a hole showing actuator locations for twelve variable case

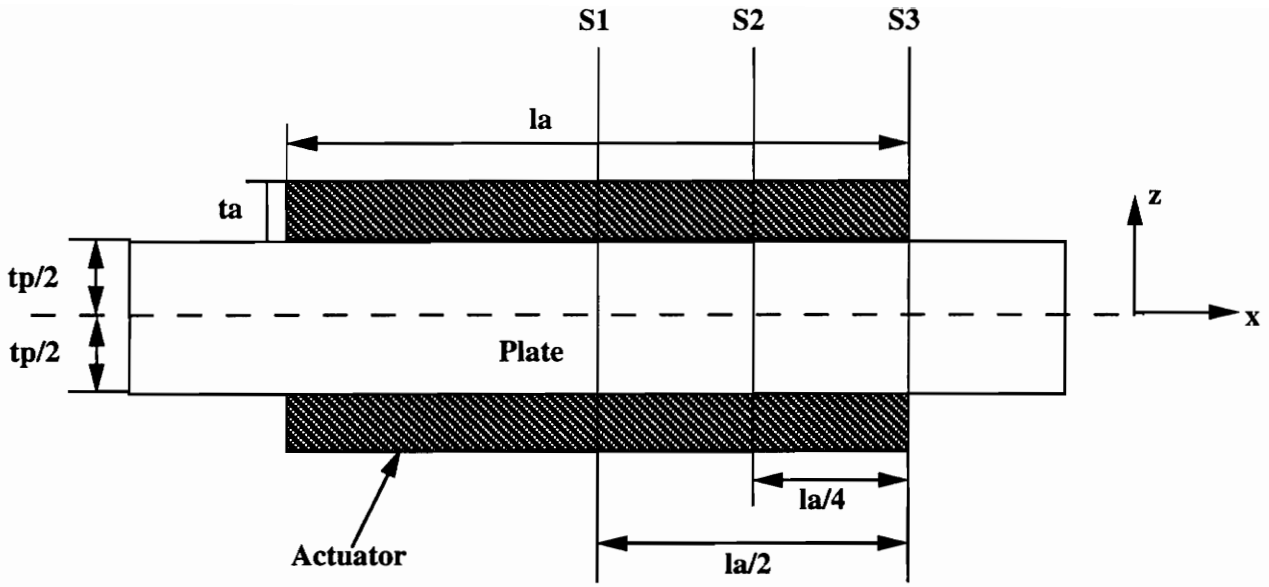

Figure 4.7 : Bonded actuators showing locations of stations used for plotting stresses

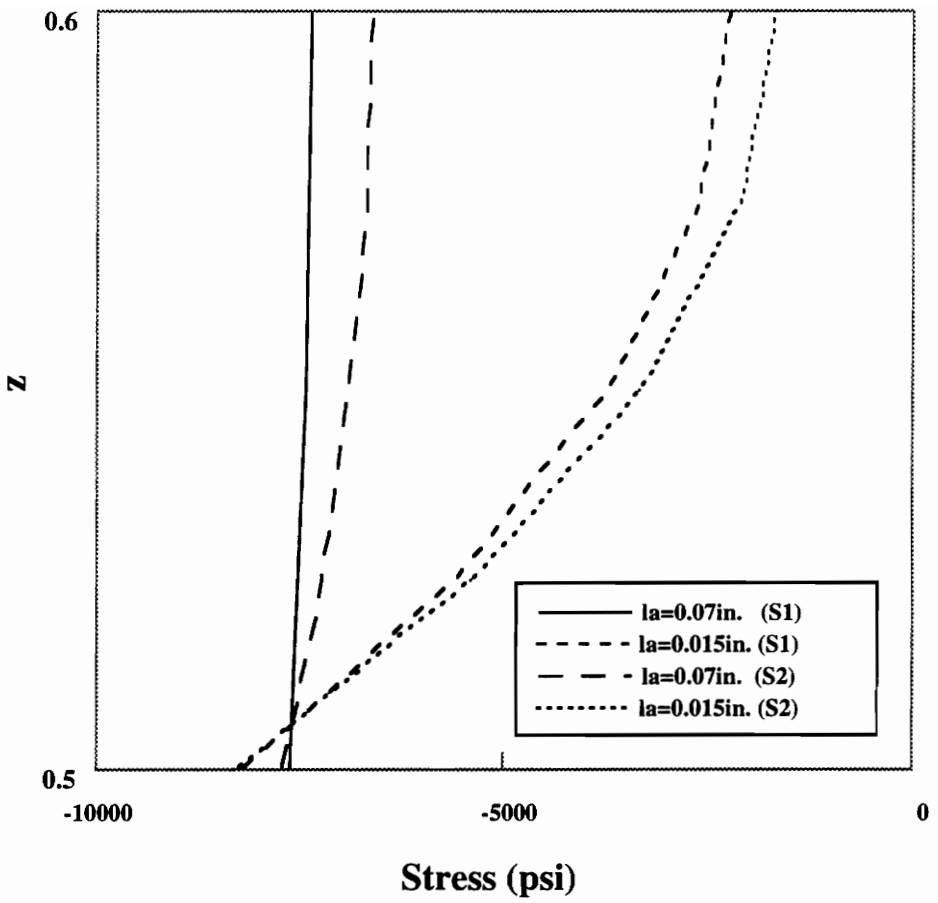

Figure 4.8 : Variation through the thickness of axial stresses for long and short actuators at station S1 and S2 of Fig. 4.7 (2ta/tp = 0.2), actuator-plate interface at z=0.5

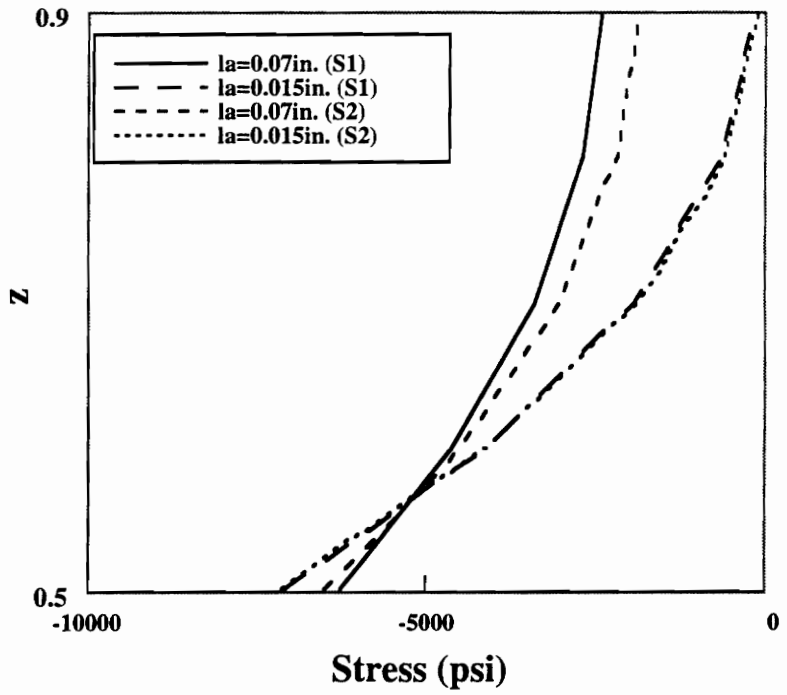

Figure 4.9 : Variation through the thickness of axial stresses for long and short actuators at stations S1 and S2 of Fig. 4.7 (2ta/tp = 0.8), actuator-plate interface at z=0.5

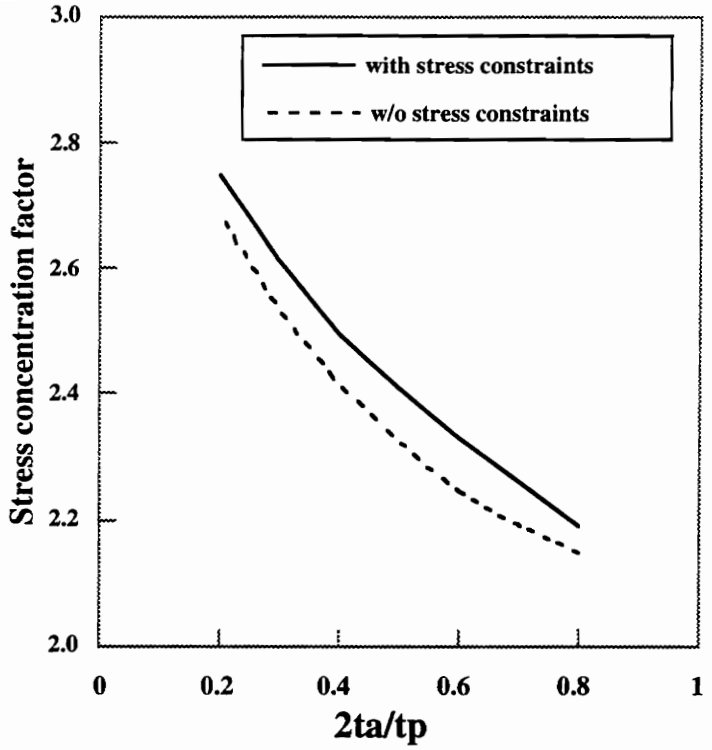

Figure 4.10 : Variation of Von-Mises based SCF with actuator thickness for embedded actuators with and without constraints on actuator stresses

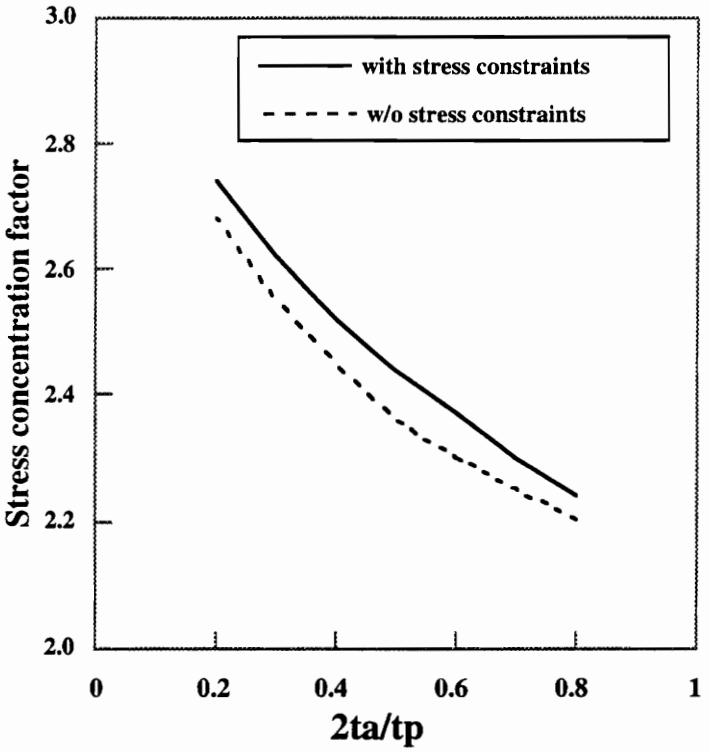

Figure 4.11 : Variation of max. shear stress based SCF with actuator thickness for embedded actuators with and without constraints on actuator stresses

CHAPTER 5

STRESS REDUCTION USING REALISTIC LIMITS ON ACTUATORS - EXTREME LOAD CASE (NON-AXISYMMETRIC ACTUATION)

5.1 INTRODUCTION

In this chapter, similar to Chapter 4, we investigate the effects of present technology limitations on piezoelectric actuators on the potential reductions in stress concentrations for an extreme load case with stresses selected from material allowables. Numerical optimization based on finite element simulations was used to obtain applied induced strain distributions in an isotropic plate with a hole. We applied uniform compression of S=-25 ksi. This corresponds to a limit of 75 ksi for aluminum without active stress alleviation. A genetic algorithm was also used for this load case to search for more effective actuator locations than those obtained with the continuous optimization. The rest of the problem is same as discussed in sections 4.2 and 4.5 with the only difference that prestressing could not be used for the extreme load case.

5.2 NON-AXISYMMETRIC PARTIAL THICKNESS ACTUATION

As discussed before, in this case the applied loading was increased from -10 ksi to -25 ksi. This will produce compressive tangential stresses of -75 ksi at $\theta = 90^{\circ}$ and tensile tangential stresses of 25 ksi at $\theta = 0^{\circ}$, at the edge of the hole. When actuators were placed only in the hole region (i.e., $A \leq r \leq 1.5A$), with constraints on actuation strains and actuator stresses, SCFs based on Von-Mises criterion for $2t_a/t_p = 0.2$ were

reduced to 2.83 and 2.97 with bonded and embedded actuators, respectively. Actuators were then placed both in the hole region as well as outside the hole region, which we designate as transition region, (Figure 5.1), to obtain larger reduction in the SCFs. These additional actuators placed over a larger area also represent larger passive effects and the distribition of material could possibly be optimized to reduce the SCFs (without any actuation strains). It may be possible to obtain larger reduction in SCF by such passive structural optimization than that obtained with applied actuation strains. However, we have not compared the active reduction obtained in this analysis with the possible reduction in SCF with better placement of actuators. Actuators were not placed near the hole around $\theta = 0^o$ due to high tensile tangential stresses in that area.

In this load case, due to high applied loading (S = -25 ksi) the stresses in the actuators were large and prestressing them did not have any positive effect. All the subsequent results, discussed in this section, are without prestressing and with constraints on actuation strains and actuator stresses. The variation of SCF with actuator thickness are shown in Figure 5.2 for bonded and embedded actuators, for Von-Mises stress criterion. We can see that large reductions in SCF can be obtained. For $2t_a/t_p = 0.8$, SCF were reduced from 3 to 1.72 and 2.19 for bonded and embedded actuators, respectively. Figure 5.3 shows the variation of of SCF based on maximum shear stress criterion for this case.

For this load case also we wanted to see how the technological limits, i.e., limitation on the maximum actuation strains and actuator stresses, influence the performance of piezoelectric actuators. To see that we found SCF for four different cases;

a) with no constraints on applied induced strains and actuator stresses,

b) constraints on actuator stresses only,

c) constraints on actuation strains only,

d) constraints on both applied induced strains and actuator stresses.

Results for Von-Mises stress criterion are shown in Figure 5.4 and Figure 5.5 for bonded and embedded actuators, respectively. Figure 5.6 and Figure 5.7 show the corresponding SCF based on the maximum shear stress criterion. We can see that both constraints have significant affect on the reduction of SCF. Without any constraints, the SCF based on Von-Mises stress criterion could be reduced from 3 to 1.08 and 1.47 for the bonded and embedded actuators, respectively. We can also see from the figures that the constraint of limited applied induced strain has larger effect than the constraint on actuator stresses, in particular for thick actuators. For example, with embedded actuators for $2t_a/t_p = 0.4$ (Figure 5.5), the SCF for Von-Mises stress criterion could be reduced to 2.0 with only the actuator stress constraint, compared to 2.72 when both constraints were applied. However, when only the maximum applied induced strain constraint was applied, the SCF was reduced to 2.54.

5.3 ACTUATOR PLACEMENT USING GENETIC ALGORITHMS

It was found that actuators placed close to the hole have large stresses due to applied mechanical loading, and this may restrict the effectiveness of piezoelectric actuators. We wanted to see whether there are other possible areas away from the hole where actuator placement would be more effective. We used Genetic Algorithm (GA) to search for such actuator locations, if any, tha would give us larger reduction in SCF compared to that obtained using continuous optimization. With a GA we can also prescribe the maximum area (A_{act}^{max}) used by the actuators. When actuator area exceeds A_{max}, the objective

function can be penalized depending on the extent of violation. This process eliminates such design in the subsequent generations.

5.3.1 GENETIC ALGORITHMS

Genetic algorithms mimic biological evolution using Darwin's principle of survival of the fittest. When a population of biological creatures is allowed to evolve over generations, individual characteristics that are useful for survival tend to be passed on to future generations, because individuals carrying them get more chances to breed. These characteristics in biological populations are stored in chromosomal strings. The mechanics of natural genetics is based on operations that result in structured yet randomized exchange of genetic information (i.e., useful traits) between the chromosomal strings of the reproducing parents, and consists of *reproduction*, *crossover*, and occasional *mutation* of the chromosomal strings.

Genetic algorithms, developed by Holland [63], simulate the mechanics of natural genetics for artificial systems based on operations which are the counterparts of the natural ones (even called by the same names). Application of the operators of genetic algorithms to a search problem first requires the representation of the possible combinations of the variables in terms of bit strings that are counterparts of the chromosomes. Naturally, the measure of goodness of a specific combination of genes is represented in an artificial system by the objective function and constraints of the search problem.

Because of the bit string representation of the variables, genetic algorithms are ideally suited for problems where the variables are required to take discrete or integer variables. Often we can represent the design by several forms of coding. For the problem of placing actuators at n possible locations we can have a string of n bits with ones representing

occupied locations and zeroes representing unoccupied locations. If we have m actuators to place, another possible representation is a string of m numbers each varying from 1 to n that indicate at which locations peripherals are placed.

Unlike most search algorithms which move from one point to another in the design variable space, genetic algorithms work with a population of strings (designs). This aspect of genetic algorithms is responsible for capturing near global solutions, by keeping many solution points that may have the potential of being close to minima (local or global) in the pool during the search process rather than singling out a point early in the process and running the risk of getting stuck at a local minimum. Like other random search algorithms, GAs occasionally accept new designs that are poorer from the previous design. This gives GA the capability of escaping from local minima. Also, the outcome of a genetic search is a population of good designs rather than a single design. This aspect can be very useful to the designer.

Most genetic algorithms work with a population of fixed size and the initial population of designs is generated randomly. The key step in the process is *reproduction*, in which individual designs with good objective function values are selected as parents for a new generation of designs. The bias towards designs with better performance is achieved by increasing the probability of their selection in relation to the rest of the population. This is often done by simulating a biased roulette wheel where individual strings occupy areas proportional to their objective function values.

Next, the parents selected are paired off for crossover. The mating of the pair also involves a random process. A random integer k between 1 and $L-1$, where L is the string length, is selected and two new strings are generated by exchanging the numbers that come after the kth location in the first parent with the corresponding locations of

the second parent. For example, the two strings of length $L = 9$

$$\begin{array}{ll} \textbf{parent 1:} & 0\ 1\ 1\ 0\ 1 \| 0\ 1\ 1\ 1 \\ \textbf{parent 2:} & 0\ 1\ 0\ 0\ 1 \| 0\ 0\ 0\ 1 \end{array},$$

are mated with a crossover point of $k = 5$, the two possible offsprings will have the following composition,

$$\begin{array}{ll} \textbf{offspring 1:} & 0\ 1\ 1\ 0\ 1\ 0\ 0\ 0\ 1 \\ \textbf{offspring 2:} & 0\ 1\ 0\ 0\ 1\ 0\ 1\ 1\ 1 \end{array}.$$

Mutation serves an important task of preventing premature loss of important genetic information by occasional introduction of random alterations of a design. The reproduction process tends to favor the design characteristics of the best individuals in the original population. Good characteristics of the poorer designs can be lost. For example, if a particular location which corresponds to the optimum designs was present in the original population only in a design that was otherwise poor, it can be lost if this design is not selected as a parent. Mutation prevents this difficulty, and is implemented by randomly changing some bits in the design string.

In order to implement a genetic algorithm for our problem, we first need to define a string representation for the location of the actuators and applied induced strains in those actuators. Initially, 31 possible actuator locations were selected as shown in Figure 5.8. The existence of an actuator at a given location and the value of the applied induced strain in that actuator were coded as a 9 bit binary number. The first bit indicates the presence (1) or absence (0) of an actuator. The remaining 8 bits are used to indicate the applied induced strains, if the actuator is present, which varies from $-1000\mu\epsilon$ (X_u) to $1000\mu\epsilon$ (X_l). Since the applied induced strain is a continuous design variable, coding of this as binary number depends on the desired presicion X_{pre} which was taken as

$10\mu\epsilon$. The string length m for the applied induced strain was then calculated from the expression

$$2^m \geq \frac{(X_u - X_l)}{X_{pre}} + 1 \ , \tag{5.1}$$

where the continuous design variable X lies within the domain $X_l \leq X \leq X_u$ with precision X_{pre}. From this expression we get $m = 8$ and this actually gives a precision of $8\mu\epsilon$. 31 such substrings representing the 31 actuator locations are put together to form a "chromosome" for the genetic search. This $9x31$ bit chromosome completely defines the locations of the actuators along with the applied induced strains in those actuators.

The genetic algorithm works on a population of n_d designs. It will search for an optimal design (maximize or minimize an objective function) by going from one generation to the next using selection, crossover and mutation. The present implementation employs elitist strategy where the best design of every generation is always copied into the next generation. This guarantees that the best design will never be lost from one generation to the next. The convergence test used in this study stops the search when the best design does not improve after a specified number of generations (n_{cgen}). The search is also stopped if the number of generations exceed n_{gen}. In summary, the genetic algorithm used in this study is :

1. Create an initial population of n_d individuals at random.
2. Rank the individuals according to the value of the objective function.
3. Copy the best design into the new generation.
4. Apply a linear roulette wheel selection rule to pick two parents: the probability of selection of an individual for breeding is proportional to n_d minus its rank in the population.

5. Create one offspring by applying a two-point crossover to the parents (two cut points are selected at random and the substrings between these cuts are exchanged between the parents and the probability of crossover is denoted as p_c).

6. Perform some random mutations in the offspring chromosome (the probability for any given gene (bit) in the chromosome to mutate is denoted p_m)

7. Add the new design in the new population. If the number of individuals in the new population is less than n_d, the new generation is not complete, go to step 4.

8. Check for convergence. If the number of generation without improvement is more than n_{cgen}, go to step 10.

9. If generation number is less than n_{gen} go to step 2.

10. Select the best design in the current population and stop.

The optimization problem was formulated as

$$\begin{aligned} &minimize && \sigma_{max} \\ &such\ that && \sigma_a^M(\epsilon_k^i) \leq \sigma_a^{max} \\ & && A_{act} \leq A_{act}^{max} . \end{aligned} \tag{5.2}$$

As before, the design variables were the values of applied induced strains ϵ_k^i , k=1,...,n in n regions of the plate. σ_{max} is the maximum equivalent stress based on Von-Mises stress or maximum shear stress criterion and constraints were placed on maximum actuator stresses (based on simplified Mohr's criterion) and the maximum available actuator area. σ_a^M are the stresses in actuators, and σ_a^{max} are the allowable stresses in actuators according to the Mohr's criterion (Figure 3.3). A_{act} is total area over which actuators are placed and A_{act}^{max} is the maximum available actuator area.

The constraints in the optimization problem were transformed into a penalty parameter , P^n , which was used in the genetic algorithm. The penalty parameter P^n was defined as

$$P^n = (P_A \; P_\sigma)^n \; , \tag{5.3}$$

where P_A is the penalty due to violation of maximum available actuator area constraint and defined as

$$P_A = \begin{cases} \frac{A_{act}}{A_{act}^{max}}, & \text{if } \frac{A_{act}}{A_{act}^{max}} > 1; \\ 1, & \text{otherwise} \end{cases} \; . \tag{5.4}$$

Similarly, P_σ is the penalty due to actuator stress violation and calculated as

$$P_\sigma = \begin{cases} max(\frac{\sigma_a^M}{\sigma_a^{max}}), & \text{if } \frac{\sigma_a^M}{\sigma_a^{max}} > 1; \\ 1, & \text{otherwise} \end{cases} \; . \tag{5.5}$$

Starting value of n was taken as 0.5 so that initially we do not penalize a design too much due to constraint violations because bad designs may also have some good traits. The value of n was incremented by 0.1 every generation to a maximum value of 2.0.

The optimization problem was then formulated as

$$minimize \quad P^n \; \sigma_{max} \; . \tag{5.6}$$

The parameters of the algorithms were set to n_d = 100, n_{gen} = 300, n_{cgen} = 50, p_c = 0.95, p_m = 0.01.

Optimizations were carried out for the load case II (i.e., S = -25 ksi) and for normalized actuator thickness $2t_a/t_p$ = 0.2. We did not consider any prestressing and constraints were applied to applied induced strains, actuator stresses and available actuator area. Available area for actuator placement was varied from 2.0 sq. in. to 22.0 sq. in. Passive stress distribution (without activating the actuators) will depend on the actuator locations. Since these actuator locations can only be found after the optimization is done, we neglected the passive effect in the optimization. After optimization

for the active stress reduction, exact analysis was performed with actuator location and applied induced strains obtained from GA to include the passive effect. Results are shown in Figure 5.9 along with the active reduction and we can see that the variation of SCF with available actuator area is not smooth, i.e., SCF does not always decrease with increase in available actuator area. This happens because the passive stress distribution due to added actuator stiffness was neglected during optimization and due to that the actuators are not placed effeciently over the plate.

Figure 5.10 and Figure 5.11 show the actuator locations obtained from GA when available area was limited to 5.0 sq. in. and 7.5 sq. in., respectively. We can see that when we increase the available actuator area from 5.0 to 7.5 sq. in., one additional actuator is placed at the location 17 (Figure 5.11). Passive SCF (without the active reduction) for these two cases were obtained as 2.49 for available actuator area of 5.0 sq. in. compared to 2.57 for the available actuator area of 7.5 sq. in.. It can be seen that the additional actuator at location 17 adversely affects the stress distribution in the region where stress concentration is large i.e., at $\theta = 90^0$. From these results, we can see that the passive stress distribution due to actuator placement is important and if possible, should be included for optimum placement of actuators. However, the purpose of this study, as mentioned earlier, was to find actuator locations away from the hole so that the stresses in actuators are well below the allowable limits so that the actuators are more effective in reducing SCFs compared to that obtained with continuous optimization. But as we can see from Figures 5.10 and 5.11 that the actuators were placed near the hole.

Next, we decided to place the actuators away from the hole and 19 possible actuator locations were selected as shown in Figure 5.12. Optimizations were then carried out (neglecting the passive effect) for three actuator thicknesses ($2t_a/t_p = 0.2, 0.6, 1.0$) and

three different available actuator areas (11.0, 22.0, and 33.0 sq. inch). Reductions in SCF for these cases along with that obtained from continuous optimizations are shown in Table 5.1. It can be seen from the table that as we increase the area over which actuators are placed, the rate of reduction in SCF drops. For $2t_a/t_p = 1.0$, when actuator area was increased from 11 sq. in. to 22 sq. in., the reduction in SCF increased by 4.9 percent compared to 2.1 percent, which was obtained when actuator area was increased from 22 sq. in. to 33 sq. in. We can also see that the reduction in SCF obtained with GA is not significantly different from that obtained with continuous optimization. For 2Ta/Tp = 0.2, the actuator locations obtained with GA for available areas 11.0, 22.0 and 33.0 sq. inch are shown in Figures 5.13, 5.14, and 5.15, respectively. Figures 5.16, 5.17, and 5.18 show the corresponding actuation locations for $2t_a/t_p = 1.0$, respectively. In this case also, exact analysis was performed to include the passive effect due to actuator stiffness using the actuator locations and applied induced strains obtained from the GA. Results are given in the Table 5.2. If the actuators are placed efficiently over the plate, we should be able to get significant reduction in the SCF without even activating the actuators. Since the passive effect was neglected during the optimization, as can be seen from Table 5.1, including this passive effect after optimization has little influence on the reduction in SCF.

5.4 COMPARISON OF PASSIVE AND ACTIVE STRESS REDUCTION

We also investigated the cost of passive reduction in stress concentration factor. Passive reduction (without activating the actuators) in stress concentration factors were calculated by placing actuators over the hole region (i.e., $A \leq r \leq 1.5A$, where A is the radius of the hole) for actuator thicknesses $2t_a = 0.01$ to 0.1 inch. Active reductions were

calculated using three different piezoelectric materials: i) with the present technology limitations, i.e., free induced strain of 1000 $\mu\epsilon$ and compressive-tensile strength 75-9 ksi, ii) free induced strain of 1000 $\mu\epsilon$ and compressive-tensile strength of 75-15 ksi, and iii) free induced strain of 2000 $\mu\epsilon$ and compressive-tensile strength of 75-20 ksi. Although the piezolelctric material listed under ii) and iii) are not presently available, we wanted to see the effect of doubling free strain (2000 $\mu\epsilon$) and improving tensile behavior of actuator on stress reduction. Area over which bonded actuators were placed was varied from 0.24 sq. in. to 0.82 sq. in. and two actuator thicknesses, $2t_a/t_p = 0.4$ and 0.8 were considered. Reduction in SCF for all these cases are shown in the Figure 3.35 along with the passive reduction.

Seven cases, shown in Figure 3.35 are summarized below:

1. Passive reduction with added thickness in the hole region
2. Active and passive reduction for $2t_a/t_p = 0.4$, free induced strain=1000 $\mu\epsilon$, compressive-tensile strength of 75-9 ksi.
3. Active and passive reduction for $2t_a/t_p = 0.4$, free induced strain=1000 $\mu\epsilon$, compressive-tensile strength of 75-15 ksi.
4. Active and passive reduction for $2t_a/t_p = 0.4$, free induced strain=1000 $\mu\epsilon$, compressive-tensile strength of 75-20 ksi.
5. Active and passive reduction for $2t_a/t_p = 0.8$, free induced strain=1000 $\mu\epsilon$, compressive-tensile strength of 75-9 ksi.
6. Active and passive reduction for $2t_a/t_p = 0.8$, free induced strain=1000 $\mu\epsilon$, compressive-tensile strength of 75-15 ksi.
7. Active and passive reduction for $2t_a/t_p = 0.8$, free induced strain=1000 $\mu\epsilon$, compressive-tensile strength of 75-20 ksi.

It can be seen that with the present technology limitations, adding thickness in the hole region is more effective in reducing SCF than bonded actuators. However, when free induced strain is increased to 2000 $\mu\epsilon$, actuators placed over a small area are more effective in reducing SCF than passive stiffening.

5.5 SUMMARY

For the extreme load case, reduction obtained in SCF with thin actuators placed in the hole region was small. The actuators were needed to be placed over larger area to obtain large reduction in SCF. Constraint of limited applied induced strain was found to have larger effect on SCF reduction than the constraint on actuator stresses. Also, passive stiffening was found to be more effective in reducing SCF than bonded actuators with present technology limitations.

A genetic algorithm was used to search for more effective actuator locations away from the hole which would give us better reduction in SCF than that obtained using continuous optimization. However, in all cases, actuators were placed in the region of high stress concentration and reduction obtained in SCF using GA was similar to that obtained using continuous optimization.

Table 5.1. Reduction in SCF with Genetic Algorithm and Continuous optimization (without passive effect, with 19 actuators)

2ta/tp	Available Area (using GA)			Cont. Opt.
	11 Sq. in.	22 sq. in.	33 sq. in.	44 sq. in.
0.2	2.86	2.83	2.81	2.67
0.6	2.60	2.52	2.47	2.43
1.0	2.49	2.22	2.16	2.13

Table 5.2. Reduction in SCF with Genetic Algorithm and Continuous optimization (passive effect included after optimization, with 19 actuators)

2ta/tp	Available Area (using GA)			Cont. Opt.
	11 Sq. in.	22 sq. in.	33 sq. in.	44 sq. in.
0.2	2.87	2.79	2.80	2.74
0.6	2.62	2.48	2.35	2.20
1.0	2.37	2.13	1.87	1.70

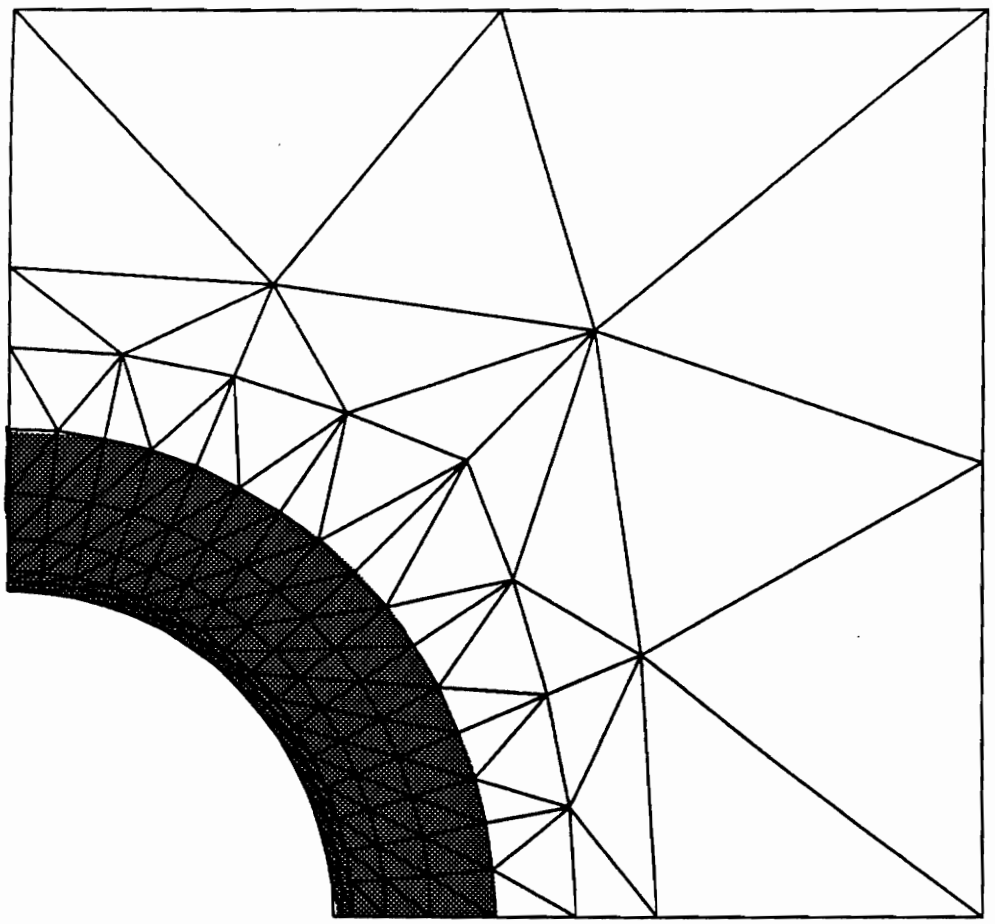

Figure 5.1 : Finite element mesh showing hole and transition regions

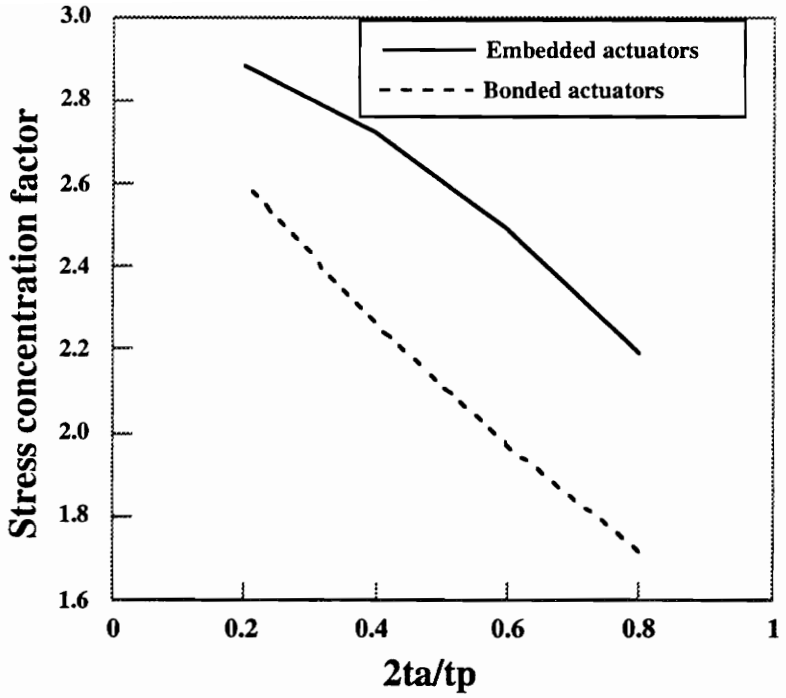

Figure 5.2 : Variation of Von-Mises based SCF with actuator thickness for embedded and bonded actuators, actuators in hole and transition regions , with constraints on actuation strains and actuator stresses

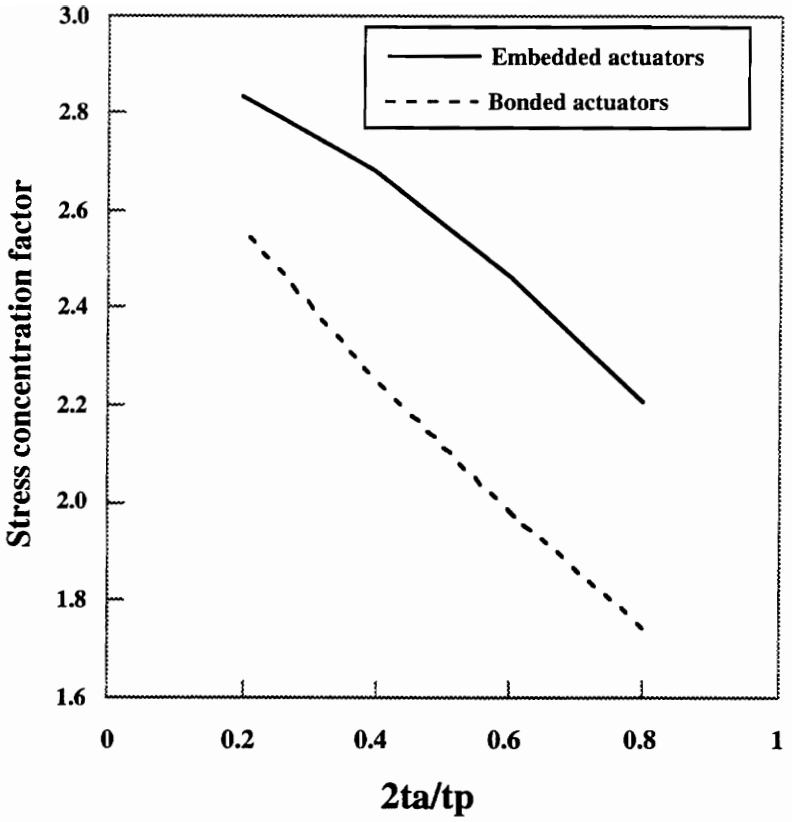

Figure 5.3 : Variation of maximum shear stress based SCF with actuator thickness for embedded and bonded actuators, actuators in hole and transition region with constraints on actuation strains and actuator stresses

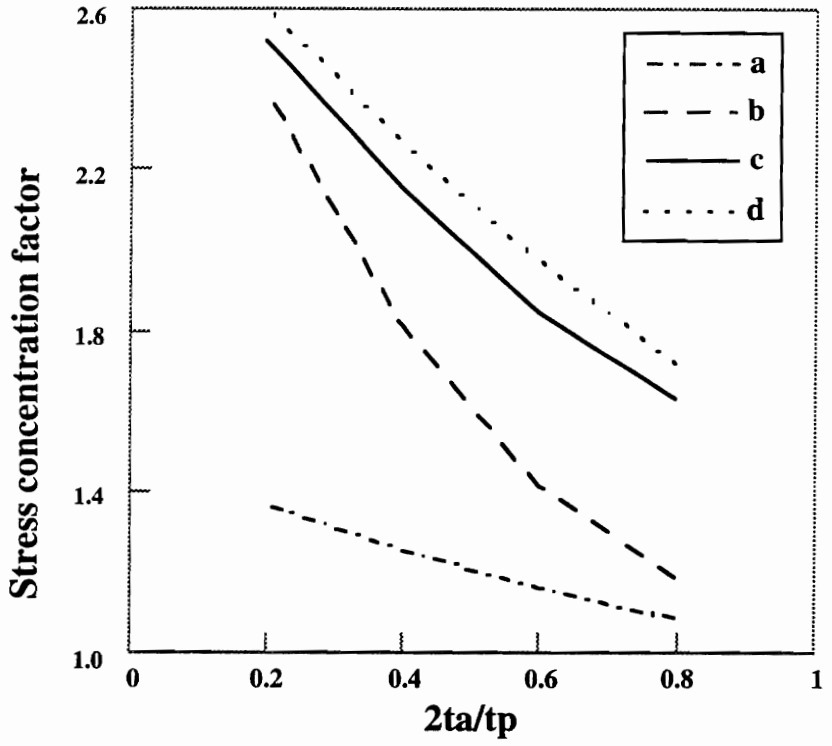

Figure 5.4 : Variation of Von -Mises based SCF with bonded actuator thickness for 4 cases for :
a) no constraints on actuator stresses and strains
b) with constraints on actuator stresses only
c) with constraints on actuation strains only
d) with both constraints

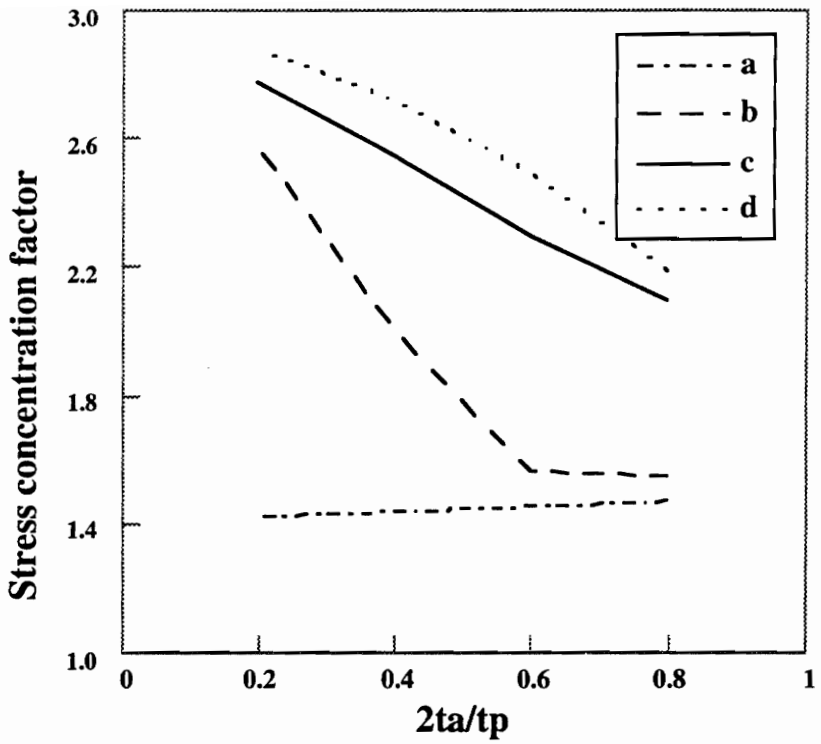

Figure 5.5 : Variation of Von -Mises based SCF with embedded actuator thickness for 4 cases for load :
a) no constraints on actuator stresses and strains
b) with constraints on actuator stresses only
c) with constraints on actuation strains only
d) with both constraints

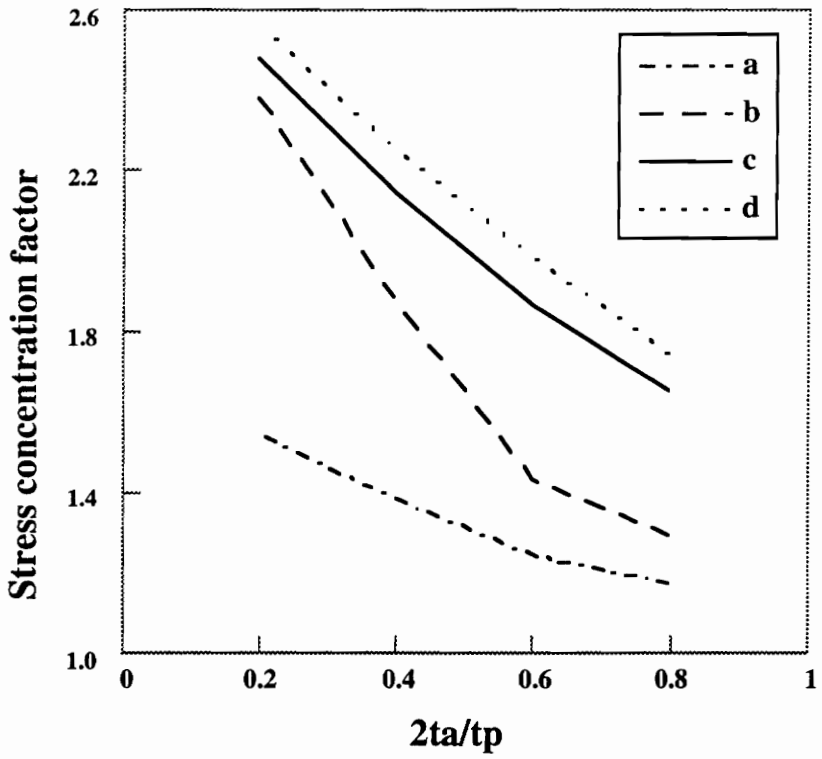

Figure 5.6 : Variation of max. shear stress based SCF with bonded actuator thickness for 4 cases for :
a) no constraints on actuator stresses and strains
b) with constraints on actuator stresses only
c) with constraints on actuation strains only
d) with both constraints

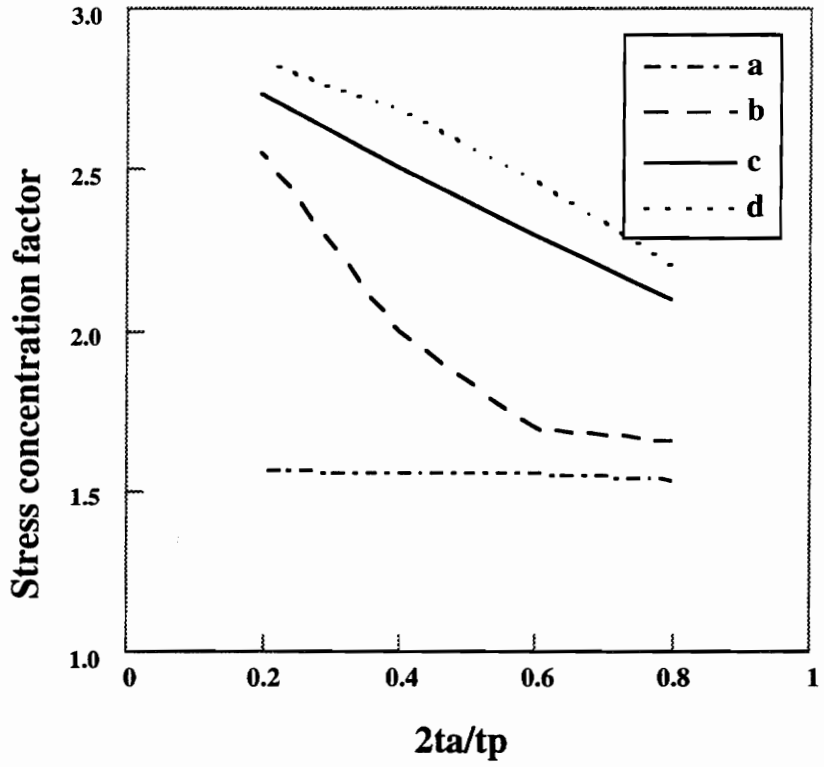

Figure 5.7 : Variation of max. shear stress based SCF with bonded actuator thickness for 4 cases for :
a) no constraints on actuator stresses and strains
b) with constraints on actuator stresses only
c) with constraints on actuation strains only
d) with both constraints

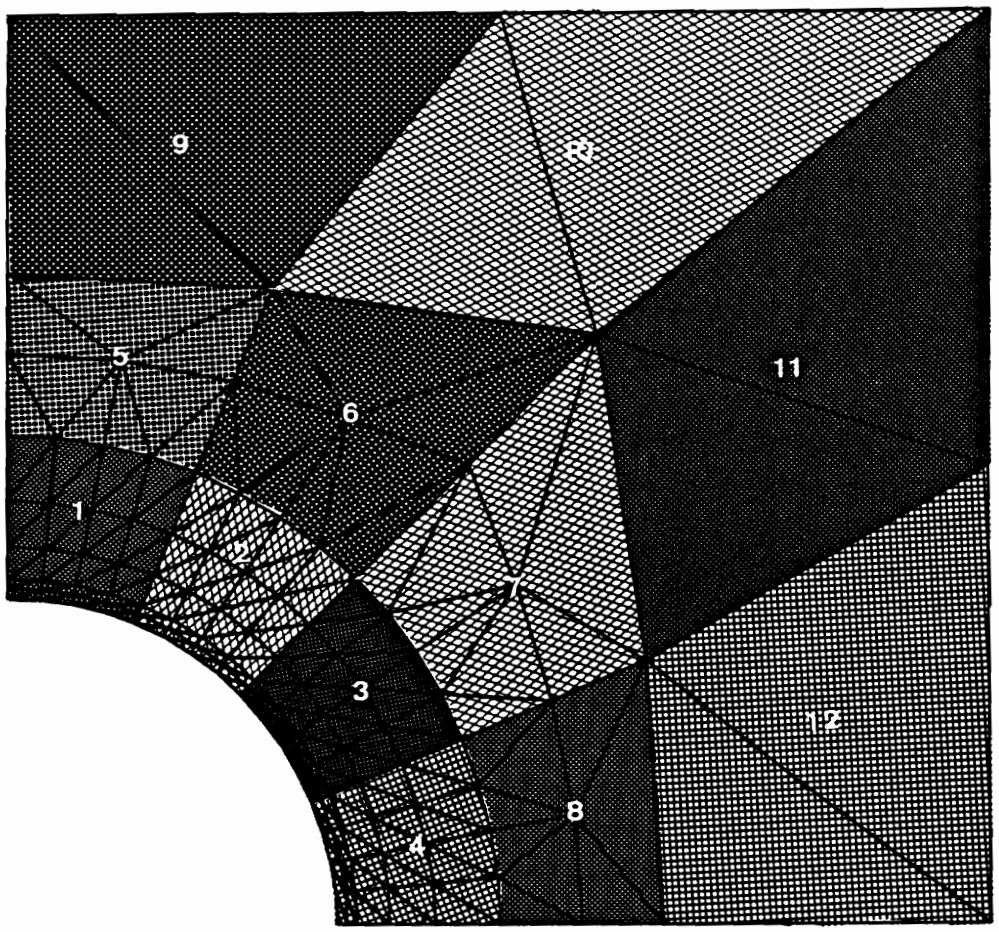

Figure 5.8a : Finite element mesh showing actuator locations in the hole region and transition region (for genetic algorithm)

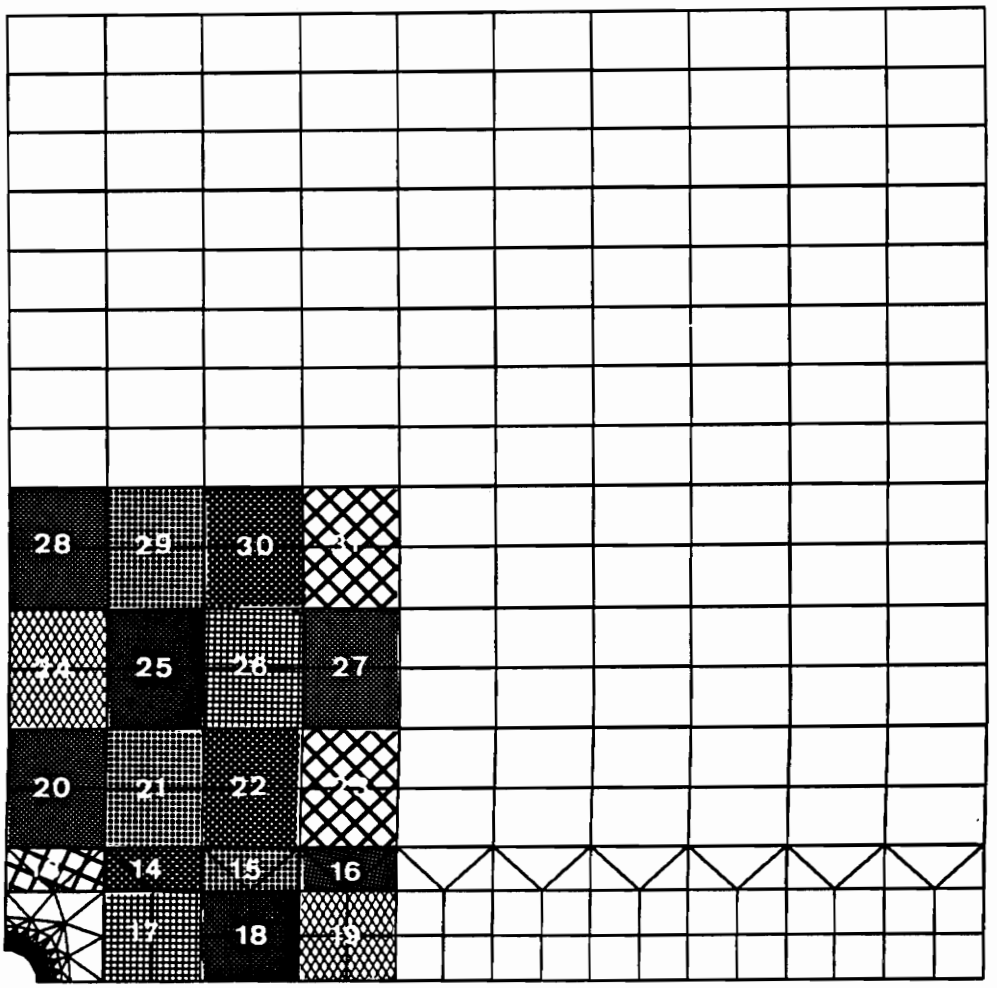

Figure 5.8b : Finite element mesh showing actuator locations away from the transition region (for genetic algorithm)

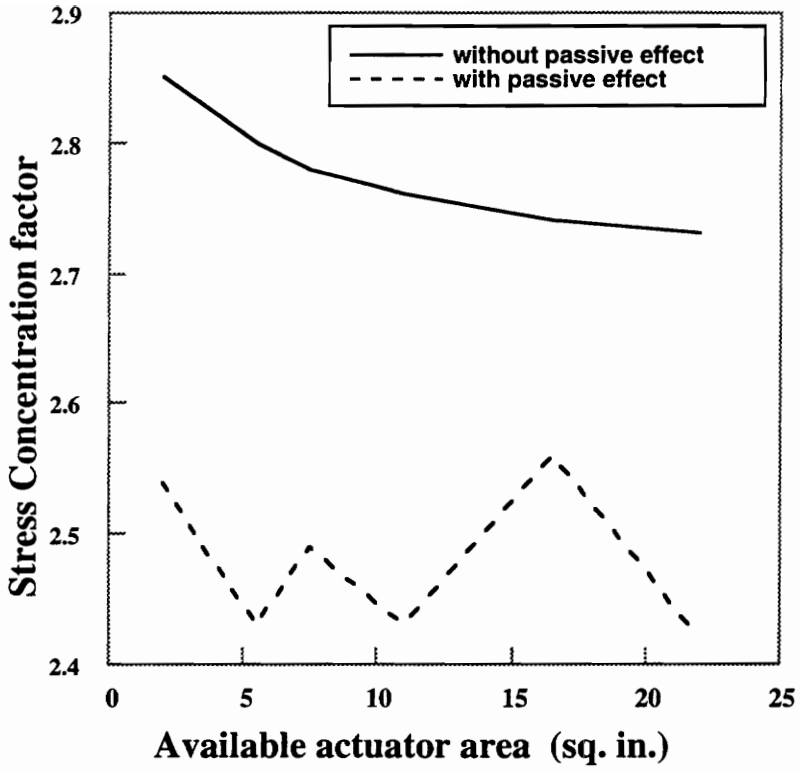

Figure 5.9 : Reduction in SCF with available actuator area with and without passive effect, bonded actuators, (2ta/tp=0.2)

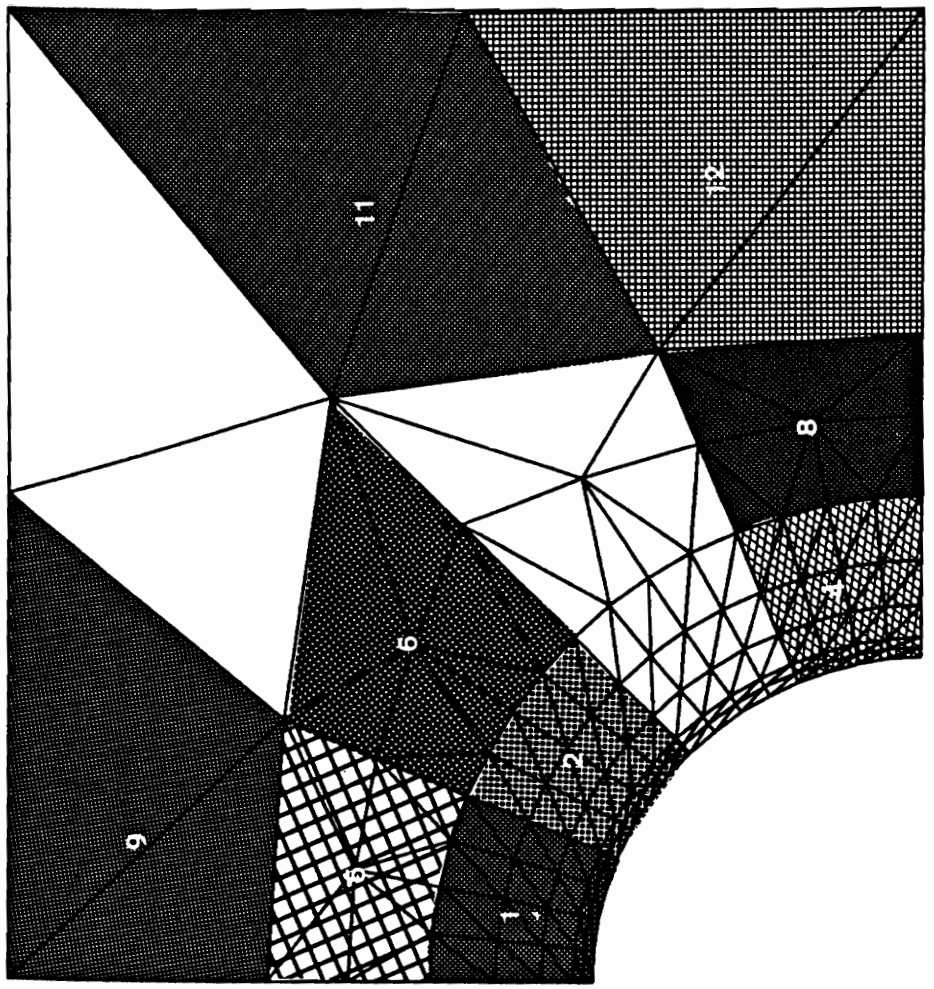

Figure 5.10a : Finite element mesh showing actuator locations in the hole region and transition region when available area limited to 5.0 sq. in. (with 31 actuators)

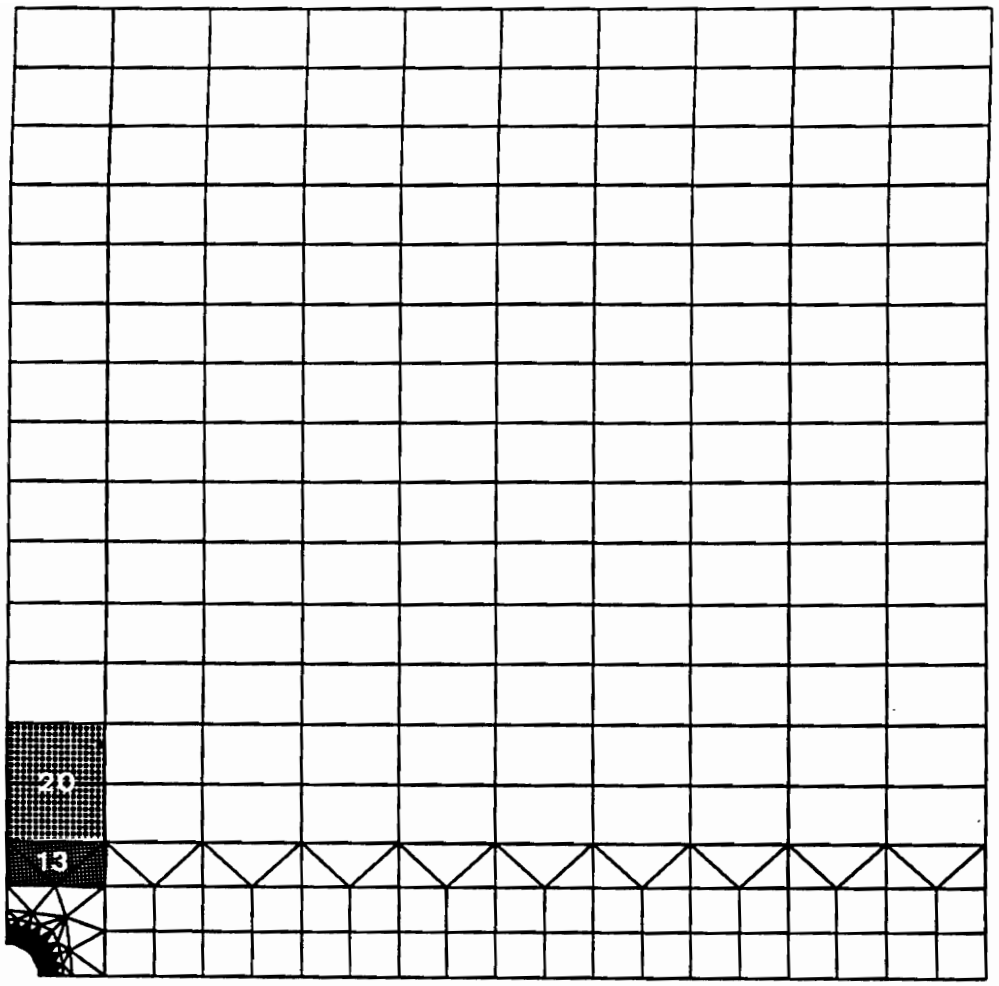

Figure 5.10b : Finite element mesh showing actuator locations away from the transition region when available area limited to 5.0 sq. in. (with 31 actuators)

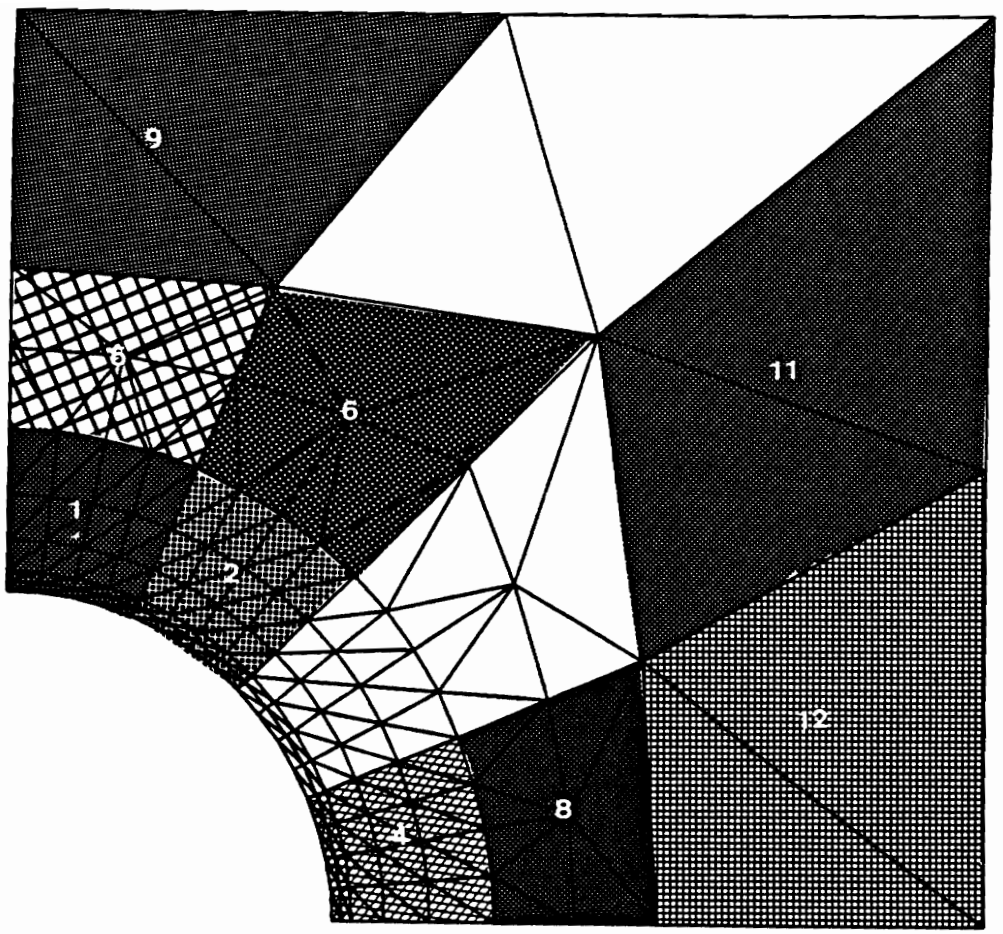

Figure 5.11a : Finite element mesh showing actuator locations in the hole region and transition region when available area limited to 7.5 sq. in. (with 31 actuators)

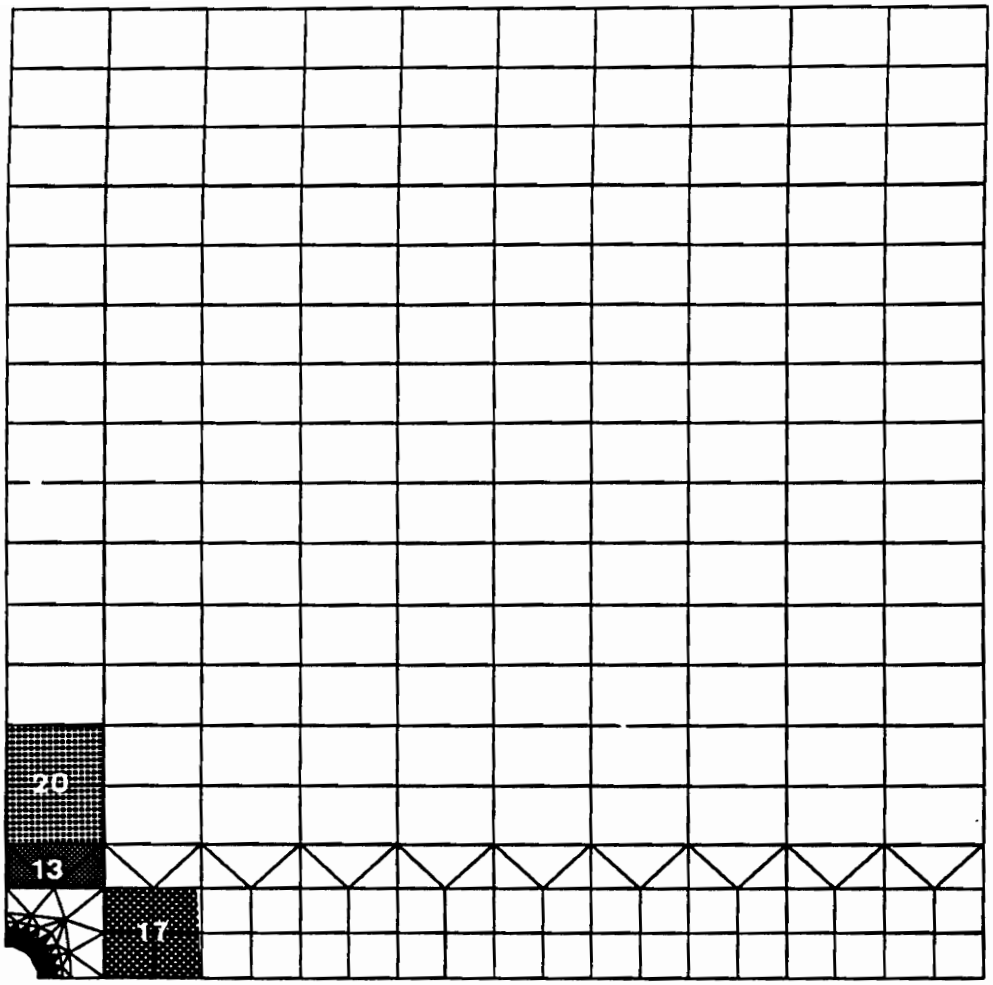

Figure 5.11b : Finite element mesh showing actuator locations away from the transition region when available area limited to 7.5 sq. in. (with 31 actuators)

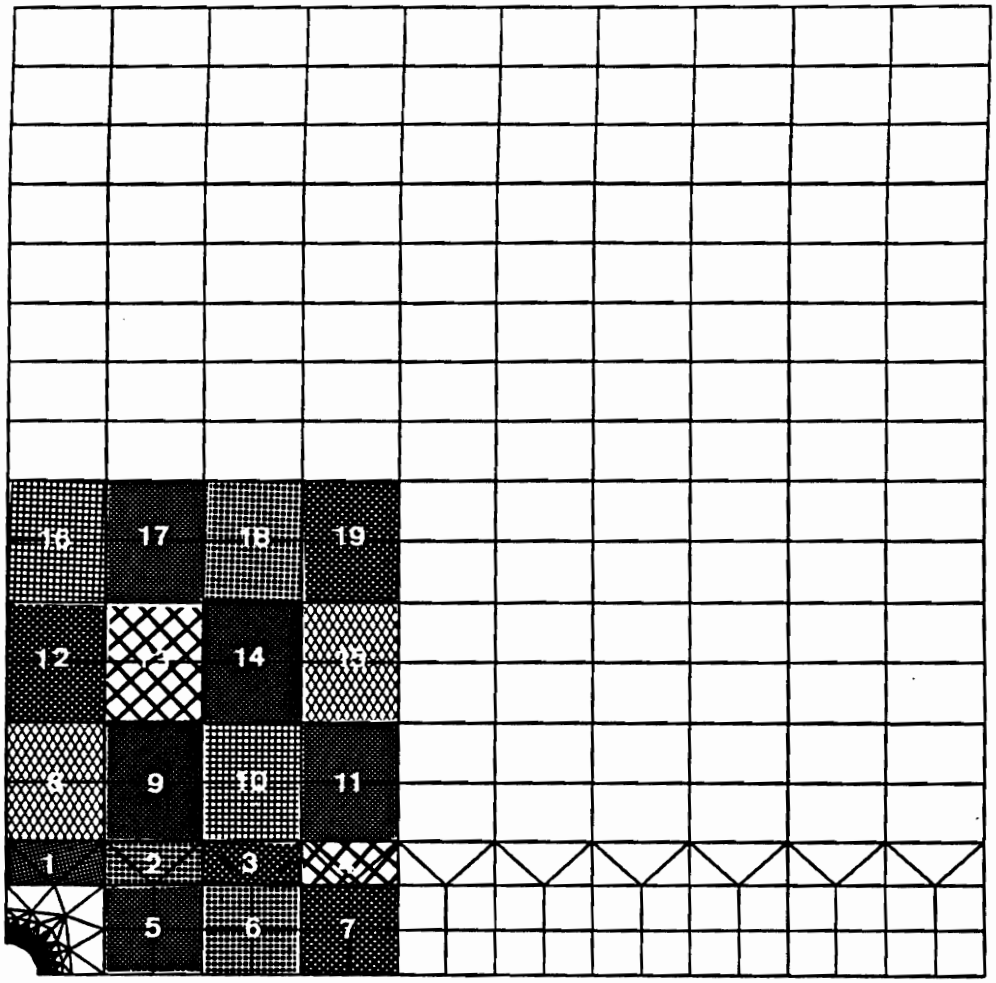

Figure 5.12: Finite element mesh showing 19 actuator locations away from the transition region

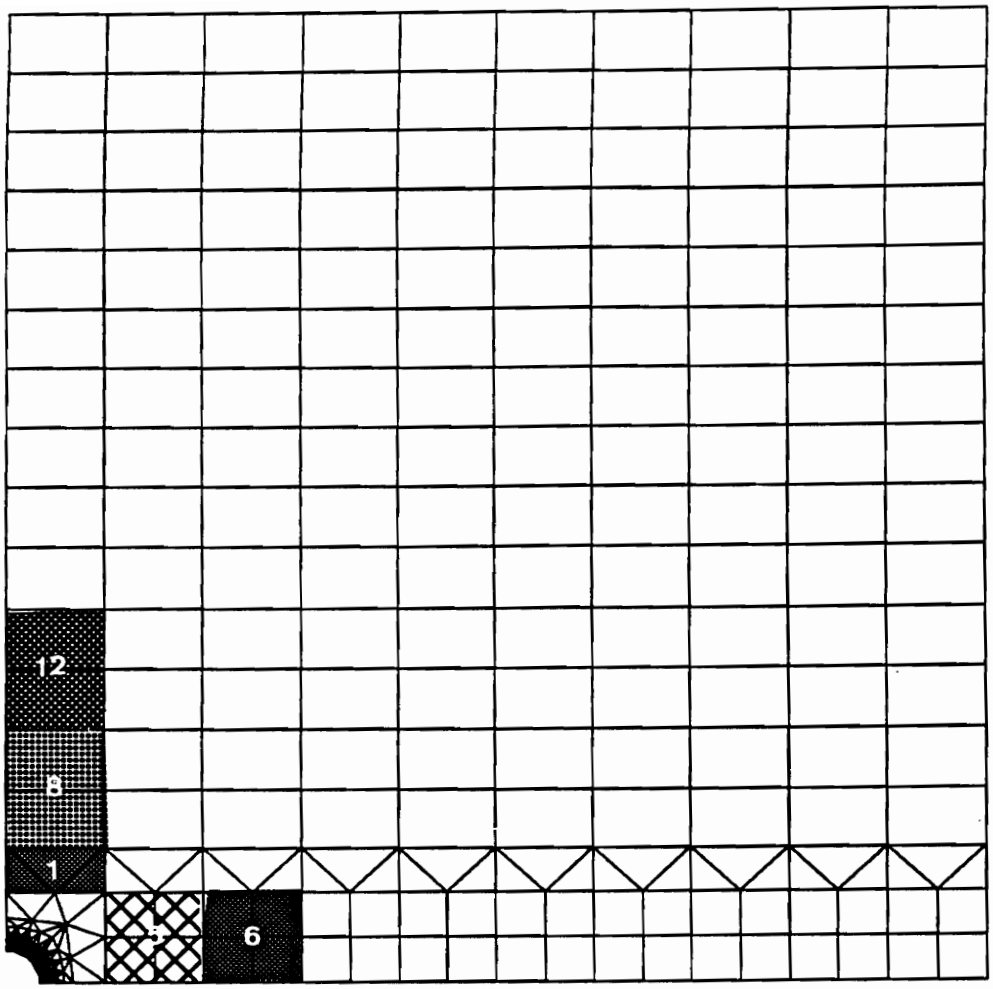

Figure 5.13 : Actuator locations obtained with genetic algorithm for 2ta/tp = 0.2 and available area limited to 11 sq. in.

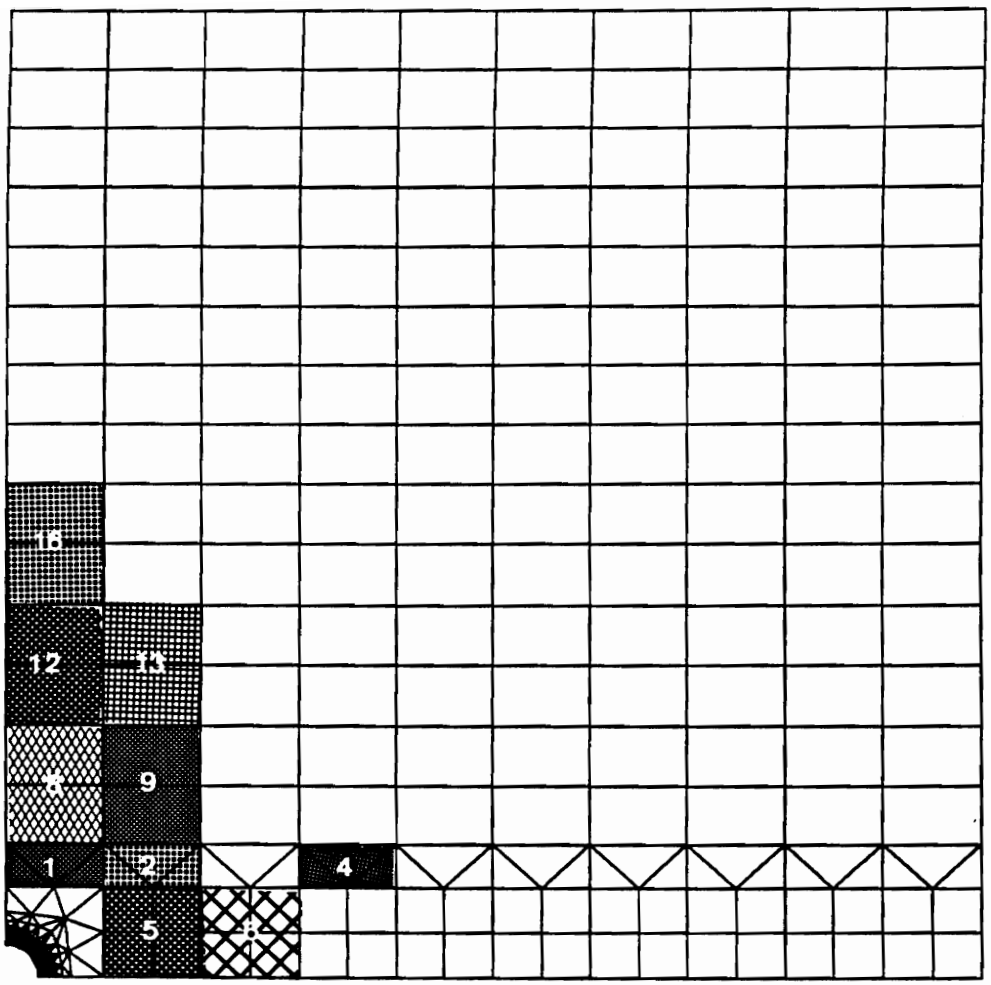

Figure 5.14 : Actuator locations obtained with genetic algorithm for 2ta/tp = 0.2 and available area limited to 22 sq. in.

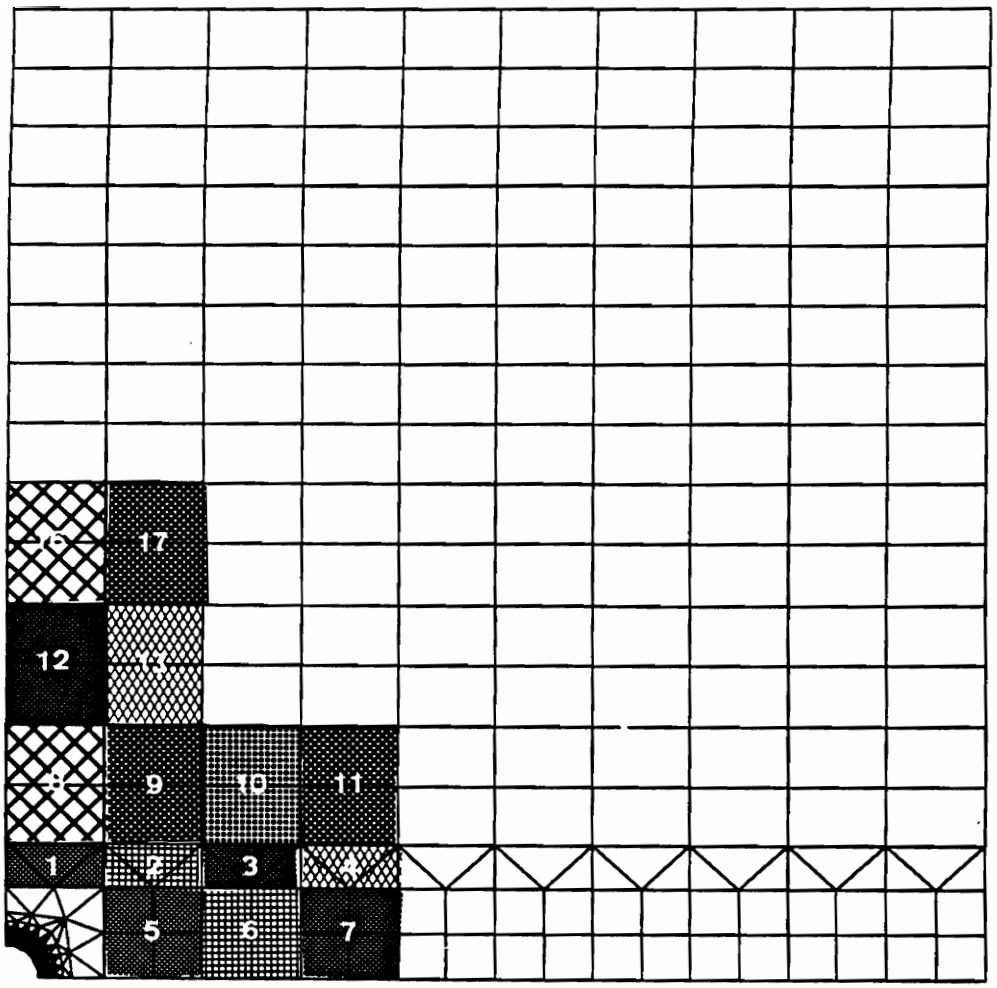

Figure 5.15 : Actuator locations obtained with genetic algorithm for 2ta/tp = 0.2 and available area limited to 33 sq. in.

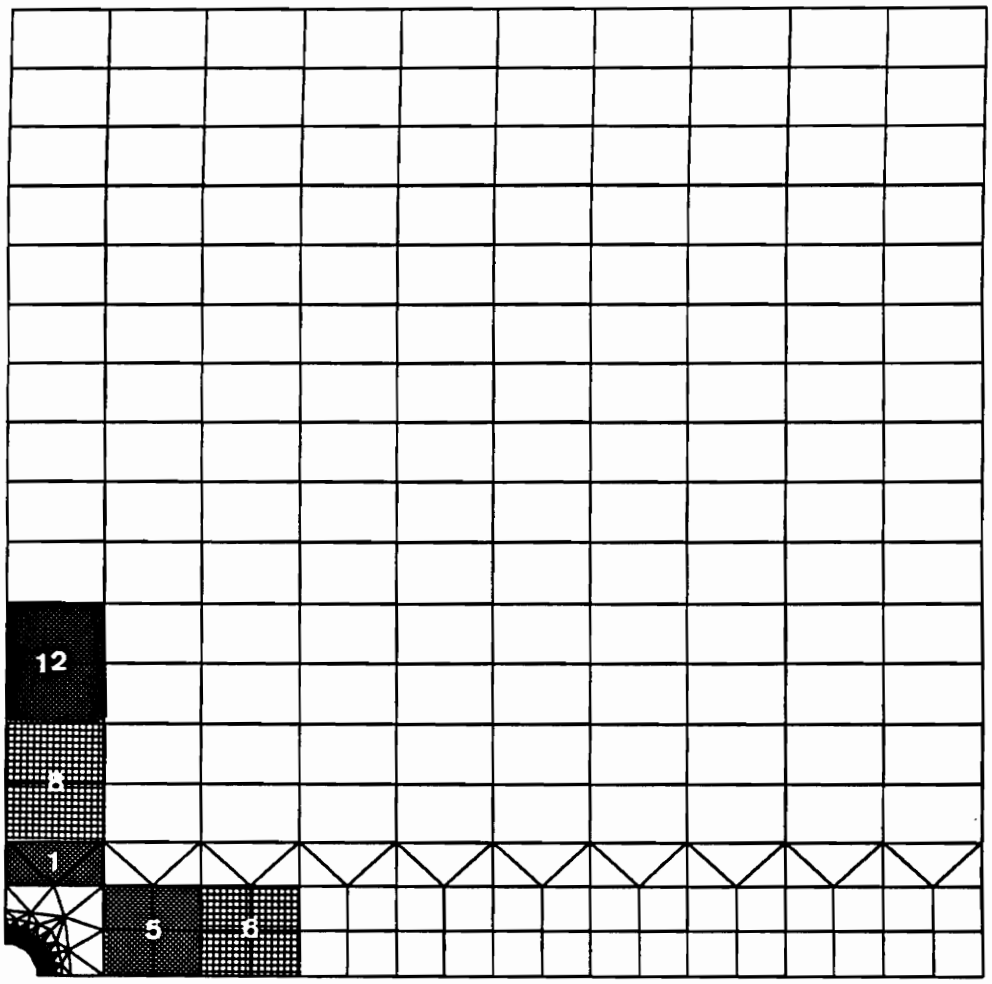

Figure 5.16 : Actuator locations obtained with genetic algorithm for 2ta/tp = 1.0 and available area limited to 11 sq. in.

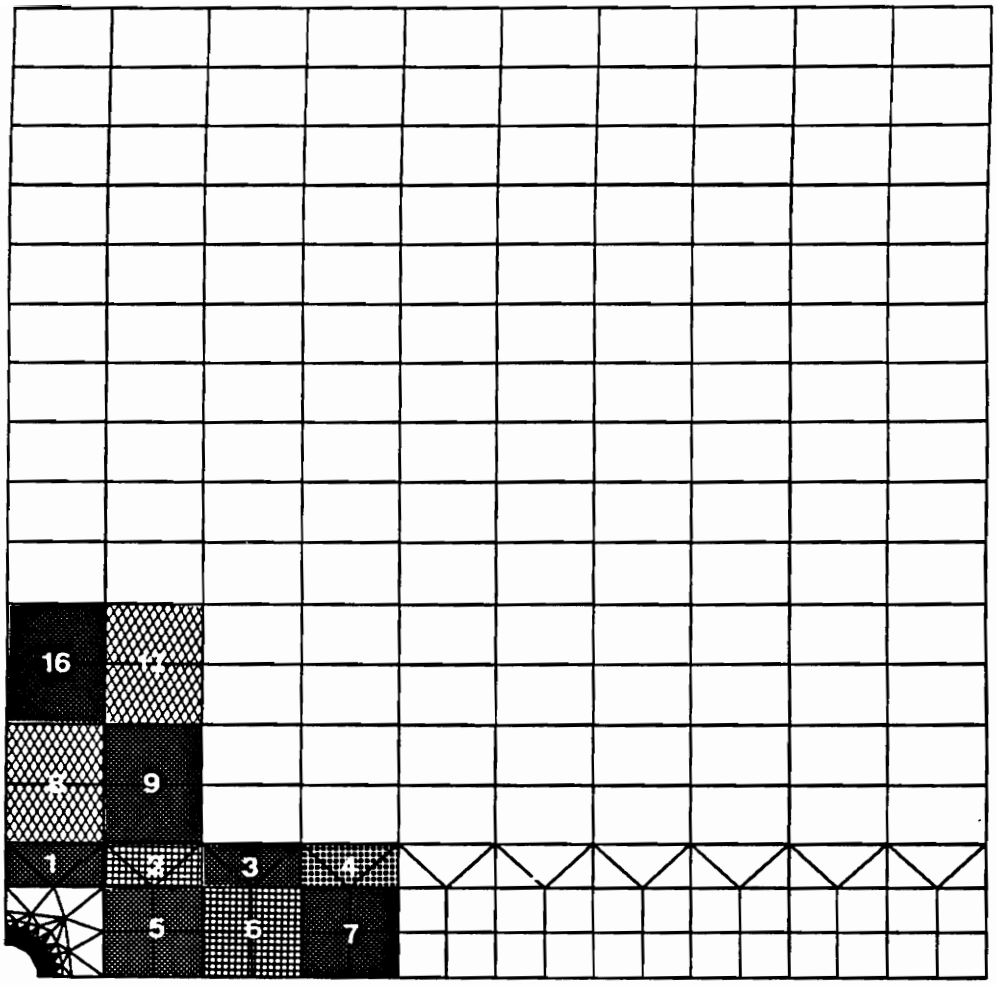

Figure 5.17 : Actuator locations obtained with genetic algorithm for 2ta/tp = 1.0 and available area limited to 22 sq. in.

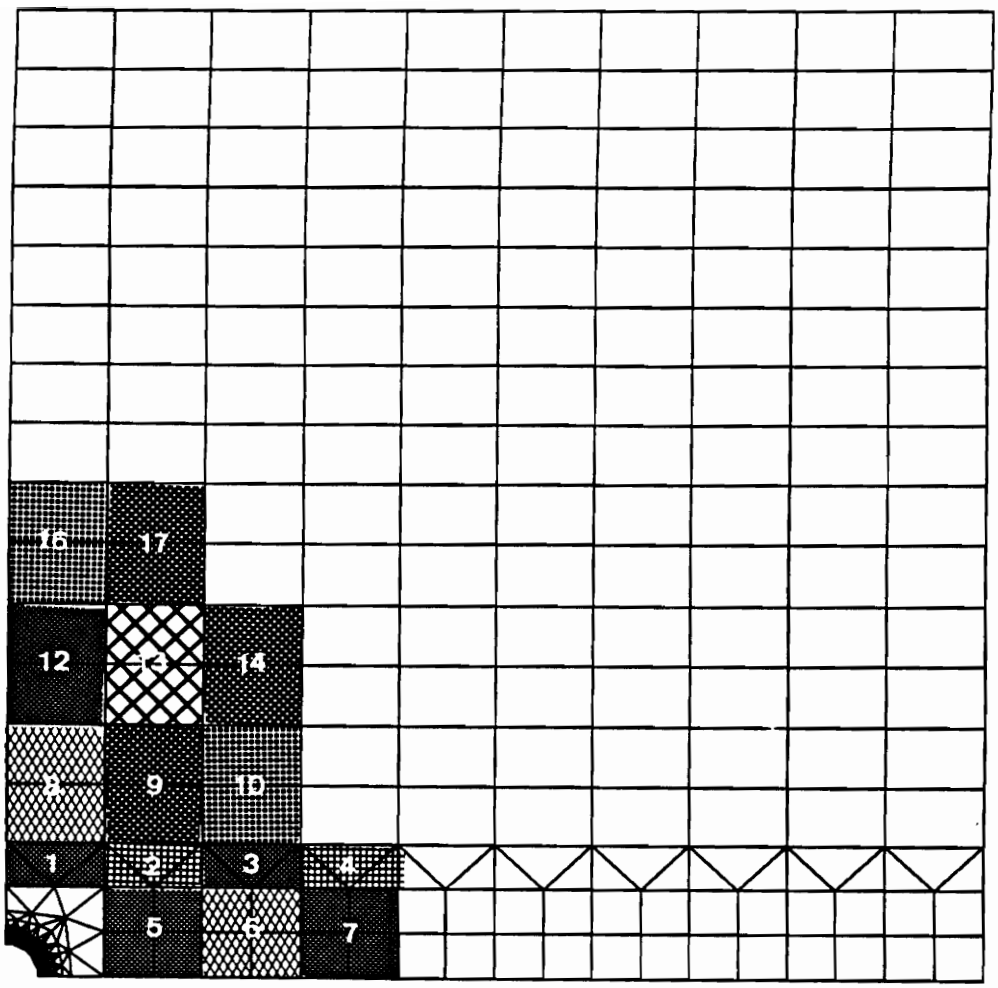

Figure 5.18 : Actuator locations obtained with genetic algorithm for 2ta/tp = 1.0 and available area limited to 33 sq. in.

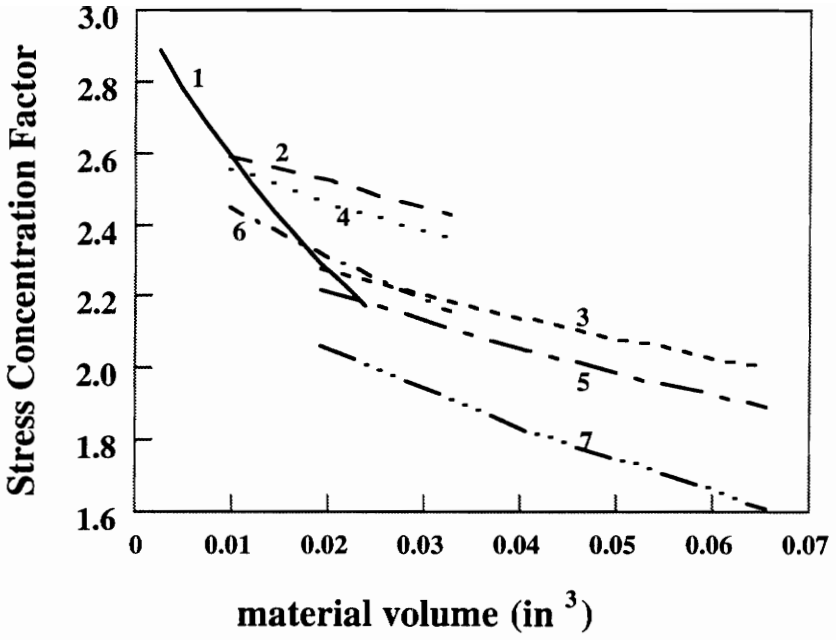

Figure 5.19 : Passive versus active reduction: comparison of extra weight for present & improved technology for 7 cases of bonded actuators :

1) passive stiffening,
2) present technology (free induced strain=1000 με , actuator tensile strength = 9ksi) -2ta/tp=0.4,
3) present technology -2ta/tp=0.8,
4) Free induced strain=1000με; actuator tensile strength=15ksi, 2ta/tp=0.4,
5) Free induced strain=1000με; actuator tensile strength=15ksi, 2ta/tp=0.8.
6) Free induced strain=2000με; actuator tensile strength=20ksi, 2ta/tp=0.4,
7) Free induced strain=2000με; actuator tensile strength=20ksi, 2ta/tp=0.8.

CHAPTER 6

CONCLUDING REMARKS

The objective of our work was to investigate the potential of reducing stresses in regions of stress concentration by applied induced strains. A thin 30 inch square plate with a 1 inch dia. circular hole under uniaxial load was used throughout this study.

We started by considering an ideal case with few physical limitations for the purpose of probing the limits of active stress reduction. We used the entire thickness of the plate for actuation, and assumed that the mechanical properties of the actuators are the same as those of the plate. We also did not place any limits on the magnitude of applied actuation strains, or considered other physical limitations of the actuators.

For the isotropic case, both analytical optimization methods and numerical optimization based on finite element simulations were used to obtain optimal axisymmetric and non-axisymmetric actuation strain distributions. We found that isotropic axisymmetric actuation strains, i.e., $\epsilon_r^i = \epsilon_\theta^i = \epsilon^i$, applied in a circular ring, do not affect stresses in the interior area. With axisymmetric actuation strain distributions, the stress concentration factor was reduced from 3 to 2. Actuation strains were only required in a ring around the hole with $r \leq 1.21A$ and $r \leq 1.25A$ for Von-Mises stress and maximum shear stress criteria, respectively.

Non-axisymmetric actuation strains were applied to an area with outer diameter 1.5 times the diameter of the hole. With analytical optimization, the stress concentration factor for maximum shear stress and Von-Mises criteria were reduced to 1.45 and 1.58, respectively. With finite element based optimization, the corresponding values were 1.62 and 1.65, respectively.

Numerical optimizations based on finite element simulations were also carried out for a composite plate with a hole, applying actuation strains over an area with outer diameter 1.5 times the diameter of the hole. With axisymmetric actuation strain distributions, the stress concentration factor was reduced from 4.47 to 2.45 for the $(0_2^\circ/\pm 45^\circ/0_2^\circ)_s$ laminate and 3.20 to 1.97 for the $(\pm 45^\circ/0_2^\circ/\pm 45^\circ/0_2^\circ)_s$ laminate. Non-axisymmetric actuation strain distributions reduced the SCF from 4.47 to 1.64 for the $(0_2^\circ/\pm 45^\circ/0_2^\circ)_s$ laminate and 3.20 to 1.46 for the $(\pm 45^\circ/0_2^\circ/\pm 45^\circ/0_2^\circ)_s$ laminate.

Next, we considered a more realistic isotropic case, consisting of bonded and embedded piezoelectric actuators. We found that having partial-thickness actuators changes the stress distribution adversely. In particular the radial stresses produced by the actuators were quite large. This effect was found to completely erase any benefits associated with axisymmetric actuation.

With non-axisymmetric partial-thickness actuation, the effectiveness of the actuation depends on the magnitude of the loads. Two types of loads were selected for the evaluation, a fatigue load case corresponding to 40 % of the yield stress and an extreme load case corresponding to the yield stress. For the fatigue load case, the reductions obtained in SCF with thin actuators were small due to limit of 1000 $\mu\epsilon$ on applied induced strains. However, by increasing the thicknesses of the actuators large reductions in SCF were still possible. For $2t_a/t_p = 0.8$, where t_p is the thickness of the plate and t_a is the thickness of the actuators on each side of the plate, the SCF could be reduced to 1.84 and 2.15 with bonded and embedded actuators, respectively. Actuator failure was considered next, with stresses in the actuators limited by a simplified Mohr's criterion. This additional constraint was found to increase SCF by 2 - 3 %. The shear lag effect was found to be large for small and thick actuators. To increase the effectiveness

of the actuators and also to alleviate the problem of actuator failure, actuators were prestressed before attaching to the plate. It was found that prestressing could reduce the SCF by an additional 7 - 9 %.

Hence, it can be seen that the piezoelectric actuators are effective for the fatigue load case, even with present technology limitations. However, due to the repetitive nature of the load, actuators will be called upon frequently and the energy expenditure could be substantial. Also we may have fatigue problem with the actuators themselves.

For the extreme load case, reduction obtained in SCF with piezoelectric actuators were small. The actuators were needed to be placed over larger area to achieve large reduction in SCF. Also, passive stiffening was found to be more effective in reducing SCF than bonded actuators with present technology limitations.

REFERENCES

[1] Davidson,R., "The Current Status and Future prospects of Smart Composites," Space Applications of Advanced Structural Materials, Proceedings of an International Symposium by the European Space Agency, The Netherlands, 21-23 March, 1990, pp. 429-436.

[2] Zuk, W. and Clark, R. H., "Kinetic Architecture," 1st edition, Van Nostrand Reeinhold, New York, pp. 14.

[3] Wada, B. K., Fansion, J. L., and Crawley, E. F., "Adaptive Structures," 1989 ASME Winter Annual Meeting, San Francisco, CA, Dec. 10-15, 1989, pp. 1-8.

[4] Rogers, C., "Intelligent Material Systems - The Dawn of a New Materials Age," Class notes.

[5] Gandhi, M. V., Thompson, B. S., Kasiviswanathan, S. R., Choi, S. B., Hansknecht, B., Soomar, M., Huang, X., Chmielewski, C., and Foiles, C., "Smart Materials and Structures Incorporating Hybrid Actuator and Sensing Systems," Smart Structures and Materials, ASME 1991, AD-Vol. 24/AMD-Vol. 123, pp. 151-156.

[6] Miura, K., "Studies of Intelligent Adaptive Structures," 1989 ASME Winter Annual Meeting, San Francisco, CA, Dec. 10-15, 1989, pp. 89-94.

[7] Spillman, W. B., "The Evolution of Smart Structures/Materials," First European Conference on Smart Structures and Materials, Glasgow, 12 -14 May, 1992, SPIE Vol. 1777, pp. 97-114.

[8] Chaudhry, Z. A. , "Enhanced Induced Strain Actuator Performance Through Discrete Attachement to Structural Elements," Ph. D. Dissertation, Virginia Polytechnic Institute and State University, Blacksburg, Virginia, July, 1992.

[9] Rogers, C. A., "Recent Findings in Active Structural Control," ASCE NinthEngineering Mechanics Conference, Texas A & M University, College Station, Texas, 25-27 May, 1992.

[10] "The Concept of Intelligent Materials and the Guidelines on R & D promotion," Japan Science and Technology Agency, 30 th November, 1989.

[11] Dittrich, K. W., "Multifunctional structures for Aerospace applications," Space Applications of Advanced Structural Materials, Proceedings of an International Symposium by the European Space Agency, The Netherlands, 21-23 March, 1990, pp. 437-441.

[12] Measures, R. M., "Smart Structures with Nerves of Glass," Progress in Aerospace Science, Vol. 26, 1989, pp. 289-351.

[13] Udd, E., "Fiber Optic Smart Structures for Aerospace Applications," First European Conference on Smart Structures and Materials, Glasgow, 12 -14 May, 1992, SPIE Vol. 1777, pp. 7-12.

[14] Culshaw, B. and Michie, C., "Fiber Optic Strain and temperature Measurment in composite Materials - A Review of the OSTIC Program," Proceedings, Conference on Recent Advances in Adaptive and Sensory Materials and their Applications, Blacksburg, Virginia, 27-29 April, 1992, pp. 791-808.

[15] Rogers, C. A., "Intelligent Material Systems and Structures," Proceedings, U. S. - Japan Workshop on Smart/Intelligent Materials and Systems, Honolulu, Hawaii, 19-23 March, 1990.

[16] Neurgaonkar, R. R., Oliver, J. R., and Nelson, J. G., "Ferroelectric Properties of highly Densified PZT and PLZT Piezoelectric Ceramics," Proceedings, Conference on Recent Advances in Adaptive and Sensory Materials and their Applications, Blacksburg, Virginia, 27-29 April, 1992, pp. 175-182.

[17] Natori, M., Shibayama, Y., and Sekine, K., "Active Accuracy Adjustment of Reflectors Through the Change of Element Boundary," Proceeding, AIAA /ASME/ASCE/AHS/ ASC 30th Structures, Structural Dynamics and Matterials Conference, Mobile, AL, 1989.

[18] Jia, J. and Rogers, C. A., " Formulation of a Laminated Shell Theory Incorporating Embedded Distributed Actuators," ASME Transactions, Vol. 112, Dec. 1990, pp.596-604.

[19] Liang, C. and Rogers, C. A., "One-Dimensional Thermomechanical Constitutive Relations of Shape Memory Materials," Journal of Intelligent Material systems and Structures, Vol. 1, No. 2, 1990, pp. 164-170.

[20] Rogers, C. A. and Robertshaw, H. H., "Shape Memory Alloy Reinforced Composites," Engineering Science Reprints 25, ESP25.88027, Society of Engineering Sciences, 1988.

[21] Lin, M.W., and Rogers, C.A., "Analysis of Stress Distribution in a Shape Memory Alloy Composite Beam," AIAA-91-1164-CP, Proceeding, AIAA/ASME/ASCE/AHS/ ASC 32nd Structures, Structural Dynamics and Matterials Conference, Baltimore, MD, 1991, part 1, pp. 169-177.

[22] Liang, C., and Rogers, C.A., "Behaviour of Shape Memory Alloy Actuators Embedded in Composites," Proceeding, AIAA/ASME/ASCE /AHS/ ASC 32nd Structures, Structural Dynamics and Matterials Conference, 1991.

[23] Chaudhary, Z., and Rogers, C.A., "Bending and Shape Control of Beams Using SMA Actuators," Journal of Intelligent Material Systems and Structures, Vol. 2, Oct. 1991, pp. 581-602.

[24] Jia, J., and Rogers, C.A., "Formulation of a Laminated Shell Theory Incorporating Embedded Distributed Actuators," ASME Transactions, Vol. 112, Dec. 1990, pp. 596-604.

[25] Fansion, J. L., and Chen, J. C., "Structural Control by the Use of Piezoelectric Active Members," Proceedings of NASA/DOD Control-Structure Interaction Conference, NASA cp-2447, Part II, 1986.

[26] Baz, A., and Poh, S., "Optimum Vibration Control of Flexible Beams by Piezoelectric Actuators," NASA CR-180209, 1987.

[27] Crawley, E.F. and de Luis, J., "Use of Piezoelectric Actuators as Element of Intelligent Structures," AIAA Journal, 1987, vol. 25, no. 10, pp. 1373-1385.

[28] Crawley, E.F., de Luis, J., Hagood, N. W., and Anderson, E. H., "Development of Piezoelectric Technology for Applications in Control of Intelligent Structures," presented at American Control Conference, Atlanta, June, 1988.

[29] Coulter, J. P., Weiss, K. D., Carlson, J. D., "Electrorheological Materials and Their Usage in Intelligent Material Systems and Structures," Class notes.

[30] Korobko, E. V., "The Main Properties of ERF's and Their Applications," Proceedings, Conference on Recent Advances in Adaptive and Sensory Materials and their Applications, Blacksburg, Virginia, 27-29 April, 1992, pp. 3-56.

[31] Uchino, K., "Electrostrictive Actuators: Materials and Applications," American Ceramic Society Bulletin, 65(4), 1986, pp. 647-652.

[32] Crowson, A., "Smart Materials and Structures: An Army Perspective," Proceedings, Conference on Recent Advances in Adaptive and Sensory Materials and their Applications, Blacksburg, Virginia, 27-29 April, 1992, pp. 811-821.

[33] Hanagud, S., Won, C. C., and Obal, M. W., "Optimal Placement of Piezoceramic Sensors and Actuators," pp.1884-1889.

[34] Dimitriadis, E. K., Fuller, C. R., and Rogers, C. A., "Piezoelectric Actuators for Distributed Noise and Vibration Excitation of Thin Plates," ASME Failure Prevention and Reliability, 1989, DE-Vol. 16, pp. 223-233.

[35] Bailey, T., and Hubbard, J. E., "Distributed Piezoelectric-Polymer Active Vibration Control of a Cantilever Beam," AIAA Journal of Guidance and Control, Vol. 8, No. 5, 1985, pp. 605-611.

[36] Nitzsche, F. and Breitbach, E., "The Smart Structures Technology in the Vibration Control of Helicopter Blades in Forward Flight," First European Conference on Smart Structures and Materials, Glasgow, 12 -14 May, 1992, SPIE Vol. 1777, pp. 321-324.

[37] Clark, R. L. and Fuller, C. R., "Control of Sound Radiation with Adaptive Structures," Journal of Intelligent Material Systems and Structures, Vol. 2, July 1992, pp. 431-.

[38] Rogers, C. A., "Active Vibration and structural Acoustic Control of Shape Memory Alloy Hybrid Composites: Experimental Results," International Congress on Recent Developments in air and Structure Borne Sound and Vibration, Auburn University, 6-8 March, 1990, pp. 695-708.

[39] Anders, W. S., Rogers, C. A., and Fuller, C. R., "Vibration and Low Frequency Acoustic Analysis of Piecewise-Activated Adaptive Composites Panels," Journal of Composite Materials, Vol. 26, No. 1, 1991, pp. 103-120.

[40] Fansion, J. L. and Garba, J. A., "Experimental Studies of Active members in Control of Large Space Structures," Proceeding, AIAA/ASME/ASCE/AHS/ASC 29th Structures, Structural Dynamics and Materials Conference, Williamsburg, VA, 18-20 April, 1988, part 1, pp. 9-17.

[41] Natori, M, Iwasaki, K., Kuwao, F., "Adaptive Planar Truss Structures and their Vibration Characteristics," Proceeding, AIAA/ASME/ASCE/AHS/ASC 28th Structures, Structural Dynamics and Materials Conference, Monterey, CA, 9-10 April, 1987, part 2A, pp. 143-151.

[42] Takahara, K., Kuwao, F., Shigehara, M., Katoh, T., Motohashi, S., Natori, M., "Piezo Linear Actuators for Adaptive Truss Structures," 1989 ASME Winter Annual Meeting, San Francisco, CA, Dec. 10-15, 1989, pp. 83-88.

[43] Miura, K., "Adaptive Structures Research at ISAS, 1984-1990," Journal of Intelligent Material Systems and Structures, Vol. 3, Jan. 1992, pp. 54-74.

[44] Crawley, E. F. and Lazarus, K. B., "Induced Strain Actuation of Isotropic and Anisotropic Plates," AIAA Journal, Vol. 29 No. 6, pp. 944-951.

[45] Austin, F. Knowles, G. J., Jung, W. G., Tung, C. C., and Sheedy, E. M., "Adaptive/ Conformal Wing Design for Future Aircraft," First European Conference on Smart Structures and Materials, Glasgow, 12 -14 May, 1992, SPIE Vol. 1777, pp. 387-390.

[46] Spangler, R. L. and Hall, S. R., "Piezoelectric Actuators for Helicopter Rotor Control," Proceeding, AIAA/ASME/ASCE/AHS/ASC 31st Structures, Structural Dynamics and Materials Conference, Long Beach, CA, 2-4 April, 1990.

[47] Lazarus, K. B., Crawley, E. F., and Bohlman, J. D., "Static Aeroelastic Control using Strain Actuated Adaptive Structures," ist U. S. / Japan Conference on Adaptive Structures, 13-15 Nov., 1990, Maui, Hawaii.

[48] Song, O., Librescue, L. and Rogers, C. A., "Static Aeroelastic Behavior of Adaptive Aircraft Wing Structures Modeled as Composite Thin-walled Beams," Proceedings, International Forum on aeroelasticity and Structural Dynamics, Aachen, Germany, 3-6 June, 1991, pp. 46-55.

[49] Chaudhry, Z. and Rogers, C. A., "Enhanced Structural Control with Discretely Attached Induced Strain Actuators," Proceeding, AIAA/ASME/ASCE/AHS/ASC 33rd Structures, Structural Dynamics and Materials Conference, Dallas, Texas,1992.

[50] Gerardi, T. G., "Health Monitoring Aircraft," Journal of Intelligent Material Systems and Structures, Vol. 1, July 1990, pp. 375-385.

[51] Hickman, G. A., Gerardi, J. J., and Feng, Y., "Application of Smart Structures to Aircraft Health Monitoring," Journal of Intelligent Material Systems and Structures, Vol. 2, July 1991, pp. 411-430.

[52] Matsuzaki, Y., Hosoda, H., and Abe, S., "Application of Fuzzy Control/Neural Networks to Rendezvous Simulation of Space Structure," First European Conference on Smart Structures and Materials, Glasgow, 12 -14 May, 1992, SPIE Vol. 1777, pp. 293-296.

[53] Shaikh, N., Chen, S., Lu, Y., and Timm, D., "Smart Structural Composites with the Ability to Monitor Vibration and Damage," First European Conference on Smart Structures and Materials, Glasgow, 12 -14 May, 1992, SPIE Vol. 1777, pp. 123-126.

[54] Rogers, C.A., Liang, C., and Li, S., "Active Damage Control of Hybrid Material Systems using Induced Strain Actuators," AIAA-91-1145-CP, Proceeding, AIAA/ASME/ ASCE/AHS/ASC 32nd Structures, Structural Dynamics and Materials Conference, Baltimore, MD, 1991, part 2, pp. 1190-1203.

[55] Holnicki-Szulc, J., Virtual Distortion Method, Lecture Notes in Engineering, 65, Springer-Verlag Berlin, 1991, pp. 84-89.

[56] Timoshenko, S. P. abd Goodier, J. N. , Theory of Elasticity, McGraw Hill, Third Edition, 1970.

[57] Murtagh, B.A., and Saunders, M.A., "MINOS 5.0 User's Guide," Technical Report Sol 83-20, Stanford University, 1983.

[58] Forray, "MINOS 5.0 User's Guide," Technical Report Sol 83-20, Stanford University, 1983.

[59] Tsai, W.S., Composites Design, Think Composites, Dayton, Ohio, 1986 .

[60] Hong, C.S., and Crews, J.H., "Stress-concentration Factors for Finite Orthrotropic Laminate with a Circular Hole and Uniaxial Loading," NASA-TP-1469, May 1979.

[61] Jones, R.M., "Mechanics of Composite Materials," McGraw-Hill Kogakusha, Ltd., 1975, pp. 74-76.

[62] Beer, F. P. and Johnston, E. R. Jr. , " Mechanics of Materials," McGraw Hill, Second Edition, 1981.

[63] Lin, M.W., and Rogers, C.A., "Formulation of a Beam Structure with Induced Strain Actuation Based on an Approximated Linear Shear Stress Field," AIAA-92-2524-CP, Proceeding, AIAA /ASME /ASCE /AHS/ ASC 33nd Structures, Structural Dynamics and Matterials Conference, Dallas, Texas, 1992, part 2, pp. 896-904.

[64] Holland, J. H., "Adaptation In Natural and Artificial Systems," Ann Arbor, The University of Michigan Press, 1975.

Vita

The author was born in Nagpur, India, on the 18th day of March, 1960. He received his bachelor of Technology degree in Naval Architecture from the Indian Institute of Technology, Kharagpur, India, in May 1981. Following that, he worked in the Design and Development Section of Mazagon Dock Ltd., Bombay, India, for five years. In September 1986, he received a scholarship from Government of India to pursue a Master of Science degree in the Department of Aerospace and Ocean Engineering at Virginia Polytechnic Institute and State University. Mr. Sensharma received his M. S. degree in August, 1988. In fall 1989, he joined the doctoral program in the area of ocean structures. In summer of 1991, Mr Sensharma changed his research focus to Smart Structures and received his doctoral degree in December, 1993.